RAMAN scattering of single photons and its use for quantum networks and high-precision measurements

Dissertation
zur Erlangung des Grades
des Doktors der Naturwissenschaften
der Naturwissenschaftlich-Technischen Fakultät
der Universität des Saarlandes

von

Philipp Conrad MÜLLER

Saarbrücken

—2021—

Tag des Kolloquiums:	08. Oktober 2021
Dekan:	Prof. Dr. Jörn Erik Walter
Berichterstatter:	Prof. Dr. Jürgen Eschner Dr. Nicolas Sangouard
Vorsitz:	Prof. Dr. Christoph Becher
Akad. Mitarbeiter:	Dr.-Ing. Andreas Tschöpe

RAMAN-Streuung einzelner Photonen und ihr Nutzen für Quantennetzwerke und Hochpräzisionsmessungen
(German title)

Contents

Abstract

This work concerns the interaction of single atoms and light as a platform for quantum-communication networks, both experimentally and simulative.
It treats, at its kernel, the calcium ion as a node of such a network, i. e. as storage of a quantum bit. Especially the quantum interface of this ion with the light field and its experimental implementation are addressed in detail. Thereby spontaneous RAMAN scattering is used to transfer the polarisation state of a single photon onto the ion's electronic state and vice versa.
On the way to this interface the RAMAN scattering process of single photons was investigated intensively. This led to a high-precision experiment measuring the phase shift of such photons as well as a detailed theoretical study of the spectral and temporal structure of the photons.
The experiments used and expanded an existing hybrid quantum-optical set-up consisting of two identical ion traps and a light source of entangled photon pairs.

Zusammenfassung

Diese Arbeit behandelt die Wechselwirkung einzelner Atome mit Licht als Plattform für Quantenkommunikationsnetzwerke, sowohl experimentell als auch simulativ.
Im Kern befasst sie sich mit dem Calciumion als Knotenpunkt eines solchen Netzwerks, d. h. als Speicher eines Quantenbits. Insbesondere wird die Quantenschnittstelle dieses Ions mit dem Lichtfeld und ihre experimentelle Umsetzung detailliert behandelt. Dabei wird durch spontane RAMAN-Streuung der Polarisationszustand eines einzelnen Photons auf den elektronischen Zustand des Ions übertragen und umgekehrt.
Auf dem Weg zur Umsetzung dieser Schnittstelle wurde der RAMAN'sche Streuprozess einzelner Photonen genau untersucht. Dies mündete in einem Hochpräzisionsexperiment zur Messung des Phasengangs solcher Photonen sowie zu einer detaillierten theoretischen Studie der spektralen und temporalen Struktur der Photonen.
Zur Verwirklichung dieser Experimente wurde ein bestehender hybrider quantenoptischer Aufbau, bestehend aus zwei identischen Ionenfallen sowie einer Lichtquelle verschränkter Photonenpaare, genutzt und erweitert.

Zammefassung

Die dò Ahwett hannelt vun de Weggselwirgung ähnselner Atome mim Licht als Arwettsplatt fa e Quandenetzwerk – unn zwar experimendell unn simmuleert.
In de Hauptsach geht's um's Calciumion als Knibbelche vun some Netzwerk, das häßt, es dud e Quandebit speichere. Insbesonnere gebt die Quandeschnittstell vum Ion mim Lichtfeld unn die experimendell Umsetzung dòdevun genau beschrieb. Dòdebei werd mit spondaner RAMAN-Streiung de Polarisationszustand vumme ähnselne Phoddòn uff de elegdronische Zustand vum Ion iwwertrah odder annersch'erum.
Uffem Wäh zu der dò Schnittstell is 'em RAMAN sei Streiprozess genau unnersucht wòr. Das hat zum ähne zuner scheen Messung vum Phasegang vun so Phodone gefihrt unn zum annere zuner deddaijiert theoredisch Ahwett iwwer die spegdral unn zeitlich Strugdur vun denne Phodone.
Fa die dò Experimende ze mache, is amme voorischer Quandeobdik-Uffbau geknoddelt wòr unn aach noch meh draangebaut wòr. Bestehn duder aus zwä Ionefalle vun ähn unn de selb Sort unn'er Quell vun veschrängde Phodonepaare.

Introduction

«I would like, ah, if I may,
... to take you on a strange journey.»

— C. Gray, RHPS (1975)[85]

The human civilisation is at the advent of a new milestone on the way of its technological development—the quantum computer. It opens the door not only to a huge speed-up due to the quantum parallelism, but although to new algorithms that are not possible on classical machines. Its influence in the upcoming decades is presumed to be as high as the invention of the classical computer had been in the past decades. At the risk of seeming pretentious the author suggests this thesis to be seen as one of the many cobblestones that pave the road to a quantum computer based on single calcium ions.

A historical prologue

Since the emergence of quantum mechanics at the beginning of the twentieth century it evolved into one of the two most-successful theories in the natural sciences, besides the theory of general relativity. The key to its success—as of all other scientific theories—is verification/falsification of its different implications through a plenty of experiments and observations of predicted events, and finally its (technical) application. All quantum effects arisen from theory that have been tested

in experiments were confirmed very well. Such an extreme success tempted the Horodeckis to say: «What is predicted by quantum formalism must occur in the laboratory.» [46].
Even more astonishing is the range of applications of quantum physics as it grew since the middle of the past century, e. g. high-impact inventions like the transistor, the laser, and the photovoltaic cell. The tremendous change in the human society that is owed to the conventional computer would not be the same without the many quantum technologies behind it. But the new millennium goes even deeper into the application of quantum phenomena as the idea of the quantum computer is at the threshold of its materialisation.

Quantum computation

The idea of a quantum computer came up in about 1980 by, among others, Yuri Manin [73] and Richard Feynman [31]. Based on the insight that the high degree of correlation in quantum systems causes the calculating time of a conventional computer to grow exponentially with the simulated quantum system's size (i. a. NP-hard problems), the idea bloomed that a computer based itself on quantum mechanics may simulate another quantum-mechanical system in a sufficiently fast manner.
Such a device is defined in analogy to the conventional computer as a set of quantum logic gates that transform a certain input state of one or more quantum bits (q-bits) into an output state which is the desired result of the calculation. In contrast to the classical machine it exploits the quantum phenomena of superposition and entanglement. Sloppily said, the first allows for q-bits to be in both logic states, «0» and «1», simultaneously, and the other for stronger correlation between q-bits as possible in classical systems. Both together open up a plenty of new logic gates not possible in conventional computers, the said quantum (logic) gates, that allow for new kinds of algorithms, and enable a high degree of parallelism in the computation.
In the following years, the first specific algorithms for quantum computers, i. e. sets of quantum gates, were proposed. The three most-prominent exemplars are the Deutsch–Jozsa algorithm [20, 21] of 1985/1992 as a proof of principle for the performance advantage of quantum computation, the Shor algorithm [115, 116] of 1994 for prime factorisation in polynomial time that may drastically accelerate cryptanalysis, and the Grover algorithm [37, 38] of 1996 for data-base search that is quadratically faster than conventional algorithms. As the number, complexity, and field of potential applications for quantum algorithms are growing all the

time, even today, it is not clear which physical platform will prevail as an efficient, not to say commercial, quantum computer. To reach a decision, the research goes into several different directions with the q-bits encoded in nuclear spin ensembles by the nuclear magnetic resonance (NMR) technique [16], in magnetic flux quanta of superconducting circuits (Josephson junctions) [18], in the spin or spatial states of quantum dots [70], in colour centres of crystals (crystallographic defects) [51], in neutral atoms trapped in an optical lattice [13], or in trapped ions as proposed in this thesis. A good example of the latter, the first experimental realisation of a quantum algorithm using trapped ions, was the Deutsch–Jozsa algorithm in 2003 using a single trapped calcium-40 ion [39].
From 1996 to 2000, David DiVincenzo has drafted out seven general criteria that have to be fulfilled to accomplish sincere quantum communication [22, 23]. The first five specify the quantum computer itself:

1. A scalable physical system with well characterised q-bits,
2. The ability to initialise the state of the q-bits to a simple fiducial state, such as $|000\ldots\rangle$,
3. Long relevant decoherence times, much longer than the gate operation time,
4. A «universal» set of quantum gates, and
5. A q-bit-specific measurement capability.

The two additional criteria specify the communication between several quantum computers or nodes to establish a so-called quantum network:

6. The ability to inter-convert stationary and flying q-bits, and
7. The ability to faithfully transmit flying q-bits between specified locations.

Special attention has been drawn to the last criterion (no. 7) because the transmission of a flying q-bit does not only have to preserve the state of that q-bit but in addition the entanglement it has with other q-bits of the network. This challenge is connected with the no-cloning theorem [133] that rules out the possibility to amplify or copy a quantum state. Together with the demanded transfer of information over long distances it leads to the principle of the quantum repeater [14].
In analogy to the classical communication the channel between sender and receiver is divided by several repeater stations to decrease the information loss of the transmissions along this way. But these stations cannot just measure the incoming signals, amplify, and send them to the next station. The procedure is totally different: Before the transmission, states of maximal (or at least high) entanglement are distributed between each pair of two subsequent stations (sender,

repeaters, and receiver). As this is done only over short distances the losses are low. Afterwards, the entanglement is swapped at each repeater station leading to an entangled state of sender and receiver only. With an optional overhead of additional channels this remote entanglement may be purified. The signal that the sender wants to transmit is then teleported to the receiver using the resulting entangled state. With this technique it is possible to reduce the error probability, given e. g. by transmission through optical fibres, from exponential to polynomial growth with the length of the channel. [25]

Overview of the thesis

This thesis studies the interaction of light and matter at the fundamental level of single particles, more specifically, photons and a trapped calcium ion. In the context of quantum technology, this contributes to the development of a quantum network based on ion traps wherein the ions serve as the quantum nodes, local memories and processors of quantum information, while the photons serve as the flying q-bits to transport the information from node to node. The speciality of this system is the use of spontaneous RAMAN scattering of single photons as a heralding mechanism for the interaction. This permits high fidelity close to unity despite the low efficiency of the interaction because the detection of an emitted photon (the so-called herald) tells if the whole process was successful, and thus all failed cases can be ignored.

The **quantum interface** treated in chapter 5 is a versatile building block of the ion-trap quantum network. It uses a single calcium-40 ion trapped in a linear PAUL trap as a single-q-bit quantum node by enabling storage, readout, and entanglement of quantum states. Of DIVINCENZO's criteria this interface fulfils no. 2, 3, 5, and 6. Photon-pair sources as of section 1.5 in combination with quantum converters [12, 67] are able to realise criterion no. 7. The missing two, no. 1 and 4, are future tasks on the agenda of our research group.

The **phase-shift measurement** presented in chapter 6 has three aspects: 1.) It reveals the phase difference of the complex absorption profiles of two RAMAN transitions, not only their amplitudes. 2.) It demonstrates the high degree of control over the atom-to-photon quantum state transfer in the ion-trap set-up. 3.) Its data are evaluated through the application of the hitherto underestimated method of BAYESian inference.

The quantum interface is set as a cornerstone «on the way» to quantum networking, while the phase-shift measurement threw us «off the trail», but led to an extended investigation of the spontaneous RAMAN process and brought grand insight to

it.
As these experiments needed a significant amount of preparatory work this is expounded in the preceding chapters: the experimental set-up in chapter 1, the quantum optical theory in chapter 2 with a detailed investigation of the Raman scattering summarised in chapter 3, and the numerical simulation of the Bloch equations for the 18-level system in chapter 4.

List of publications

The following is a chronological list of the publications made during the time of this thesis, and to which the author contributed:

[107] N. Sangouard, J-D. Bancal, P. Müller, J. Ghosh & J. Eschner «Heralded mapping of photonic entanglement into single atoms in free space: proposal for a loophole-free Bell test» in *New J. Phys.* **15** (2013), 085004. DOI: 10.1088/1367-2630/15/8/085004

[111] M. Schug, J. Huwer, C. Kurz, P. Müller & J. Eschner «Heralded Photonic Interaction between Distant Single Ions» in *Phys. Rev. Lett.* **110** (2013), 213603. DOI: 10.1103/PhysRevLett.110.213603

[61] C. Kurz, J. Huwer, M. Schug, P. Müller & J. Eschner «A high-rate source for single photons in a pure quantum state» in *New J. Phys.* **15** (2013), 055005. DOI: 10.1088/1367-2630/15/5/055005

[80] P. Müller & J. Eschner «Single calcium-40 ion as quantum memory for photon polarization: a case study» in *Appl. Phys. B* **114** (2014), 303, s. arXiv: 1309.7863

This became the basis of the schemes of the quantum interface, section 5.2 on p. 82.

[113] M. Schug, C. Kurz, P. Eich, J. Huwer, P. Müller & J. Eschner «Quantum interference in the absorption and emission of single photons by a single ion» in *Phys. Rev. A* **90** (2014), 23829

[64] C. Kurz, M. Schug, P. Eich, J. Huwer, P. Müller & J. Eschner «Experimental protocol for high-fidelity heralded photon-to-atom quantum state transfer» in *Nat. Commun.* **5** (2014), 5527. DOI: 10.1038/ncomms6527

This is the first publication of an implementation of the quantum interface presented in this thesis, precisely the receiver mode, see section 5.3 on p. 89.

[66] A. Lenhard, M. Bock, C. Becher, S. Kucera, J. Brito, P. Eich, P. Müller & J. Eschner «Telecom-heralded single-photon absorption by a single atom» in *Phys. Rev. A* **92** (2015), 63827

[63] C. Kurz, P. Eich, M. Schug, P. Müller & J. Eschner «Programmable atom-photon quantum interface» in *Phys. Rev. A* **93** (2016), 62348. DOI: 10.1103/PhysRevA.93.062348

This work shows the implementation of sender and entangler mode of the quantum interface, see section 5.3.

[15] J. Brito, S. Kucera, P. Eich, P. Müller & J. Eschner «Doubly heralded single-photon absorption by a single atom» in *Appl. Phys. B* **122** (2016), 36. DOI: 10.1007/s00340-015-6276-9

[82] P. Müller, T. Tentrup, M. Bienert, G. Morigi & J. Eschner «Spectral properties of single photons from quantum emitters» in *Phys. Rev. A* **96** (2017), 23861. DOI: 10.1103/PhysRevA.96.023861

This is a detailed theoretical study of the spectra of Raman-scattered photons. Based on Tristan Tentrup's master thesis [121], it has been comprehensively revised, extended, and finalised by the author of this thesis, see chapter 3 for a summary.

[81] P. Müller, M. Kreis, P. Eich & J. Eschner «Measurement of the scattering phase in a spontaneous Raman process»

This work is recapitulated as chapter 6.

[60] S. Kucera, J. Arenskötter, M. Kreis, P. Eich, P. Müller & J. Eschner «Photon-photon to atom-photon entanglement transfer to a $^{40}Ca^{+}$ quantum node and state readout by teleportation»

This work completes the implementation of the quantum interface, the receiver mode with single photons, see section 5.3.

Chapter 1

Natural and experimental fundamentals

This chapter summarises the natural prerequisites for the experiments as well as the crucial technical parts of the experimental set-up. It begins in the first section with the conceptual basis of quantum communication—the q-bit—that is described by several mathematical objects as well as represented by different physical objects. The calcium ion serves as one of the latter, and is introduced subsequently in detail in section 1.2. Thereafter, the method and apparatus used in the research group to master this quantum-mechanical object are described.

1.1 The spheres of Bloch and Poincaré

«... only a congeries of iridescent globes,
yet stupendous in its malign suggestiveness.»

— H. Heald & H. P. Lovecraft (1933)[43]

In analogy to the binary digit or bit as the fundamental unit of information in classical computers, the proposed quantum computer is based on the «quantum bit» as

the fundamental unit of quantum information. The abbreviation «q-bit» or «qubit», introduced in [114], reminds of the cubit, the fundamental length unit of ancient architecture [68]. Perhaps, this expression was chosen with the subconscious hope that the one will suit the action to the wonderful idea of the quantum computer as the other helped to create similarly impressive constructions as the pyramids of Gizeh.

In the theory of quantum mechanics the most simple system that can carry information is the two-level system. Its general state, the q-bit, is described by the two-dimensional density operator $\hat{\rho}$ on the two-dimensional complex HILBERT space $\mathcal{H}_2$ with the universal symmetry group $SU(2)$ [71]. Thus, only three real numbers are needed to quantify $\hat{\rho}$ and so it is rewritten as a three-dimensional real vector in [33], the so-called BLOCH vector $\boldsymbol{r} = (x, y, z)$, through

$$\hat{\rho} = \frac{\mathbb{1} + \boldsymbol{r} \cdot \hat{\boldsymbol{\sigma}}}{2} = \frac{1}{2}\begin{pmatrix} 1+z & x-\mathrm{i}y \\ x+\mathrm{i}y & 1-z \end{pmatrix} \tag{1.1}$$

wherein $\hat{\boldsymbol{\sigma}} = (\hat{\sigma}_x, \hat{\sigma}_y, \hat{\sigma}_z)$ is the vector operator of the PAULI matrices [91],

$$\hat{\sigma}_x = \begin{pmatrix} 0 & 1 \\ 1 & 0 \end{pmatrix}, \qquad \hat{\sigma}_y = \begin{pmatrix} 0 & -\mathrm{i} \\ \mathrm{i} & 0 \end{pmatrix}, \qquad \hat{\sigma}_z = \begin{pmatrix} 1 & 0 \\ 0 & -1 \end{pmatrix}. \tag{1.2}$$

The reverse transformation is done by $\boldsymbol{r} = \mathrm{tr}(\hat{\rho}\hat{\boldsymbol{\sigma}}) = \langle\hat{\boldsymbol{\sigma}}\rangle$. The properties of $\hat{\rho}$ transform into properties of $\boldsymbol{r}$ as follows:

$$\begin{aligned} \hat{\rho} \text{ self-adjoint} &\leftrightarrow \boldsymbol{r} \text{ real} \\ \hat{\rho} \text{ positive semi-definite} &\leftrightarrow |\boldsymbol{r}| \leq 1 \end{aligned}$$

and $\mathrm{tr}\,\hat{\rho} = 1$ is given by construction (1.1).

Following this equivalence, precisely the isomorphism of $SU(2)$ and $SO(3)$, the q-bit may even be seen as the fundamental entity of nature as envisaged by Carl Friedrich von WEIZSÄCKER in his «Ur-Theorie» [71, 128–130]. Therein, information is seen as the most fundamental concept of nature, and encoded in quantum-mechanical states. These in turn are unravelled into tensor products of the smallest possible alternatives, the binary alternative, i. e. the decision between just two options. He calls these «ur-alternatives», nowadays they are called q-bits. As the density operator $\hat{\rho}$ of each q-bit corresponds to a three-dimensional entity $\boldsymbol{r}$ in real space, this theory considers the three-dimensionality of space as an inherent consequence of quantum mechanics.

One famous physical example of a q-bit is the spin state of a spin-½ particle. The expectation value of its spatial spin orientation $\hat{\mathbf{S}}$ is directly given by the quantum-mechanical state through $\mathrm{tr}(\hat{\rho}\hat{\mathbf{S}}) = \hbar \boldsymbol{r}$. An expressive visualisation thereof is the so-called Bloch sphere where the pairs of eigenstates of the three Pauli matrices,

$$|{\pm}1_x\rangle = \frac{1}{\sqrt{2}}\begin{pmatrix}1\\ \pm 1\end{pmatrix}, \quad |{\pm}1_y\rangle = \frac{1}{\sqrt{2}}\begin{pmatrix}1\\ \pm \mathrm{i}\end{pmatrix}, \quad |{+}1_z\rangle = \begin{pmatrix}1\\ 0\end{pmatrix}, \quad |{-}1_z\rangle = \begin{pmatrix}0\\ 1\end{pmatrix},$$

correspond to $\pm\mathbf{e}_x$, $\pm\mathbf{e}_y$, and $\pm\mathbf{e}_z$ in real space, and thus define the three Cartesian axes, see figure 1.1.

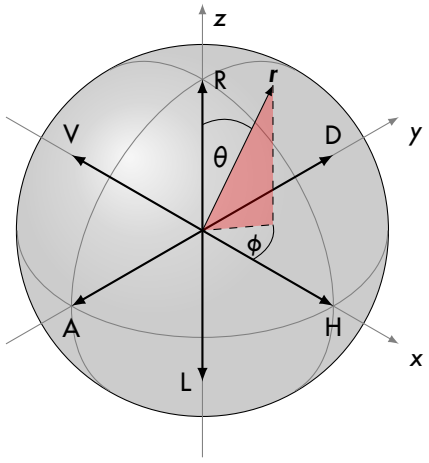

(a)

$\boldsymbol{r}$	θ	ϕ	S_1	S_2	S_3	pol.
$+\mathbf{e}_x$	$\frac{\pi}{2}$	0	1	0	0	H
$-\mathbf{e}_x$	$\frac{\pi}{2}$	π	−1	0	0	V
$+\mathbf{e}_y$	$\frac{\pi}{2}$	$\frac{\pi}{2}$	0	1	0	D
$-\mathbf{e}_y$	$\frac{\pi}{2}$	$\frac{3}{2}\pi$	0	−1	0	A
$+\mathbf{e}_z$	0	(0)	0	0	1	R
$-\mathbf{e}_z$	π	(0)	0	0	−1	L

(b)

Figure 1.1 – The Bloch and Poincaré sphere with the six basic Pauli eigenstates, their Bloch vectors $\boldsymbol{r}$ expressed by the two spherical angles θ and ϕ, and their relation to the Stokes parameters S_i, and to the six polarisation states (R, L, H, V, D, and A). Values in parentheses are chosen arbitrarily.

Another example is the polarisation state of an electromagnetic wave. This classical degree of freedom translates into a quantum-mechanical property through field quantisation: The gauge boson of the electromagnetic field is the photon (with spin 1), whose spin state is again a two-level system as the relativistic behaviour of light prohibits the one spin state perpendicular to the direction of propagation ($m_S = 0$). The two remaining states of spin orientation, parallel and anti-parallel to the propagation direction ($m_S = +1$ and -1), correspond to right- and left-circular polarisation, respectively. As a visualisation, the expectation values

of the spin orientation for all possible superposition states form again a sphere in the three-dimensional space, called POINCARÉ sphere. Two opposite points on it correspond to a pair of orthogonal polarisations. Thus, the poles correspond to the two circular polarisations, and its equator comprises all linear polarisation states.
If the direction of propagation is chosen to be the z-direction, the POINCARÉ and the BLOCH sphere are identical. Its surface ($r = 1$) encompasses all pure states while its volume covers all mixed states.
The connection to the electric field is depicted in the following. The normalised STOKES parameters [120], S_1, S_2, and S_3, are combined to a three-dimensional vector of a length $r \leq 1$ that is equal to the BLOCH vector:

$$\boldsymbol{r} = \begin{pmatrix} S_1 \\ S_2 \\ S_3 \end{pmatrix} = \begin{pmatrix} r\cos\phi\sin\theta \\ r\sin\phi\sin\theta \\ r\cos\theta \end{pmatrix} \in \mathbb{R}^3.$$

The two angles θ and ϕ for inclination and azimuth of the standard spherical coordinate system [98] are introduced to characterise all pure polarisation states (with $r = 1$). The corresponding state in the two-dimensional HILBERT space is

$$|\theta, \phi\rangle = e^{-i\frac{\phi}{2}} \cos\frac{\theta}{2}|R\rangle + e^{+i\frac{\phi}{2}} \sin\frac{\theta}{2}|L\rangle \in \mathcal{H}_2 \tag{1.3}$$

using the two states $|R\rangle$ and $|L\rangle$ of right- and left-circular polarisation as basis. It is associated with the direction of the wave's electric field vector in the same manner,

$$\boldsymbol{E}(\theta, \phi) = |\boldsymbol{E}| \left(e^{-i\frac{\phi}{2}} \cos\frac{\theta}{2}\mathbf{e}_R + e^{+i\frac{\phi}{2}} \sin\frac{\theta}{2}\mathbf{e}_L \right), \tag{1.4}$$

where $\mathbf{e}_R$ and $\mathbf{e}_L$ are the vectors for the two circular polarisations in position space. These are complex linear combinations of ones for horizontal and vertical polarisation:

$$\mathbf{e}_R = \frac{1}{\sqrt{2}}(\mathbf{e}_H + i\mathbf{e}_V) = \frac{1}{\sqrt{2}} \begin{pmatrix} 1 \\ i \\ 0 \end{pmatrix} \qquad \text{and} \qquad \mathbf{e}_L = \frac{1}{\sqrt{2}}(\mathbf{e}_H - i\mathbf{e}_V) = \frac{1}{\sqrt{2}} \begin{pmatrix} 1 \\ -i \\ 0 \end{pmatrix}.$$

This notation of the electric polarisation of a single photon as a quantum-mechanical state is henceforth used in this thesis. The integration over all possible polarisa-

tion states is the well-known spherical integral over the unit sphere:

$$\int_{\text{unit sphere}} \mathrm{d}V = \int_0^1 \int_0^\pi \int_0^{2\pi} r^2 \sin\theta \, \mathrm{d}r \, \mathrm{d}\theta \, \mathrm{d}\phi$$

1.2 The calcium ion

The quantum system of choice for the experiments presented in this work is the singly ionised isotope 40 of calcium, $^{40}Ca^+$. It has several advantages, in technical as well as in physical aspects: Calcium is a wide spread, easily extracted and purified material. In natural sources it is dominated by the stable isotope 40 with nearly 97 % [76]. Its electronic transitions are well accessible by wavelengths of conventional laser systems and it is easily trappable and storable for several hours or even days in a linear PAUL trap [47]. The 4 s–3 d quadrupole serves as a good transition for the purpose of quantum logic. The lack of nuclear spin allows one to concentrate the study on the valence electron alone, and spares the need of microwave sources to drive hyperfine transitions.

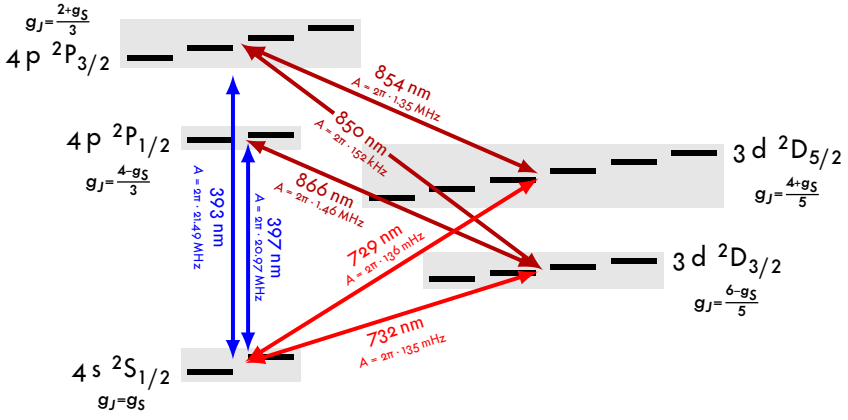

Figure 1.2 – The energy level scheme of $^{40}Ca^+$. Shown are the five lowest energy levels as grey boxes enclosing their ZEEMAN-split sub-levels as black crossbars. The seven optical transitions connecting these levels are drawn as arrows labelled with their wavelengths and EINSTEIN *A*-coefficients. The LANDÉ factors g_J of the levels are although given.

In this work, the relevant energy levels of $^{40}Ca^+$ are the ground state, where the one remaining valence electron is in the 4 s-orbital, and the lowest excited states, where it is in the 3 d- or 4 p-orbital. Due to the fine-structure splitting, these are realised as five different energy levels, shown in figure 1.2. They are connected

by seven optical transitions identified by their wavelengths. The exact values are given in table 1.1. Both transitions between 4 s and 3 d are dipole-forbidden, electric quadrupole transitions. This causes the 3 d-levels to be metastable with lifetimes of about 1 s. The lifetime τ of an energy level is given by the reciprocal of its decay constant Γ, i. e. the sum over the EINSTEIN A-coefficients of all its decay channels, $\frac{1}{\tau} = \Gamma = \sum_i A_i$ (also given in table 1.1 in technical frequencies).
The lack of a nuclear spin leaves the spin of the valence electron as the total spin of the system, $S = \frac{1}{2}$. Thus, the anomalous ZEEMAN effect is observed in presence of an external magnetic field, splitting the five energy levels further into eighteen ZEEMAN sub-levels (black crossbars in figure 1.2). For a field strength of several Gauss ($= 10^{-4}$ T), the splitting of neighbouring levels is in the order of MHz in frequency. The resulting plethora of states and transitions serves as a good playground for quantum optics [10, 39, 53, 108, 126, etc.].

Table 1.1 – Numerical values of the relevant states and transitions of $^{40}Ca^{+}$. The transition wavelengths were measured using a FIZEAU interferometer (model WS/7 of «HighFinesse GmbH») and are given for vacuum. Their uncertainties correspond to the interferometer's inaccuracy of 60 MHz. The last column gives the numbering of the transitions used in the Matlab programme of section 4.2 on p. 65.

level	lifetime	decay channel	wavelength	$A_i/2\pi$	no.
$P_{3/2}$	6.924(19) ns[52]	$\rightarrow D_{5/2}$	854.44337(15) nm	1.350(6) MHz[52]	6
		$\rightarrow D_{3/2}$	850.03561(14) nm	0.1520(9) MHz[52]	4
		$\rightarrow S_{1/2}$	393.48075(3) nm	21.49(6) MHz[52]	3
$P_{1/2}$	7.098(20) ns[52]	$\rightarrow D_{3/2}$	866.45211(15) nm	1.44(7) MHz[52, 100]	2
		$\rightarrow S_{1/2}$	396.95915(3) nm	20.97(7) MHz[52, 100]	1
$D_{5/2}$	1.168(9) s[57]	$\rightarrow S_{1/2}$	729.34765(11) nm	0.1363(10) Hz[57]	5
$D_{3/2}$	1.176(11) s[57]	$\rightarrow S_{1/2}$	732.5905(2) nm	0.1353(13) Hz[57]	0
$S_{1/2}$	stable				

In the experimental set-up, the $S_{1/2}$–$P_{1/2}$ transition is used for cooling the ion by a laser at 397 nm wavelength that is slightly red-detuned from the atomic resonance. In addition, a laser at 866 nm is used to pump the ion back from the $D_{3/2}$ manifold, which happens many orders of magnitude faster than the natural decay at the 732 nm transition. Both lasers are switched on also in the idle time between actual measurements or experimentation sequences as this cooling cycle is part of the trapping too. Above this Λ-shaped level system $S_{1/2}$–$P_{1/2}$–$D_{3/2}$ lies another Λ-system $S_{1/2}$–$P_{3/2}$–$D_{5/2}$ with nearly the same properties but more

Zeeman sub-levels. This one is used for the quantum logic with the advantage of separating the cooling and fluorescence detection from the logical operations. Note, that the two transitions at 397 nm and 393 nm wavelength are the blue Fraunhofer lines H and K, respectively [35]. Qualitatively, their level structure is the same as the well-known D_1 and D_2 lines of neutral sodium.

1.2.1 Photo-ionisation of calcium

The two natural occurrences of atomic calcium are neutral (Ca I) in solid state and doubly ionised (Ca III) in solution. To attain singly ionised calcium (Ca II) only one of the two valence electrons has to be removed from the neutral atom. In the experiment this is achieved in a two-step photo-ionisation process: From the ground state of Ca I, $[\mathrm{Ar}]\,4\,s^2$, a photon at 423 nm wavelength excites to $[\mathrm{Ar}]\,4\,sp$, and a second photon at 389 nm wavelength transfers one electron to a Rydberg state where the trap potential adds the tiny last bit of energy to ionise the atom to Ca II, precisely $[\mathrm{Ar}]\,4\,s$. For the first step a frequency-doubled diode laser is used, and for the second step a simple ultraviolet LED. Details are found in [110, p. 68 ff.].

1.3 Theory of ion trapping

> «In the first place it is fair to state
> that we are not experimenting
> with single particles …»
>
> — E. Schrödinger (1952)[109]

To use a single atomic ion as a quantum-mechanical test ground, it has to be wholly separated from the environment. To put this into practice, the research group, among many others, uses the linear type of the radio-frequency trap invented (and patented) by Wolfgang Paul in the year 1953 [86–89] as engine of choice. Facile in construction and very versatile in use, it brought him the Nobel prize in physics in 1989 [90]. Being placed in ultra-high vacuum, such a device is able to trap and confine single charged particles for long times, and thus, it serves as the fundamental building block for excellent high-precision spectrometers [84, 131].
It is impossible to trap a charged particle in a static electromagnetic field because of the lack of a global minimum in such a field, as dictated by Earnshaw's theorem [26]. In detail, the Laplace equation for the two electromagnetic potentials Φ and $\boldsymbol{A}$ shows that all extrema in free space are in fact saddle points. In

the PAUL trap this problem is solved through an oscillating field. It has equipotential planes in the shape of an elliptic hyperboloid (the so-called saddle potential) with an oscillating cross section. In the case of the linear type, this is achieved by four longitudinal electrodes, metallic rods or blades, arranged parallel to each other as the edges of a cuboid, at which two diagonally opposed electrodes carry the same voltage U_{RF} oscillating with a radio frequency ω_{RF}. This oscillating quadrupole potential in the cross section is superposed by a static electric potential U_{end} of two ring- or tiplike end electrodes that sit on the middle axis (see fig. 1.3).

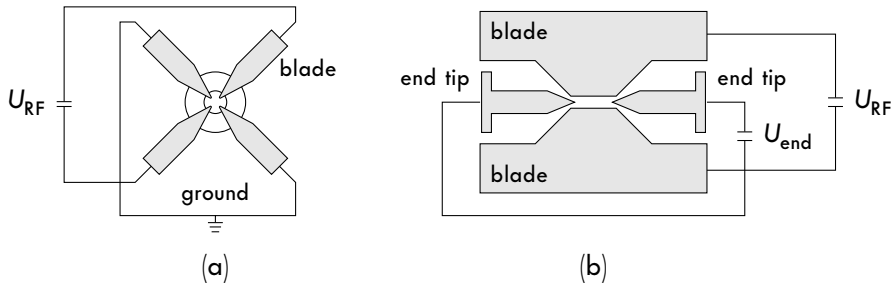

Figure 1.3 – Schematic drawings of the linear PAUL trap used in the experimental set-up: a) cross section through *x*-*y*-plane; b) side view, cut through two opposed blades.

The resulting total electric potential is approximated about the trap centre by

$$\Phi(x, y, z, t) = \frac{\alpha U_{end}}{2l_0^2}(2z^2 - x^2 - y^2) + \frac{U_{RF}}{2r_0^2}\cos(\omega_{RF}t)(x^2 - y^2) \qquad (1.5)$$

wherein the minimum distance of the trap centre to the end electrodes and to the longitudinal electrodes are denoted by l_0 and r_0, respectively. The trap geometry causes a shielding of the axial potential, which is conveyed by the numerical factor $\alpha < 1$. The equations of motion for each of the CARTESian coordinates of a charged particle in this potential (1.5) are MATHIEU differential equations [75]

$$\frac{d^2x_i}{d\phi^2} + (a_i - 2q_i\cos(2\phi))x_i = 0$$

with a phase $\phi = \frac{\omega_{RF}t}{2}$ as the variable and six dimensionless coefficients, a_i and q_i, called stability parameters. They are defined by

$$-a_x = -a_y = \frac{a_z}{2} = \frac{4Q\alpha U_{end}}{Ml_0^2\omega_{RF}^2} =: a, \qquad -q_x = q_y = \frac{2QU_{RF}}{Mr_0^2\omega_{RF}^2} =: q, \qquad q_z = 0$$

where Q and M denote the charge and mass of the particle, respectively.
In the case of $|a_i|, q_i^2 \ll 1$, the MATHIEU equations have stable solutions in which the particle's motion in each coordinate is a superposition of two oscillations,

$$x_i(t) \sim \cos(\omega_i t)\left(1 - \frac{q_i}{2}\cos(\omega_{RF} t)\right),$$

the so-called «micro-motion» with the fast, driving radio frequency ω_{RF} in the x-y-plane and the «secular motion» with a slower frequency,

$$\omega_x = \omega_y = \frac{\omega_{RF}}{2}\sqrt{\frac{1}{2}q^2 - a} =: \omega_r \qquad \text{or} \qquad \omega_z = \frac{\omega_{RF}}{2}\sqrt{a_z} = \sqrt{\frac{2Q\alpha U_{end}}{M l_0^2}},$$

in the x-y-plane and on the z-axis, respectively.

1.4 The twin ion engine

Q.: «Can you fly a TIE Fighter?»
A.: «I can fly anything.»

— Star Wars VII (2015)

To accomplish more complex experiments in the scope of quantum networks, e. g. showing interaction of two distant single ions [111], two identically constructed PAUL traps are set up separated by about one metre from each other in the same laboratory. They are referred to as «Dark Trap» (DT) and «Bright Trap» (BT) due to their change in colour after the first bake-out [104]. The design of the traps was developed at the «Leopold-Franzens-Universität Innsbruck» [40] in the mid-1990s. Its size parameters are $r_0 = 0.8\,\text{mm}$ and $l_0 = 2.5$ or $5\,\text{mm}$ according to eq. (1.5), and the geometric shielding factor unfolded to be $\alpha = 0.183$. With a typical static electric potential of $U_{end} = 400\,\text{V}$ the resulting axial secular frequency is $\omega_z = 2\pi \cdot 1.197\,\text{MHz}$. The radio frequency of $\omega_{RF} = 2\pi \cdot 26.133\,\text{MHz}$ with an amplitude of $U_{RF} = 1449\,\text{V}$ leads to the radial secular frequency, $\omega_r = 2\pi \cdot 3.647\,\text{MHz}$, and to the stability parameters, $a = 0.004$ and $q = 0.405$. These verify the case of stable oscillatory motion of the ion.
Initially, the twin ion engine (TIE) was set up at the «Institut de Ciències Fotòniques» (ICFO) in Barcelona. Detailed descriptions of that stage are given in the theses of Marc ALMENDROS, Felix ROHDE, and Carsten SCHUCK [3, 104, 110]. In the year 2010, the whole apparatus was moved to the «Universität des Saarlandes» (UdS) in Saarbrücken, and modified and improved over the following

years by Jan Huwer, Michael Schug, Christoph Kurz, Stephan Kucera, Pascal Eich [28, 47, 58, 62, 112], and the author.
All devices sensitive to acoustic noise are set up on optical tables actively damped by laminar air flow. Both vacuum chambers are mounted on one table, model ST of «Newport Corporation», all lasers are set up on another one, model RS 4000 of «Newport Corporation», except for the 854 nm laser that rests on the same table (by «Melles Griot») as the photon-pair source (sec. 1.5).

1.4.1 Vacuum vessels

Each Paul trap is mounted inside a separate chamber of ultra-high vacuum, hanging from the top CF-200 flange under an angle of 22.5° to the horizontal plane. Optical access is achieved through eight CF-63 ports in that plane, one CF-200 port at the bottom, and three small CF-16 ports on top with cut-outs through the mounting flange, for details see [110, p. 26–29]. The ultra-high vacuum (UHV) is reached and maintained without interruption over several years by a 50-liter ion pump, model IP-050 of «Thermionics Laboratory Inc.», after a necessary low pressure is reached by a titanium sublimation pump, model SB-1020 of the same company. Applying this procedure after a two-step bake-out of the vacuum chamber as described in [110, p. 242] a pressure below $5 \cdot 10^{-10}$ mbar is reached.
As a source of single calcium atoms two tubes of stainless steel, 60 mm long and 2 mm in diameter, filled with calcium powder are installed below each Paul trap. If one of them is heated up to 300–400°C by running an electric current of 4–6 A thought them, an atom beam of evaporated calcium flows through the trap centre. The other oven is just a reserve. With the activation of both, the photo-ionisation light sources according to section 1.2.1 and the trap potential, single $^{40}Ca^{+}$ ions are trapped within a few minutes.

1.4.2 Optical access

Together with each trap a pair of high-numerical-aperture laser objectives (HALOs) is mounted in-vacuum, and connected to the top flange by a three-dimensional translation stage[1] that allows the fine-adjustment of the focussing of the laser beams to the trap centre. The HALOs consist of four lenses especially designed[2] to be diffraction limited over the wide range of visible wavelengths, 400 nm to

1) This ANPxyz100 configuration of «attocube systems AG» consists of two ANPx and one ANPz translation stage stacked above each other.
2) The HALOs are designed by the company «Linos Photonics», for details see [110, p. 51–55].

870 nm, and to collect a reasonable portion of the solid angle. With an opening angle of 47.2° they cover 4.18 % of the solid angle corresponding to a numerical aperture (NA) of 0.4. Thus, the focal spot at the centre of the trap ranges from 1.2 µm at 393 nm wavelength to 2.6 µm at 866 nm wavelength [36]. This enables the separate optical access («addressing») of single ions in a string, both by laser excitation and by their emission (fig. 1.4).

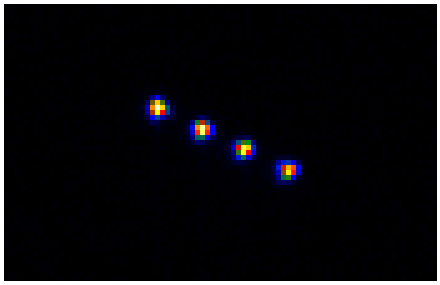

Figure 1.4 – Image of the first ion string trapped in Saarbrücken. This false-colour picture was taken on 26. 11. 2010 with the Andor camera (see sec. 1.4.4) detecting blue fluorescence of 397 nm wavelength of about 100 000 photons per second with optics focused to the centre of the trap (BT). The four trapped ions are visible as clearly separated single spots.

Any laser beam sent through one of the other view ports, without the strong focusing by the HALOs, illuminates all ions in the trap centre with almost equal strength. Typical focal spots range from 50 to 100 µm.

1.4.3 Magnetic field

Each trap is equipped with a set of magnetic coils outside of the vacuum vessel. These sets consist of three pairs of series-connected magnetic coils that provide three orthogonal static magnetic fields. One of them, usually the pair on the HALO axis, produces the main static magnetic field $\boldsymbol{B}_0$ that defines the quantisation axis of the ion (see p. 28) while the other two are weaker and provide compensation of the terrestrial field and of static stray fields, which is important for a controlled and stable orientation of the quantisation axis. With an electric current of about 3 A through the main pair a typical magnetic field of 280 µT is reached. The employed power supplies of model QL 355 of «Aim-TTi» have a long-term stability below 100 µA at 3 A leading to an expected contribution to the magnetic field noise just below 10 nT.
Another important part of magnetic field noise is attributed to dynamic stray fields emitted chiefly by the electronic devices of the laboratory itself. These show the power-line frequency of 50 Hz and its harmonics. Three additional smaller coils

are set-up for compensation of the dynamic stray fields, but only the one at the quantisation axis is used so far. A weak AC signal of sine components at 50 Hz and 150 Hz with fixed amplitudes and phases given by calibration measurements is applied to this coil. The signal is locked to the power line by a phase-locked loop (PLL). This compensation leads to an increase of the ion's coherence time from 97 µs to 204 µs at the RF transition in the $S_{1/2}$, measured through RAMSEY interferometry [101]. Details are given in the master thesis of Matthias KREIS [56].

1.4.4 Photon detection

The detection of single photons is a crucial point in quantum-optics experiments. Photons emitted by the calcium ion are sent either via optical fibre cables to single-photon detectors shielded in lightproof boxes for fast and efficient detection or to a highly sensitive camera for spatial resolution.
The blue photons emitted at the fluorescence transitions of 393 nm or 397 nm wavelength are sent through a multi-mode fibre with about 85 % transmission efficiency into photo-multiplying tubes (PMT). With the model «H7422P-40 SEL» of «Hamamatsu Photonics K. K.» quantum efficiencies of 25 and 28(1) % are achieved. The temporal spread of the electric signals that correspond to single-photon detections is specified to be 280 ps. Taken the cooling cycle of a single trapped ion as an example (see sec. 1.2), a detected fluorescence rate of slightly more than 200 000 clicks per second is achievable under optimised conditions for high emission. This almost reaches the possible maximum for steady-state conditions estimated as follows: Under strong excitation all eight participating ZEEMAN sub-levels (of $S_{1/2}$, $P_{1/2}$, $D_{3/2}$) are equally populated leading to the maximal population of the $P_{1/2}$ of $\frac{2}{8}$ (see figure 1.2). Multiplying this with the EINSTEIN *A*-coefficient of the transition, $2\pi \cdot 20.97(7)$ MHz, and with the efficiencies of photon collection, coupling, and detection, results in an estimated maximum of 320 000 clicks per second.
The infrared photons are guided through single-mode fibres with about 60 % efficiency onto avalanche photodiodes (APD), model «COUNT-10C-FC» of «Laser Components», with a detection efficiency of 24(5) % and a low dark-count rate of about 30/s.
For spatial resolution an electron-multiplying charge-coupled device (EMCCD), camera model «iXon DV887DCS-BV», serial number X-1602, from «Andor Technology Ltd.» is used. The ion's fluorescence light collected by a HALO is magnified by an optical telescope by a factor of 20. Thus, the size of a camera pixel of 16 µm corresponds to 800 nm resolution in the object plane of the ion as depicted in figure 1.4.

1.4.5 Coherent light sources

To address all five electric dipole transitions and the quadrupole transition at 729 nm mentioned above, six commercial diode lasers with additional, home-build stabilisation are used. All of these are extended-cavity diode lasers (ECDL) with a grating in Littrow configuration for the optical feedback, developed by «Toptica Photonics AG» [102]. Depending on the wavelength different models are in use; these are «DL 100» for 852 nm and 846 nm, «DL pro» for 850 nm, 866 nm, and 393 nm, «TA pro» for 729 nm, and «TA-SHG pro» for 397 nm and 854 nm. Their fundamental optical frequency has a narrow spectral linewidth of about 150 kHz in free-running mode (for a integration over 5 µs). The abbreviation SHG means second-harmonic generation. These models are diode lasers at the fundamental wavelengths 794 nm and 854 nm, respectively, that are frequency doubled to 397 nm and 427 nm by a non-linear crystal (in a $\chi^{(2)}$ process) in a folded ring cavity. In the case of the 854 nm laser a portion of the fundamental beam is sent directly to the ion while the SHG light of 427 nm wavelength is used as the source of photon pairs at 854 nm in another set-up, see section 1.5. Each laser is frequency stabilised via a so-called transfer resonator, see section 1.4.6 and [103], to the same reference laser of 852 nm wavelength that itself is stabilised to the $S_{1/2}$–$P_{3/2}$ transition of caesium by saturated absorption in a vapour cell.
As the light of 729 nm wavelength is used to drive the $S_{1/2}$–$D_{5/2}$ quadrupole transition in $^{40}Ca^{+}$ with a natural linewidth of only 136 mHz (see section 1.2 on p. 11), more effort has to be put into the frequency stabilisation of that laser. The main part of this is owed to Jan Huwer and well documented in his thesis [47]. The laser is stabilised to an ultra-stable resonator made of ultra-low expansion glass (ULE) that has a high finesse of 480 000 and a spectral linewidth of 4.034(5) kHz. Together with the Pound–Drever–Hall technique (PDH), see section 1.4.6, and a high-speed control amplifier, model «FALC», the linewidth of the laser light is reduced below 32(2) Hz.
In addition, as part of the photo-ionisation (sec. 1.2.1 on p. 13) a laser of 846 nm wavelength is used. This one is not stabilised, but tuned manually to the proper wavelength where it stays for the duration of some minutes needed for the trapping. Its light, about 130 mW, is frequency doubled to 423 nm wavelength by single-pass second-harmonic generation, sending it through a periodically poled crystal of potassium titanyl phosphate ($KTiOPO_4$).
Acousto-optical modulators (AOM) are used to fine-tune the frequencies of the lasers in the MHz-regime as well as to control their amplitude and phase sent into the ion trap. A special kind of AOM, an acousto-optic deflector (AOD), is used to address single sites of an ion string, which is mandatory for the effective

operation of multi-ion quantum gates.

A special source of electromagnetic radiation is used to drive the magnetic dipole transition in the $S_{1/2}$ ground-state manifold. It is an LC circuit consisting of a tunable capacitor and a simple two-winding copper-wire coil underneath the bottom flange of the vacuum vessel, which transmits the applied radio frequency (RF) as an electromagnetic wave to the ion. The coil has a diameter of 16 cm and its centre is 8 cm below the ion's position in the trap, see figure 2.4 on p. 40. A radio frequency equal to $g_S \mu_B B_0 / h$, i. e. 8 MHz for an RF amplitude of $B_0 \approx 300\,\mu\text{T}$, is resonant with the transition between the two ZEEMAN sub-levels in $S_{1/2}$. Details to this RF coil are given in [62, p. 50 ff.]. Both traps are equipped with such a device.

1.4.6 Laser stabilisation

To excite an atomic transition by laser light in a fully controlled way the laser needs to have a linewidth comparable to, but lower than the natural linewidth of the transition and a stable optical frequency, both over the course of a whole experimental sequence (or even a whole measurement day). The first is achieved by locking the laser to a FABRY–PÉROT cavity with the POUND–DREVER–HALL technique (PDH) [9, 24], and the second by locking this cavity to a stable reference. Therefore, these cavities are called transfer resonators.
As mentioned above the primal reference for frequency stability is the $S_{1/2}$–$P_{3/2}$ transition of caesium at 852.347 275 82(27) nm [124]. By DOPPLER-free absorption spectroscopy in a caesium vapour cell at room temperature the first transfer resonator is used to lock the 852 nm laser to this reference. All other lasers use that laser as reference and are locked to it by their individual transfer resonators. This active laser-stabilisation scheme was introduced at ICFO in the starting time of the research group, for more details see [3, 103, 104].

1.5 Photon-pair sources

As a resource of quantum-mechanical entanglement, a source of photon pairs based on spontaneous parametric down-conversion (SPDC) is set up in the same laboratory.
In a non-linear optical medium, such as periodically poled potassium titanyl phosphate ($KTiOPO_4$), the dielectric polarisation $\boldsymbol{P}$ does not only depend linearly on

the electric field $\boldsymbol{E}$ but also on higher orders,

$$\boldsymbol{P} = \varepsilon_0 \left(\chi^{(1)} \boldsymbol{E} + \chi^{(2)} \boldsymbol{E}^2 + \chi^{(3)} \boldsymbol{E}^3 + \ldots \right),$$

wherein $\chi^{(n)}$ are tensors of $(n+1)$-th order that represent the electric susceptibilities of n-th order, respectively. Quantum field theory tells that the second order, due to its $\boldsymbol{E}^2$-dependence, induces two-photon processes in the quantum regime. One of these is the spontaneous parametric down-conversion or parametric fluorescence where a single photon with frequency ω_{in} and wave vector $\boldsymbol{k}_{\text{in}}$ entering the non-linear medium is transformed into a pair of two photons with frequencies ω_i and wave vectors $\boldsymbol{k}_i$. The conservation of energy and momentum are reflected in the so-called phase-matching conditions,

$$\hbar\omega_{\text{in}} = \hbar\omega_1 + \hbar\omega_2 \qquad \text{and} \qquad \hbar\boldsymbol{k}_{\text{in}} = \hbar\boldsymbol{k}_1 + \hbar\boldsymbol{k}_2.$$

These cause the resulting photons of a pair to be entangled both in frequency and propagation direction. Due to the conservation of angular momentum they are additionally entangled in polarisation. In the case of periodically poled $KTiOPO_4$ (with a certain arrangement of regularly spaced layers of alternating ferro-electric orientation) the photon pair is in the maximally entangled singlet state,

$$|\Psi^-\rangle = \frac{1}{\sqrt{2}} \left(|1_H 1_V\rangle - |1_V 1_H\rangle \right),$$

that is often sloppily deemed the Bell state of orthogonal (linear) polarisation. This kind of SPDC is called type II.

Two such photon-pair sources are set up and operated in the laboratory. The early experiments were conducted using the source described in [41, 93, 94]. With a maximal pump power of 70 mW of the blue laser beam (at 427 nm wavelength) it produces about 5 600 photon pairs per second. Filtered to the atomic bandwidth of about 22 MHz this corresponds to a spectral brightness of 3.6/(s MHz mW) for single-mode fibre-coupled photon pairs. Their polarisation entanglement has a concurrence of 94.8(1.5) %.

Later experiments use a new photon-pair source, set up by Stephan Kucera [59] with a much higher output through resonator enhancement, and augmented by Jan Arensk̈otter [4] with a bidirectional pumping scheme to improve purity and entanglement of the pair state. At a 427 nm pump power of 40 mW it produces 1.8(2) million photon pairs per second with a concurrence of 98.3(5) % and a purity of 97.1(9) % [60]. In addition to the enhancement the resonator acts as a filter reducing the linewidth of the photons to 9.43(1) MHz, already compatible with the calcium transition at 854 nm. This leads to a spectral brightness of $4.8(5) \cdot 10^3$ photons per s MHz mW.

1.6 Experiment control

To perform complex experimental protocols consisting of sequences of many short and precise pulses of several lasers and RF sources sent to the ion traps, the whole experimental apparatus has to be controlled by a single device. It was the main part of Marc Almendros' thesis [3] to develop and build such a pulse sequencer, the «Hydra».
Its prototype version is a modular backplane-based bus system consisting of a digital signal processor (DSP) connected to several digital input–output cards and RF-generator cards. The DSP has a clock frequency of 1 GHz, and is stabilised to a rubidium atomic clock, model FS725 of «Stanford Research Systems». Each RF-generator card includes a field-programmable gate array (FPGA) and a direct digital synthesiser (DDS) to generate RF pulses that are arbitrary in amplitude, duration, frequency, and phase down to a resolution of 12.5 ns (due to the update rate of 80 MHz). Up to 13 RF signals are generated simultaneously and sent to the AOMs to be transformed into laser pulses as mentioned above. Some cards include an analogue input channel that uses the signal of a photodiode to stabilise the optical power of the laser beam. The user controls Hydra through the HydraPC software, a programme written in C++ and installed on a conventional computer.
As this prototype lacks the ability to temporally resolve the clicks of single-photon detectors, a commercial time-correlated pulse counter, model PicoHarp 300 of «PicoQuant» with a maximal resolution of 4 ps, is used.
Now, already the next generation, Hydra-II, is installed in the laboratory. It is a commercial device by «Signadyne», a spin-off company that was founded by Marc Almendros in 2010, and by now is part of «Keysight Technologies». Is has the advantage of directly processing the single-photon-detection inputs with a time-tag resolution of 320 ps that enables even more complex sequences including the reaction to single photons in a phase-dependent manner. Additionally, it has a higher RF-pulse resolution of 1.25 ns. Its user-friendly control programme, made by the author and others, is a graphical user interface (GUI) written in Matlab of «The MathWorks, Inc.» that interprets between the internal software made by «Signadyne» and the experimenter.
To be able to use the analogue signals of the photodiodes for intensity stabilisation of the laser beams they have to be digitised as Hydra-II has no analogue input channels. This is achieved by a single external custom-made analogue input card called «Karkinos», developed by Stephan Kucera as his diploma thesis [58].

All these control devices together enabled more and more automation of the

experiment over the past years, for a detailed example see [59]. This complex and extensive set-up makes the sophisticated experiments presented in this thesis practically feasible in the first place.

Chapter 2

Interaction of light and matter

«Sweet exists by convention,
and bitter by convention,
... colour by convention;
but in reality, atoms and the void alone exist.»

— Democritus (about 400 BC)

In this chapter, the general interaction of charged matter with the electromagnetic field is approximated to adapt to the situation of a single isolated ion in the presence of laser light. This is done in a semiclassical approach: The ion is treated as a hydrogen-like atom in the widespread comprehension of quantum-mechanical atom physics, while the laser light is considered as classical, electromagnetic plane waves.
First, the multipole expansion of the electromagnetic field about the centre of mass is carried out, which leads to the energy terms driving the individual transitions in the ion. Then, one such elemental transition is studied exemplarily in detail as a two-level model. Including additional approximations this leads to a very general Hamilton operator (2.8) that serves as a building block for the complex dynamics covered in chapter 4. Special attention to the influence of the geometry on the interaction completes this chapter.

2.1 The multipole expansion

Singly ionised calcium-40 is modelled as a hydrogen-like atom. It consists of two charged particles: the atomic core $^{40}Ca^{+}$ with closed electron shells, and the single valence electron e^{-}. Both have three spatial degrees of freedom, say their position coordinates, $\hat{\boldsymbol{r}}_c = (\hat{x}_c, \hat{y}_c, \hat{z}_c)$ for the core and $\hat{\boldsymbol{r}}_e = (\hat{x}_e, \hat{y}_e, \hat{z}_e)$ for the valence electron. These are written with a circumflex to indicate them as quantum-mechanical observables. As the core consists of an even–even nucleus and a closed shell of 18 electrons, its residual spin is zero. Thus, the only additional degree of freedom is the valence electron's spin as the total spin of the system with the quantum number $S = \frac{1}{2}$.
As the core is several orders of magnitude heavier than the electron ($m_c \gg m_e$), it is favourable to transform the coordinate system into the one of the centre of mass,

$$\hat{\boldsymbol{R}} = \frac{m_c \hat{\boldsymbol{r}}_c + m_e \hat{\boldsymbol{r}}_e}{m_c + m_e} \approx \hat{\boldsymbol{r}}_c,$$

wherein the total mass $M = m_c + m_e$ is at rest, and the electron with the reduced mass $m = \frac{m_c m_e}{m_c + m_e}$ has the relative coordinate $\hat{\boldsymbol{r}} = \hat{\boldsymbol{r}}_e - \hat{\boldsymbol{r}}_c$. The two position vectors transform according to

$$\hat{\boldsymbol{r}}_e = \hat{\boldsymbol{R}} + \frac{m_c}{M}\hat{\boldsymbol{r}} \qquad \text{and} \qquad \hat{\boldsymbol{r}}_c = \hat{\boldsymbol{R}} - \frac{m_e}{M}\hat{\boldsymbol{r}} \tag{2.1}$$

and their momenta to

$$\hat{\boldsymbol{p}}_e = \frac{m_e}{M}\hat{\boldsymbol{P}} + \hat{\boldsymbol{p}} \qquad \text{and} \qquad \hat{\boldsymbol{p}}_c = \frac{m_c}{M}\hat{\boldsymbol{P}} - \hat{\boldsymbol{p}} \tag{2.2}$$

into the momentum $\hat{\boldsymbol{P}}$ of the total mass and the momentum $\hat{\boldsymbol{p}}$ of the reduced mass, which is directly linked to the relative velocity,

$$\hat{\boldsymbol{v}} = \frac{\hat{\boldsymbol{p}}}{m} = \frac{\hat{\boldsymbol{p}}_e}{m_e} - \frac{\hat{\boldsymbol{p}}_c}{m_c}.$$

Following the general Pauli equation [91], the Hamilton operator for two charged particles (one without spin; the other with spin $\frac{1}{2}$) in an external electromagnetic field defined by the potentials Φ and $\boldsymbol{A}$ is

$$\hat{H} = \frac{\left(\hat{\boldsymbol{p}}_c - q_c \boldsymbol{A}(\hat{\boldsymbol{r}}_c, t)\right)^2}{2m_c} + \frac{\left(\hat{\boldsymbol{\sigma}} \cdot \left(\hat{\boldsymbol{p}}_e - q_e \boldsymbol{A}(\hat{\boldsymbol{r}}_e, t)\right)\right)^2}{2m_e} + q_c \Phi(\hat{\boldsymbol{r}}_c, t) + q_e \Phi(\hat{\boldsymbol{r}}_e, t) + \frac{q_c q_e}{4\pi\varepsilon_0 \left|\hat{\boldsymbol{r}}_e - \hat{\boldsymbol{r}}_c\right|},$$

wherein the PAULI operator $\hat{\boldsymbol{\sigma}}$ (see eq. (1.2) on p. 8) pays tribute to the electron spin; the first two terms are the kinetic energies of the two particles with the canonical momenta, the third and fourth term denote the potential energy in the external electric field, and the last term is the energy of the interaction of the two particles. Here, the two potentials are no operators as the electromagnetic field is treated classically in the following sections. With the TAYLOR expansions of the external electric and magnetic field about the centre of mass,

$$\boldsymbol{E}(\hat{\boldsymbol{R}} + \hat{\boldsymbol{\varepsilon}}, t) = \sum_{k=0}^{\infty} \frac{1}{k!} (\hat{\boldsymbol{\varepsilon}} \cdot \hat{\boldsymbol{\nabla}}_{\boldsymbol{R}})^k \boldsymbol{E}(\hat{\boldsymbol{R}}, t),$$
$$\boldsymbol{B}(\hat{\boldsymbol{R}} + \hat{\boldsymbol{\varepsilon}}, t) = \sum_{k=0}^{\infty} \frac{1}{k!} (\hat{\boldsymbol{\varepsilon}} \cdot \hat{\boldsymbol{\nabla}}_{\boldsymbol{R}})^k \boldsymbol{B}(\hat{\boldsymbol{R}}, t),$$

the potentials transform to

$$\Phi(\hat{\boldsymbol{R}} + \hat{\boldsymbol{\varepsilon}}, t) = \Phi(\hat{\boldsymbol{R}}, t) - \hat{\boldsymbol{\varepsilon}} \cdot \sum_{k=0}^{\infty} \frac{1}{(k+1)!} (\hat{\boldsymbol{\varepsilon}} \cdot \hat{\boldsymbol{\nabla}}_{\boldsymbol{R}})^k \boldsymbol{E}(\hat{\boldsymbol{R}}, t),$$
$$\boldsymbol{A}(\hat{\boldsymbol{R}} + \hat{\boldsymbol{\varepsilon}}, t) = -\frac{1}{2} \hat{\boldsymbol{R}} \times \boldsymbol{B}(\hat{\boldsymbol{R}}, t) - \hat{\boldsymbol{\varepsilon}} \times \sum_{k=0}^{\infty} \frac{1}{(k+2)k!} (\hat{\boldsymbol{\varepsilon}} \cdot \hat{\boldsymbol{\nabla}}_{\boldsymbol{R}})^k \boldsymbol{B}(\hat{\boldsymbol{R}}, t),$$

fulfilling $\hat{\boldsymbol{E}} = -\hat{\boldsymbol{\nabla}}\hat{\Phi} - \partial_t \hat{\boldsymbol{A}}$ and $\hat{\boldsymbol{B}} = \hat{\boldsymbol{\nabla}} \times \hat{\boldsymbol{A}}$. Hence, inserting the coordinate transformation, eq. (2.1) and eq. (2.2), results in

$$\hat{H} = \frac{\hat{\boldsymbol{P}}^2}{2M} + \frac{\hat{\boldsymbol{p}}^2}{2m} + Q\Phi(\hat{\boldsymbol{R}}, t) - q\hat{\boldsymbol{r}} \cdot \boldsymbol{E}(\hat{\boldsymbol{R}}, t) - \frac{q_{\text{red}}}{2} \hat{\boldsymbol{r}} \cdot (\hat{\boldsymbol{r}} \cdot \operatorname{grad} \boldsymbol{E}(\hat{\boldsymbol{R}}, t)) + \mathcal{O}(|\hat{\boldsymbol{r}}|^3)$$
$$+ \hat{H}_{\text{dia}} - \hat{\boldsymbol{\mu}}_L \cdot \boldsymbol{B}(\hat{\boldsymbol{R}}, t) - \hat{\boldsymbol{\mu}}_S \cdot \boldsymbol{B}(\hat{\boldsymbol{R}}, t) + \frac{q_c q_e}{4\pi\varepsilon_0 |\hat{\boldsymbol{r}}|} \quad (2.3)$$

for the HAMILTON operator. The introduced parameters are the total charge Q, the so-called interaction charge q, and the reduced charge q_{red},

$$Q = q_c + q_e, \qquad q = \frac{q_c m_e - q_e m_c}{M}, \qquad q_{\text{red}} = \frac{q_c m_e^2 + q_e m_c^2}{M^2},$$

as well as the magnetic moments,

$$\hat{\boldsymbol{\mu}}_L = \frac{q_c}{2m_c} \hat{\boldsymbol{L}}_c + \frac{q_e}{2m_e} \hat{\boldsymbol{L}}_e \qquad \text{and} \qquad \hat{\boldsymbol{\mu}}_S = \frac{q_e}{2m_e} g_S \hat{\boldsymbol{S}},$$

with the orbital angular momenta $\hat{\boldsymbol{L}}_c = \hat{\boldsymbol{r}}_c \times \hat{\boldsymbol{p}}_c$ and $\hat{\boldsymbol{L}}_e = \hat{\boldsymbol{r}}_e \times \hat{\boldsymbol{p}}_e$, and the spin angular momentum $\hat{\boldsymbol{S}} = \frac{\hbar}{2} \hat{\boldsymbol{\sigma}}$.

In the scope of perturbation theory, the trap potential $\Phi(\hat{\boldsymbol{R}}, t)$ together with the static portion $\boldsymbol{B}_0$ of the magnetic field $\boldsymbol{B}(\hat{\boldsymbol{R}}, t)$, and all terms independent of the external fields are treated as the unperturbed HAMILTONian,

$$\hat{H}_0 = \underbrace{Q\Phi(\hat{\boldsymbol{R}}, t) + \frac{\hat{\boldsymbol{P}}^2}{2M}}_{=:\hat{H}_T \text{ harm. oscillator}} + \overbrace{\underbrace{\frac{\hat{\boldsymbol{p}}^2}{2m} + \frac{q_c q_e}{4\pi\varepsilon_0 |\hat{\boldsymbol{r}}|}}_{\text{H-like atom}} - \hat{\boldsymbol{\mu}}_J \cdot \boldsymbol{B}_0}^{=:\hat{H}_A}, \tag{2.4}$$

where the first two terms determine the motion of the entire ion in the external trap potential $\Phi(\hat{\boldsymbol{R}}, t)$ as discussed in section 1.3, while the third and fourth term give rise to the behaviour of a hydrogen-like atom at the centre of mass. The last term containing the operator of the total magnetic moment $\hat{\boldsymbol{\mu}}_J = \hat{\boldsymbol{\mu}}_L + \hat{\boldsymbol{\mu}}_S$ generates the ZEEMAN splitting, which defines the direction of $\boldsymbol{B}_0$ as the axis of quantisation. This formula shows a separation of the seven degrees of freedom into two sub-systems, the external motion of the coordinate $\hat{\boldsymbol{R}}$ and the internal dynamics of $\hat{\boldsymbol{r}}$ and $\hat{\boldsymbol{S}}$. In the quantum regime, the first one governs the phononic excitation of the centre of mass as a three-dimensional harmonic oscillator $\hat{H}_T$ with eigenfrequencies ω_x, ω_y, and ω_z, and with the phonon numbers n_x, n_y, and n_z as the external degrees of freedom. The second sub-system $\hat{H}_A$ governs the electronic state of the ion with the four quantum numbers of the atomic orbitals as the internal degrees of freedom, n, L, J, and m_J (since S is fixed). Hence, the eigenstates of $\hat{H}_0$ are written as the tensor product of the eigenstates of $\hat{H}_A$ and $\hat{H}_T$, i. e. $|n, L, J, m_J\rangle$ and $|n_x, n_y, n_z\rangle$, respectively.

The terms quadratic in the electromagnetic field are summarised in $\hat{H}_{\text{dia}} \sim \boldsymbol{A}^2$ and are neglected in the regime of weak fields. All other terms are linear in the field strengths and govern the interactions between the ion and the fields such as laser beams. These are treated as perturbations. The two lowest orders in $\hat{\boldsymbol{r}}$ are of great interest for the excitation of the ion in the laboratory. The term of the lowest order is the interaction of the electric dipole moment $\hat{\boldsymbol{d}} = q\hat{\boldsymbol{r}}$ with the electric field at the centre of mass,

$$\hat{H}_{\text{E1}} = -\hat{\boldsymbol{d}} \cdot \boldsymbol{E}(\hat{\boldsymbol{R}}, t). \tag{2.5}$$

The second order consists of two terms, one is the interaction of the electric quadrupole moment $\hat{Q}_{ij} = q_{\text{red}}(3\hat{x}_i\hat{x}_j - \delta_{ij}\hat{\boldsymbol{r}}^2)$ with the gradient of the electric field,

$$\hat{H}_{\text{E2}} = -\tfrac{1}{6}\,\text{tr}(\hat{Q} \cdot \text{grad}\, \boldsymbol{E}(\hat{\boldsymbol{R}}, t)),$$

and the other is the interaction of the magnetic dipole moment $\hat{\boldsymbol{\mu}}_J$ with the dynamical part of the magnetic field $\boldsymbol{B}_{\text{dyn}}(\hat{\boldsymbol{R}}, t) = \boldsymbol{B}(\hat{\boldsymbol{R}}, t) - \boldsymbol{B}_0$,

$$\hat{H}_{M1} = -\hat{\boldsymbol{\mu}}_J \cdot \boldsymbol{B}_{\text{dyn}}(\hat{\boldsymbol{R}}, t).$$

Each of the higher orders $\mathcal{O}(|\hat{\boldsymbol{r}}|^3)$ brings three additional terms, a higher electric and magnetic multipole moment as well as a moment of the displacement current. For details on these see [74].

Remark: The presented treatment is done non-relativistically because all relativistic corrections, e. g. LAMB shift and spin–orbit coupling, do not change the level structure qualitatively, only additional energy shifts come into play. These are already included in the fine-structure splitting given in section 1.2 on p. 11. The same argument holds for the atomic structure of the closed inner electron shells, whose interaction with the valence electron gives the largest contribution to the fine structure.

2.2 The two-level system

To determine the properties of the transitions in the atom in a general manner, a single transition between two eigenstates $|\psi\rangle = |n, L, J, m_J\rangle|n_x, n_y, n_z\rangle$ and $|\psi'\rangle = |n', L', J', m_{J'}\rangle|n'_x, n'_y, n'_z\rangle$ of the unperturbed system is picked out and this subsystem is treated as a closed two-level system. In addition to the above-mentioned multipole expansion two other approximations are applied, as describes in the following, the LAMB–DICKE assumption and the rotating-wave approximation. With the eigenenergies $\hbar\omega_0$ and $\hbar\omega'_0$ of these two states the corresponding HAMILTON operator of the unperturbed reduced two-level system is

$$\hat{H}_0 = \hbar \begin{pmatrix} \omega_0 & 0 \\ 0 & \omega'_0 \end{pmatrix} = \hbar \begin{pmatrix} \omega_A + \boldsymbol{n} \cdot \boldsymbol{\omega}_T + \frac{\omega_{\text{sum}}}{2} & 0 \\ 0 & \omega'_A + \boldsymbol{n}' \cdot \boldsymbol{\omega}_T + \frac{\omega_{\text{sum}}}{2} \end{pmatrix}$$

in the basis of $|\psi\rangle$ and $|\psi'\rangle$. Herein, the parameters of the harmonic oscillator are combined into the vectors $\boldsymbol{n} = (n_x, n_y, n_z)$, $\boldsymbol{n}' = (n'_x, n'_y, n'_z)$, and $\boldsymbol{\omega}_T = (\omega_x, \omega_y, \omega_z)$, and the scalar $\omega_{\text{sum}} = \omega_x + \omega_y + \omega_z$. The natural frequency of the atomic transition including the ZEEMAN shifts due to $\boldsymbol{B}_0$ is $\omega_{12} := \omega'_A - \omega_A$, excluding the change in phonon numbers.
From now on, the system is described in the interaction picture defined by the

unitary transformation based on $\hat{H}_0$,

$$\hat{U} = e^{-\frac{i}{\hbar}\hat{H}_0 t} = \begin{pmatrix} e^{-i(\omega_A + \boldsymbol{n}\cdot\boldsymbol{\omega}_T + \frac{\omega_{sum}}{2})t} & 0 \\ 0 & e^{-i(\omega'_A + \boldsymbol{n}'\cdot\boldsymbol{\omega}_T + \frac{\omega_{sum}}{2})t} \end{pmatrix}.$$

The eigenstates in the interaction picture are written $|\psi_A\rangle = \hat{U}^+|n, L, J, m_J\rangle$, $|\psi'_A\rangle = \hat{U}^+|n', L', J', m'_J\rangle$, $|\psi_T\rangle = \hat{U}^+|\boldsymbol{n}\rangle$, and $|\psi'_T\rangle = \hat{U}^+|\boldsymbol{n}'\rangle$.
The interaction between the two states is governed by one of the multipole terms, $\hat{H}_{E1}$, $\hat{H}_{E2}$, or $\hat{H}_{M1}$, depending on the selection rules, see section 2.3.

2.2.1 Classical laser field

The light of each laser beam sent to the ion is treated classically as a plane electromagnetic wave. Its vector potential is described by

$$\boldsymbol{A}(\hat{\boldsymbol{R}}, t) = A_0 \boldsymbol{u} \sin(\boldsymbol{k}\cdot\hat{\boldsymbol{R}} - \omega t) \tag{2.6}$$

with the propagation direction given by the wave vector $\boldsymbol{k}$, and an angular frequency of $\omega = c|\boldsymbol{k}|$. The polarisation direction is given by the unit vector $\boldsymbol{u}$, which is perpendicular to $\boldsymbol{k}$. Its exact form is treated in section 2.3. The amplitude A_0 is related to the square root of the laser intensity at the place of the atom. From eq. (2.6) follows the electric field of the laser,

$$\boldsymbol{E}(\hat{\boldsymbol{R}}, t) = A_0 \omega \boldsymbol{u} \cos(\boldsymbol{k}\cdot\hat{\boldsymbol{R}} - \omega t),$$

which drives the electric dipole moment of the atom as depicted by eq. (2.5). This leads to the off-diagonal matrix element,

$$\begin{aligned}
E_{21} &= \langle\psi'|\hat{H}_{E1}|\psi\rangle = -\langle n', L', J', m'_J|\hat{\boldsymbol{d}}|n, L, J, m_J\rangle \cdot \langle\boldsymbol{n}'|\boldsymbol{E}(\hat{\boldsymbol{R}}, t)|\boldsymbol{n}\rangle \\
&= -\langle n', L', J', m'_J|\hat{U}\hat{U}^+\hat{\boldsymbol{d}}\hat{U}\hat{U}^+|n, L, J, m_J\rangle \cdot \langle\boldsymbol{n}'|\hat{U}\hat{U}^+\boldsymbol{E}(\hat{\boldsymbol{R}}, t)\hat{U}\hat{U}^+|\boldsymbol{n}\rangle \\
&= -\langle\psi'_A|\hat{U}^+\hat{\boldsymbol{d}}\hat{U}|\psi_A\rangle \cdot \langle\psi'_T|\hat{U}^+\boldsymbol{E}(\hat{\boldsymbol{R}}, t)\hat{U}|\psi_T\rangle \\
&= -\langle\psi'_a|\hat{\boldsymbol{d}}e^{i(\omega'_A - \omega_A)t}|\psi_A\rangle \cdot \langle\psi'_T|\boldsymbol{E}(\hat{U}^+\hat{\boldsymbol{R}}\hat{U}, t)|\psi_T\rangle \\
&= -\langle\psi'_A|\hat{\boldsymbol{d}}|\psi_A\rangle e^{i\omega_{12}t} \cdot \langle\psi'_T|\boldsymbol{E}(\hat{\boldsymbol{R}}(t), t)|\psi_T\rangle \\
&= -\boldsymbol{d}_{12}e^{i\omega_{12}t} \cdot A_0\omega\boldsymbol{u}\frac{1}{2}\left(\langle\psi'_T|e^{i\boldsymbol{k}\cdot\hat{\boldsymbol{R}}(t)}|\psi_T\rangle e^{-i\omega t} + \langle\psi'_T|e^{-i\boldsymbol{k}\cdot\hat{\boldsymbol{R}}(t)}|\psi_T\rangle e^{i\omega t}\right),
\end{aligned}$$

with the electric-dipole matrix element $\boldsymbol{d}_{12} := \langle\psi'_A|\hat{\boldsymbol{d}}|\psi_A\rangle$. The constant pre-factor $-|\boldsymbol{d}_{12}|A_0\omega$ is abbreviated by $\hbar\Omega_{E1}$ introducing the Rabi frequency Ω_{E1} of the ideal case of a point-like atom. The directional dependence $(\boldsymbol{d}_{12}\cdot\boldsymbol{u})$ leads to geometrical factors that are discussed below in section 2.3.

2.2.2 The Lamb–Dicke regime

The remaining brackets are solved by expressing the position operators through the creation and annihilation operators of the harmonic oscillator in the interaction picture, $\hat{R}_i(t) = R_{0,i}(\hat{a}_i^+(t) + \hat{a}_i(t))/\sqrt{2}$ with $\hat{a}_i(t) = \hat{a}_i e^{-i\omega_i t}$, and applying the Taylor expansion. This leads to

$$\left\langle \psi_T' \middle| e^{i\boldsymbol{k}\cdot\hat{\boldsymbol{R}}(t)} \middle| \psi_T \right\rangle = e^{i\Delta\boldsymbol{n}\cdot\boldsymbol{\omega}_T t} \underbrace{e^{-\frac{\eta^2}{2}} \prod_{i=1}^{3} \sqrt{\frac{n_{i,\max}!}{n_{i,\min}!}} \sum_{m=0}^{n_{i,\min}} \binom{n_{i,\min}}{m} \frac{(i\eta_i)^{|\Delta n_i|+2m}}{(|\Delta n_i| + m)!}}_{=:\frac{\Omega_{\boldsymbol{n},\boldsymbol{n}'}}{\Omega_{E1}}}$$

with $n_{i,\min}$ and $n_{i,\max}$ being the minimum and maximum of n_i and n_i', respectively, and $\Delta n_i = n_i' - n_i$. The three dimensionless numbers $\eta_i = k_i R_{0,i}/\sqrt{2}$ are called Lamb–Dicke parameters. In the case that the extension of the atomic wave packet is much smaller than the wavelength of the exciting light, i. e. if $\langle(\boldsymbol{k}\cdot\hat{\boldsymbol{R}})^2\rangle \ll 1$, only the leading order of η_i is relevant, thus

$$\Omega_{\boldsymbol{n},\boldsymbol{n}'} \sim e^{-\frac{\eta^2}{2}} \prod_{i=1}^{3} \eta_i^{|\Delta n_i|},$$

and transitions with a big change $|\Delta\boldsymbol{n}| \gg 1$ in phonon numbers are suppressed. This is called Lamb–Dicke regime. In this case the transition with $\Delta\boldsymbol{n} = 0$, the carrier transition, is the strongest one. It is resonant to the natural atomic frequency ω_{12} and has the coupling strength $\Omega_{\boldsymbol{n},\boldsymbol{n}} = \Omega_{E1}\exp(-\boldsymbol{\eta}^2/2)$. The first-order sideband transitions are the ones where $\boldsymbol{n}$ changes by one in only one dimension, say $\Delta\boldsymbol{n} = (\pm1, 0, 0)$. A transition accompanied by an increase in phonon number is called blue sideband because a higher frequency, $\omega_{12} + \omega_T$, is needed. Its coupling strength is $\Omega_{\boldsymbol{n},\boldsymbol{n}+1} = i\eta_1\sqrt{n_i + 1}\,\Omega_{\boldsymbol{n},\boldsymbol{n}}$. The other one, the red sideband, is resonant to $\omega_{12} - \omega_T$ and has the coupling strength $\Omega_{\boldsymbol{n},\boldsymbol{n}-1} = i\eta_1\sqrt{n_i}\,\Omega_{\boldsymbol{n},\boldsymbol{n}}$.

2.2.3 Rotating-wave approximation

The matrix element of eq. (2.5) takes the form

$$E_{21} = \frac{\hbar\Omega_{\boldsymbol{n},\boldsymbol{n}'}}{2} e^{i\omega_{12}t}\left(e^{i\Delta\boldsymbol{n}\cdot\boldsymbol{\omega}_T t}e^{-i\omega t} + e^{-i\Delta\boldsymbol{n}\cdot\boldsymbol{\omega}_T t}e^{i\omega t}\right) \tag{2.7}$$

where the first term oscillates with the difference frequency,

$$\Delta_{\boldsymbol{n},\boldsymbol{n}'} := \omega - \omega_{12} - \Delta\boldsymbol{n}\cdot\boldsymbol{\omega}_T = \omega - \omega_{\text{atom}},$$

called detuning of the laser from the atomic transition. It is usually in the MHz-regime or lower. The other term oscillates with the sum frequency. On time scales above its inverse, which for optical transitions is in the femtosecond regime, this term averages out and thus is neglected in the so-called «rotating-wave approximation» (RWA). The resulting two-level HAMILTON operator is

$$\hat{H}'_{\mathrm{E1}} = \frac{\hbar}{2}\begin{pmatrix} 0 & \Omega^*_{n,n'} e^{\mathrm{i}\Delta_{n,n'}t} \\ \Omega_{n,n'} e^{-\mathrm{i}\Delta_{n,n'}t} & 0 \end{pmatrix}.$$

The RABI frequency $\Omega_{n,n'}$ is the frequency with which the atom oscillates between the two states $|\psi\rangle$ and $|\psi'\rangle$ in the presence of a resonant field, i. e. for $\Delta_{n,n'} = 0$. For the further calculation it is useful to remove the time dependence. This is achieved by a transformation $\hat{H}_L$ into a reference frame rotating with the detuning of the laser:

$$\hat{H}_L = \frac{\hbar}{2}\begin{pmatrix} -\Delta_{n,n'} & 0 \\ 0 & +\Delta_{n,n'} \end{pmatrix} \qquad \rightarrow \qquad \hat{U}_L = e^{-\frac{\mathrm{i}}{\hbar}\hat{H}_L t} = \begin{pmatrix} e^{\frac{\mathrm{i}}{2}\Delta_{n,n'}t} & 0 \\ 0 & e^{-\frac{\mathrm{i}}{2}\Delta_{n,n'}t} \end{pmatrix}$$

It leads to the HAMILTON operator

$$\hat{H}''_{\mathrm{E1}} = \hat{U}_L^+ \hat{H}'_{\mathrm{E1}} \hat{U}_L - \hat{H}_L = \frac{\hbar}{2}\begin{pmatrix} +\Delta_{n,n'} & \Omega^*_{n,n'} \\ \Omega_{n,n'} & -\Delta_{n,n'} \end{pmatrix}, \tag{2.8}$$

which is used in chapter 4 to model each fundamental transition of the complex dynamics in $^{40}Ca^+$. This reference frame demonstrates the presence of one additional photon in the laser mode with energy $\hbar\omega$ when the atom is in the energetic lower state $|\psi\rangle$. The discrepancy between the total energies of these two states is just given by the detuning $\Delta_{n,n'} = \omega - \omega_{\mathrm{atom}}$.

2.2.4 Higher-order transitions

The same reasoning leads to similar expressions for the higher-order transitions. The vector potential $\boldsymbol{A}$ of eq. (2.6) yields the magnetic field

$$\boldsymbol{B}(\hat{\boldsymbol{R}}, t) = A_0(\boldsymbol{k} \times \boldsymbol{u}) \cos(\boldsymbol{k} \cdot \hat{\boldsymbol{R}} - \omega t)$$

and the electric quadrupole field

$$(\mathrm{grad}\, \boldsymbol{E}(\hat{\boldsymbol{R}}, t))_{ij} = A_0 \omega k_i u_j \sin(\boldsymbol{k} \cdot \hat{\boldsymbol{R}} - \omega t)$$

of the exciting (laser) light.

The same approximations as in the case of an electric dipole transition are valid and lead to the respective RABI frequencies

$$\Omega_{M1} = -\frac{1}{\hbar} |\boldsymbol{\mu}_{12}| A_0 |\boldsymbol{k}| = \frac{g_J \mu_B}{\hbar} A_0 k$$

for a magnetic dipole transition and

$$\Omega_{E2} = -\frac{1}{6\hbar} \left|\hat{Q}\right| A_0 \omega |\boldsymbol{k}| = -\frac{q_{red}\langle r^2\rangle}{2\hbar} A_0 \omega k$$

for an electric quadrupole transition. The first depends on the BOHR magneton $\mu_B = e\hbar/(2m_e)$ and the LANDÉ factor g_J, the second depends on the reduced electric charge q_{red} introduced on p. 27. The different directional dependence for all three kinds of transitions are discussed in the next section. In comparison to the electric dipole transition with $\Omega_{E1} = -q\langle r\rangle A_0 \omega/\hbar$ the coupling strength of the quadrupole has an extra factor proportional to the ratio of the expansion of the electronic wave function to the wavelength of the exciting light ($\sim r/\lambda$). This makes such transitions weaker by several orders of magnitude. The magnetic dipole is similarly weak due to the relative factor $\hbar/(cm_e\langle r\rangle)$ and the much lower transition frequency.

2.3 Geometrical considerations

Since the electromagnetic field has vectorial character its polarisation implies a directional dependence of the driven transitions. This leads to geometrical weighting factors to the above-mentioned RABI frequencies that depend on the polarisation direction of the exciting light.
As the quantisation axis is defined by the static magnetic field that couples to the total magnetic moment, the ZEEMAN splitting of the fine-structure states leads to the anomalous ZEEMAN effect. Thus, for the electric transitions, which couple only to the degree of freedom of the orbital angular momentum, the combination of spin and orbital angular momentum becomes important. This leads to a complex dependency between the coupling strengths and the direction of polarisation of the exciting light, and the CLEBSCH–GORDAN coefficients have to be taken into account as further factors to the RABI frequencies. This section goes into the geometrical details to find both factors for all considered transitions.

2.3.1 Addition of angular momenta

As mentioned in section 2.1 the energy eigenstates $|n, L, J, m_J\rangle$ of the unperturbed system are also eigenstates of the total angular momentum to which the magnetic

multipoles couple directly. As the electric multipoles couple only to the orbital angular momentum of charged particles and keep the spin state untouched, the eigenstates of the uncoupled momenta $\hat{\boldsymbol{L}}_e$ and $\hat{\boldsymbol{S}}$ have to be taken into account. These are $|n, l, m\rangle$ and $|S, m_S\rangle$, respectively. Their connection to the eigenstates of the total angular momentum are given by linear combination that follows from the calculus of the addition of angular-momentum operators. The coefficients of these linear combinations are complex numbers called Clebsch–Gordan coefficients c_{CG}:

$$|n, L, J, m_J\rangle = \sum_{m_S=-S}^{+S} c_{CG}(L, m, S, m_S, J)|n, l, m\rangle \otimes |S, m_S\rangle$$

Herein $m_J = m + m_S$ and $|L - S| \leq J \leq L + S$ must both be fulfilled to satisfy the conservation of angular momentum. The tables of the Clebsch–Gordan coefficients for all combinations of two angular momenta with the quantum numbers ½, 1, ³⁄₂, and 2 are found in [83, p. 368].

To calculate the matrix element of an electric multipole moment for the transition between two certain states, the coupling between all products of $|n, l, m\rangle$ and $|S, m_S\rangle$ in the respective two linear combinations have to be taken into account. Fortunately, this is given by the same formalism applied to the addition of the lower state's with the photon's total angular momentum (with indices 1 and ϕ) to yield the angular momentum of the upper state (with the index 2), i. e.

$$\left|n_2, L_2, J_2, m_{J_2}\right\rangle = \sum_{m_\phi=-J_\phi}^{+J_\phi} c_{CG}(J_1, m_1, J_\phi, m_\phi, J_2)\left|n_1, L_1, J_1, m_{J_1}\right\rangle \otimes \left|J_\phi, m_\phi\right\rangle.$$

This is owed to another case of the law of conservation of angular momentum, which applies to both particles together—the atom and the single photon that is emitted or absorbed at this transition. The resulting values of the Clebsch–Gordan coefficients for the seven relevant transitions in $^{40}Ca^+$ are specified in the appendix, see section A 3 on p. 117. The principal quantum number n does not affect the angular dependence: In spherical coordinates the position representation of the spatial part of the atomic wave function shows the separation of the angular dependence into spherical harmonics Y_{lm} from the radial dependence into R_{nl},

$$\langle \boldsymbol{r}|n, l, m\rangle = \psi_{nlm}(\boldsymbol{r}) = R_{nl}(r)Y_{lm}(\theta, \phi).$$

Furthermore, the selection rules for the electric multipole transitions follow directly from the properties of the spherical harmonics $Y_{lm}(\theta, \phi) = \langle \theta, \phi|l, m\rangle$, precisely

through the formulae,

$$\cos\hat{\theta}|l,m\rangle = \sqrt{\frac{(l+1+m)(l+1-m)}{(2l+1)(2l+3)}}\,|l+1,m\rangle + \sqrt{\frac{(l+m)(l-m)}{(2l-1)(2l+1)}}\,|l-1,m\rangle, \tag{2.9}$$

$$e^{\pm i\hat{\phi}}\sin\hat{\theta}|l,m\rangle = \mp\sqrt{\frac{(l\pm m+2)(l\pm m+1)}{(2l+1)(2l+3)}}\,|l+1,m\pm1\rangle \pm \sqrt{\frac{(l\mp m)(l\mp m-1)}{(2l-1)(2l+1)}}\,|l-1,m\pm1\rangle. \tag{2.10}$$

This is carried out in section 2.3.3 and 2.3.4.

2.3.2 The laboratory coordinate system

For a general description of the laser-beam geometry, the laboratory coordinate system is defined in the following way: The plane of the laboratory table is given by the two CARTESian coordinates x and z, the latter being the direction of the static magnetic field $\boldsymbol{B}_0$. The third coordinate y points upwards out of the laboratory table, see figure 2.1.

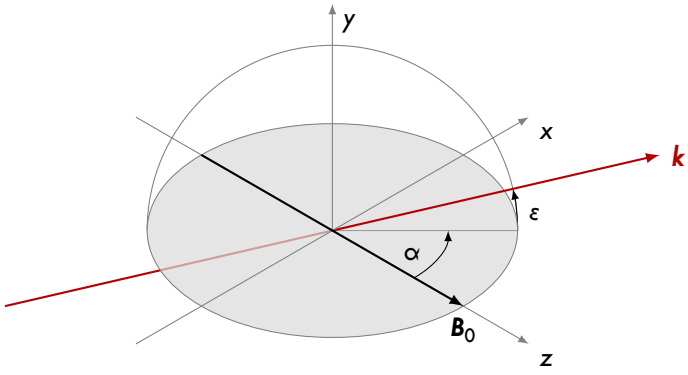

Figure 2.1 – Geometry of the laboratory coordinate system (see text).

The direction of a laser beam is set by two angles, the azimuth α indicating the rotation in the plane of the laboratory table out of the z-direction and the elevation ε above this plane, which in most of the practical cases is equal to zero. This leads to the wave vector

$$\boldsymbol{k} = \frac{2\pi}{\lambda}\begin{pmatrix}\cos\varepsilon\sin\alpha\\ \sin\varepsilon\\ \cos\varepsilon\cos\alpha\end{pmatrix}. \tag{2.11}$$

To cover the full surface of the sphere, the allowed intervals are $\alpha \in [0;2\pi]$ and $\varepsilon \in [-\pi/2;\pi/2]$. In contrast to the standard spherical coordinates (see sec. 1.1 on p. 7), the

volume element in this case is $dV = r^2 \cos\varepsilon \, dr \, d\alpha \, d\varepsilon$. The polarisation component in the x-z-plane of the laboratory table is called horizontal (H); the other one perpendicular to H is called vertical (V). As both are of course perpendicular to the wave vector, their unit vectors are

$$\mathbf{e}_H = \begin{pmatrix} \cos\alpha \\ 0 \\ -\sin\alpha \end{pmatrix} \qquad \text{and} \qquad \mathbf{e}_V = \begin{pmatrix} -\sin\varepsilon\sin\alpha \\ \cos\varepsilon \\ -\sin\varepsilon\cos\alpha \end{pmatrix}.$$

Thus, the laser's electric-field vector, given in eq. (1.4) on p. 10, transforms accordingly to $\boldsymbol{E} = |\boldsymbol{E}|\,\boldsymbol{u}$ with the unit vector $\boldsymbol{u} = (\mathbf{e}_H\langle H| + \mathbf{e}_V\langle V|)\,|\theta, \phi\rangle$ into the laboratory system:

$$\boldsymbol{u} = \frac{1}{\sqrt{2}} \begin{pmatrix} (\cos\alpha - i\sin\varepsilon\sin\alpha)e^{-i\frac{\phi}{2}}\cos\frac{\theta}{2} + (\cos\alpha + i\sin\varepsilon\sin\alpha)e^{i\frac{\phi}{2}}\sin\frac{\theta}{2} \\ i\cos\varepsilon\left(e^{-i\frac{\phi}{2}}\cos\frac{\theta}{2} - e^{i\frac{\phi}{2}}\sin\frac{\theta}{2}\right) \\ -(\sin\alpha + i\sin\varepsilon\cos\alpha)e^{-i\frac{\phi}{2}}\cos\frac{\theta}{2} - (\sin\alpha - i\sin\varepsilon\cos\alpha)e^{i\frac{\phi}{2}}\sin\frac{\theta}{2} \end{pmatrix} \tag{2.12}$$

Therein, the two angles θ and ϕ define the general polarisation state, eq. (1.3).

2.3.3 Electric dipole transitions

The representation of the electric dipole moment in spherical coordinates is

$$\hat{\boldsymbol{d}} = q\hat{\boldsymbol{r}} = q\hat{r}\begin{pmatrix} \cos\hat{\phi}\sin\hat{\theta} \\ \sin\hat{\phi}\sin\hat{\theta} \\ \cos\hat{\theta} \end{pmatrix} = q\hat{r}\begin{pmatrix} \frac{1}{2}(e^{+i\hat{\phi}} + e^{-i\hat{\phi}})\sin\hat{\theta} \\ \frac{1}{2i}(e^{+i\hat{\phi}} - e^{-i\hat{\phi}})\sin\hat{\theta} \\ \cos\hat{\theta} \end{pmatrix},$$

and in combination with eq. (2.9) and (2.10) this leads directly to the selection rules for electric dipoles as $\Delta l = \pm 1$ and $\Delta m \in \{-1, 0, +1\}$, and to the directions of the dipole moments, $\mathbf{e}_z$ for $\Delta m = 0$ and $\mathbf{e}_x \mp i\mathbf{e}_y$ for $\Delta m = \pm 1$. The electric dipole interaction $\hat{H}_{E1}$ connects this with the direction of polarisation. Thus, the z-component of the polarisation, i. e. the one parallel to the quantisation axis, drives the transitions with $\Delta m = 0$, which therefore are called π-transitions; while the other two components drive both of the two transitions with $\Delta m = \pm 1$, and are thus called $\sigma^{\pm}$-transitions.[1] The coupling strength of the electric dipole between two states results to be

$$\langle\psi'|\hat{H}_{E1}|\psi\rangle = -\langle n', l', m'|\hat{\boldsymbol{d}}|n, l, m\rangle \cdot \langle \boldsymbol{n}'|\boldsymbol{E}(\hat{\boldsymbol{R}}, t)|\boldsymbol{n}\rangle = \frac{\hbar\Omega_{E1}}{2} g_{|\Delta l|,\Delta m},$$

1) The π stands for german «**p**arallel», and σ for «**s**enkrecht» (i. e. perpendicular).

where $l' = l + \Delta l$ and $m' = m + \Delta m$, and a geometrical weighting factor $g_{|\Delta l|,\Delta m}$ appears that depends on the four angles α, ε, θ, and ϕ of the laser beam. These factors are

$$g_{1,0} = \frac{u_z}{|\boldsymbol{u}|}\left(\sqrt{\frac{(l+1+m)(l+1-m)}{(2l+1)(2l+3)}}\,\delta_{l',l+1} + \sqrt{\frac{(l+m)(l-m)}{(2l-1)(2l+1)}}\,\delta_{l',l-1}\right),$$

$$g_{1,\pm1} = \frac{u_x \mp i u_y}{2\,|\boldsymbol{u}|}\left(\mp\sqrt{\frac{(l\pm m+2)(l\pm m+1)}{(2l+1)(2l+3)}}\,\delta_{l',l+1} \pm \sqrt{\frac{(l\mp m)(l\mp m-1)}{(2l-1)(2l+1)}}\,\delta_{l',l-1}\right)$$

for π- and σ-transitions, respectively. Inserting eq. (2.12) leads to the formulae used in the Matlab programme of chapter 4.

The other way around, these factors are the partial directive gain (or emission probability amplitude) of the atom as a single-photon emitter if it does a quantum jump on the corresponding transition. To find the directional characteristics (or directivity) for the light emitted at these transitions one has to integrate over all possible polarisation states weighted by the geometrical factors $g_{|\Delta l|,\Delta m}$,

$$\left|\mathrm{Pol}_{|\Delta l|,\Delta m}(\alpha,\varepsilon)\right\rangle = \frac{1}{2\pi}\iint g^*_{|\Delta l|,\Delta m}|\theta,\phi\rangle \sin\theta\,\mathrm{d}\theta\,\mathrm{d}\phi\,.$$

This is visualised in figure 2.2 for the three possible cases of Δm. If the emitted light of these three cases is added incoherently, the result will be a spherical wave of non-polarised light.

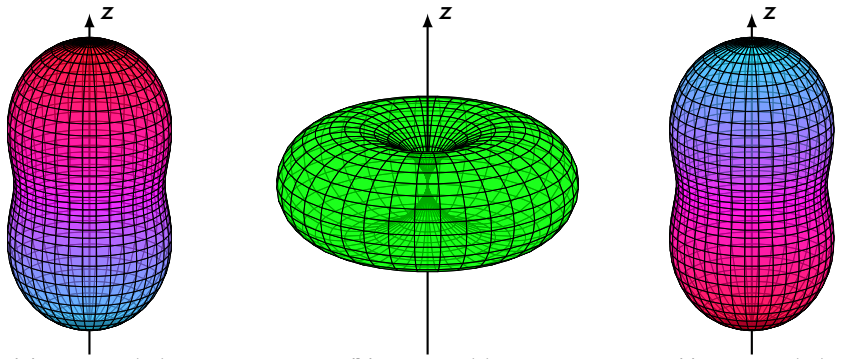

Figure 2.2 – Directional characteristics of the electric dipole emission. The radius indicates the directional dependence of the intensity (i. e. the directivity) while the colours encode the polarisation of the radiation. Red and cyan indicate the right- and left-circular polarisation, respectively; green and magenta the linear polarisation parallel and perpendicular to the plane spanned by the wave vector $\boldsymbol{k}$ and the quantisation axis $\mathbf{e}_z$.

2.3.4 Electric quadrupole transitions

The electric quadrupole moment in spherical coordinates reads as follows:

$$\hat{Q} = q_{\text{red}}\hat{r}^2 \begin{pmatrix} 3\cos^2\hat{\phi}\sin^2\hat{\theta} - \mathbb{1} & 3\cos\hat{\phi}\sin\hat{\phi}\sin^2\hat{\theta} & 3\cos\hat{\phi}\sin\hat{\theta}\cos\hat{\theta} \\ 3\cos\hat{\phi}\sin\hat{\phi}\sin^2\hat{\theta} & 3\sin^2\hat{\phi}\sin^2\hat{\theta} - \mathbb{1} & 3\sin\hat{\phi}\sin\hat{\theta}\cos\hat{\theta} \\ 3\cos\hat{\phi}\sin\hat{\theta}\cos\hat{\theta} & 3\sin\hat{\phi}\sin\hat{\theta}\cos\hat{\theta} & 3\cos^2\hat{\theta} - \mathbb{1} \end{pmatrix}.$$

Again using eq. (2.9) and (2.10) the selection rules for electric quadrupoles result in $\Delta l = 0 = \Delta m$, or $\Delta l = \pm 2$ and $\Delta m \in \{0, \pm 1, \pm 2\}$. The discussion is restricted to the cases of $|\Delta l| = 2$ as these alone are of interest in $^{40}Ca^+$ because they correspond to the quadrupole transitions at 729 nm and 732 nm wavelength. The interaction term, $\hat{H}_{E2} = -\frac{1}{6}\,\mathrm{tr}(\hat{Q}\cdot \mathrm{grad}\,\boldsymbol{E}(\hat{\boldsymbol{R}}, t))$, leads to the quadrupole-moment matrix elements,

$$\langle\psi'|\hat{H}_{E2}|\psi\rangle = -\frac{1}{6}\langle n', l', m'|\hat{Q}_{ij}|n, l, m\rangle\langle \boldsymbol{n}'|k_j E_i(\hat{\boldsymbol{R}}, t)|\boldsymbol{n}\rangle = \frac{\hbar\Omega_{E2}}{2} g_{|\Delta l|,\Delta m},$$

with the introduction of the RABI frequency Ω_{E2} for electric quadrupole transitions and again geometrical weighting factors. For $|\Delta l| = 2$ these are,

$$g_{2,0} = -\frac{3}{2}\frac{k_x u_x + k_y u_y - 2k_z u_z}{|\boldsymbol{k}||\boldsymbol{u}|}\left(\sqrt{\frac{(l-m+1)(l+m+1)(l-m+2)(l+m+2)}{(2l+1)(2l+3)^2(2l+5)}}\,\delta_{l',l+2} + \sqrt{\frac{(l-m-1)(l+m-1)(l-m)(l+m)}{(2l-3)(2l-1)^2(2l+1)}}\,\delta_{l',l-2}\right),$$

$$g_{2,\pm1} = \mp\frac{3}{2}\frac{k_z(u_x \mp i u_y) + (k_x \mp i k_y)u_z}{|\boldsymbol{k}||\boldsymbol{u}|}\left(\sqrt{\frac{(l-m+1)(l+m+1)(l\pm m+2)(l\pm m+3)}{(2l+1)(2l+3)^2(2l+5)}}\,\delta_{l',l+2} - \sqrt{\frac{(l-m)(l+m)(l\mp m-1)(l\mp m-2)}{(2l-3)(2l-1)^2(2l+1)}}\,\delta_{l',l-2}\right),$$

$$g_{2,\pm2} = \frac{3}{4}\frac{k_x u_x \mp i(k_x u_y + k_y u_x) - k_y u_y}{|\boldsymbol{k}||\boldsymbol{u}|}\left(\sqrt{\frac{(l\mp m+1)(l\mp m+2)(l\pm m+3)(l\pm m+4)}{(2l+1)(2l+3)^2(2l+5)}}\,\delta_{l',l+2} + \sqrt{\frac{(l\mp m-3)(l\mp m-2)(l\pm m-1)(l\pm m)}{(2l-3)(2l-1)^2(2l+1)}}\,\delta_{l',l-2}\right).$$

Here, eq. (2.11) and (2.12) are used to find the angular dependence.
The directivity for the cases of different Δm is shown in figure 2.3. And as above, if the emitted light of these five cases is added incoherently, the result will be a non-polarised spherical wave.

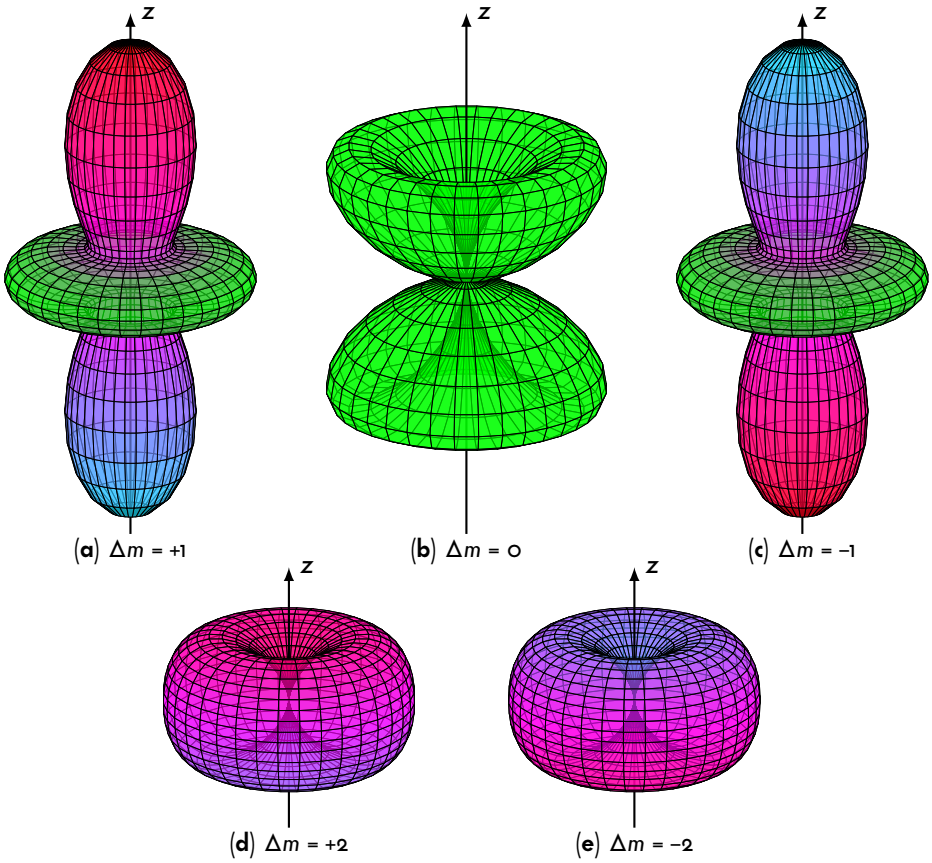

Figure 2.3 – Directional characteristics of the electric quadrupole emission for $\Delta l = \pm 2$. The radius indicates the directional dependence of the intensity (i. e. the directivity) while the colours encode the polarisation of the radiation as in figure 2.2.

2.3.5 Magnetic dipole transitions

Finally, the simple case of the magnetic dipole interaction $\hat{H}_{M1}$ is discussed. Again, the multipole-moment operator, here

$$\hat{\boldsymbol{\mu}}_J = \frac{-e}{2m_e} g_J \hat{\boldsymbol{J}} = -g_J \frac{\mu_B}{\hbar} \begin{pmatrix} \frac{1}{2}(\hat{J}_+ + \hat{J}_-) \\ \frac{1}{2i}(\hat{J}_+ - \hat{J}_-) \\ \hat{J}_z \end{pmatrix}$$

with the ladder operators $\hat{J}_\pm$, exhibits the selection rules, $\Delta J = 0$ and $\Delta m_J = \pm 1$. In addition it shows that the driven transitions are between eigenstates of spin–orbit

coupling directly, so the Clebsch–Gordan coefficients do not come into play here. The only degree of freedom that changes is the magnetic quantum number m_J. Looking at the interaction term

$$\hat{H}_{M1} = -\hat{\boldsymbol{\mu}}_J \cdot \boldsymbol{B}_{dyn}(\hat{\boldsymbol{R}}, t) = g_J \frac{\mu_B}{\hbar} \hat{\boldsymbol{J}} \cdot (\boldsymbol{k} \times \boldsymbol{u}) A_0 \cos(\boldsymbol{k} \cdot \hat{\boldsymbol{R}} - \omega t)$$

shows furthermore that only the one component of the total angular momentum $\hat{\boldsymbol{J}}$, which is perpendicular to the wave vector $\boldsymbol{k}$ and to the polarisation direction $\boldsymbol{u}$, governs this interaction. As the atom stays in its Zeeman manifold under this interaction the light to drive it has to be radio waves instead of visible or near-infrared light. The coil underneath the ion trap (see section 1.4.5 and figure 2.4) produces a magnetic field $\boldsymbol{B}_{dyn}$ in y-direction that oscillates with about 8 MHz to drive the magnetic dipole transition between the $S_{1/2}$ Zeeman sub-levels.

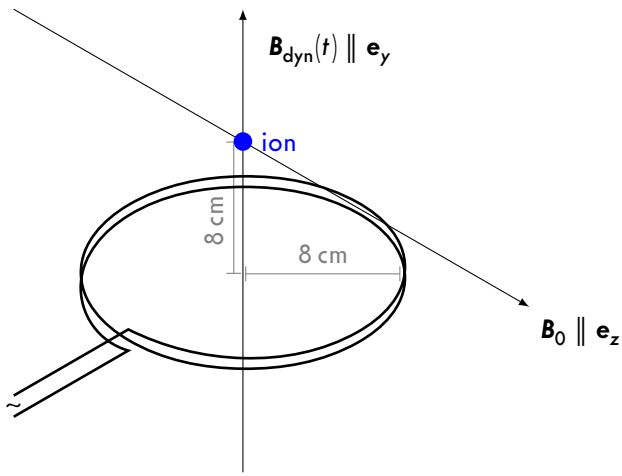

Figure 2.4 – Geometry of the radio-frequency coil that drives the magnetic dipole transition. The alternating electric current applied to the coil beneath the ion trap produces an oscillating magnetic field $\boldsymbol{B}_{dyn}(t)$ perpendicular to the quantisation axis given by the static field $\boldsymbol{B}_0$.

The geometrical weighting factors are,

$$g_{|\Delta J|, \Delta m_J} = \frac{(k_y \mp \mathrm{i} k_x) u_z \pm \mathrm{i} k_z (u_x \pm \mathrm{i} u_y)}{2 |\boldsymbol{k}|} \sqrt{(J \mp m_J)(J \pm m_J + 1)},$$

and lead to the directivity shown in figure 2.5.

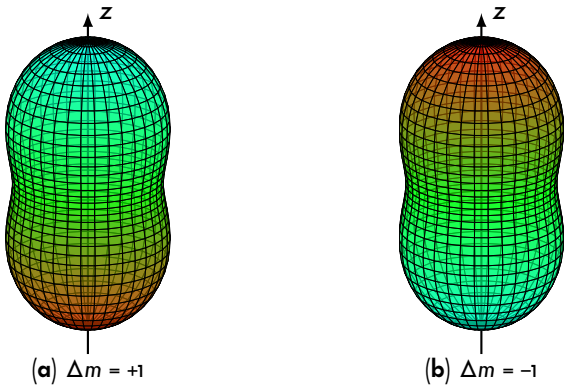

Figure 2.5 – Directional characteristics of the magnetic dipole emission. The radius indicates the directional dependence of the intensity (i. e. the directivity) while the colours encode the polarisation of the radiation as in figure 2.2.

In opposition to the two electric transitions mentioned above, the magnetic dipole does not support a spherical wave as it is aligned with the axis of the external magnetic field.

Chapter 3

Modelling the spontaneous RAMAN scattering

«Die ganzen 50 Jahre bewusster Grübelei haben mich
der Antwort der Frage „Was sind Lichtquanten"
nicht näher gebracht. Heute glaubt zwar jeder Lump,
er wisse es, aber er täuscht sich.»

— A. EINSTEIN (1951)[29]

The spirit that hovered over the whole thesis is the question:

«How does a photon emitted by an atom really looks like?»

One of the abiding and heated debates in quantum optics over the last few decades is about the nature of RAMAN-scattered light, especially at the single-photon level. The addressed issues are the purity and coherence of the scattered light and the question if these single photons actually reach the FOURIER limit. Another question rises from the impression that an excitation far below saturation generates RAMAN-scattered photons with a bandwidth arbitrarily narrower than the natural linewidth of the atomic emitter, and how this is compatible to the property of an atom to act as a filter for broadband light.
Answering these questions led to an extended investigation over several years. Its results are summarises in this chapter and confirm previously existing intuitions. After a brief introduction to RAMAN scattering, a model based on resolvent theory (sec. 3.1) and in particular its results and predictions are presented in detail. This is followed by another model, based on the LINDBLAD equation (sec. 3.5). Finally the

RAMAN operator is derived (sec. 3.6), a concise tool that comprehends the essence of this scattering process, and which is used in chapter 5 for further calculations.

The elastic or **RAYLEIGH scattering** of photons at a single atom or molecule, where the initial and final state of the scattering centre are the same, is well described in the picture of a two-level system. The inelastic or RAMAN scattering on the other hand is more complex due to the needed third level where the process ends, and thus poorly described in the literature. The best references so far [54, 135, 136] concern only partial aspects of the elemental process. Especially the excitation by a single photon, which is very important in the context of quantum networks, is absent in the literature.

RAMAN scattering is the simultaneous absorption and emission of a photon by a single atom or molecule in which the scattering centre ends in a state different from where it started. This effect was predicted by Adolf SMEKAL in 1923 [117], and measured for the first time by Chandrasekhara V. RAMAN and Kariamanickam S. KRISHNAN in 1928 [99]. In the youth of this field of research the processes between different vibrational and rotational states of molecules were investigated which opened up the wide field of RAMAN spectroscopy [125]. It is used to identify molecules and to study their chemical bonding as well as to characterise material properties of e. g. semiconductors. These techniques have application in chemistry, archaeology, forensic analysis, art history, and medical sciences. Decades later, processes between internal states of single atoms were examined, as it is the case in this thesis. Today, surface-enhanced RAMAN spectroscopy (SERS) reaches an enhancement factor of up to 10^{11} above the free-space variant, which makes even single-molecule imaging possible [65].

If the final state of the emitter is energetically higher than the initial one, the process is called STOKES–RAMAN scattering. The opposite is hence called anti-STOKES–RAMAN scattering. In the case of only one present light field (with a carrier frequency close to the resonance of the absorption transition) the scattering is called spontaneous as a single photon is emitted spontaneously into the vacuum field. This is the case of interest in this thesis. The other case is called stimulated RAMAN scattering at which a second light field is present, resonant or near-resonant to the emission transition. This non-linear optical effect is exploited in so-called RAMAN amplifiers and RAMAN lasers [27, 106].

A quantum-mechanical treatment of the process needs to include at least three atomic states, the initial and the final state as well as an excited state that is populated, at least virtually, during the scattering process. The corresponding level scheme for the spontaneous RAMAN scattering is sketched in figure 3.1. It introduces the detuning Δ of the excitation light field with carrier frequency ω

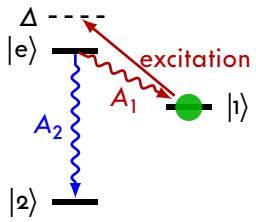

Figure 3.1 – The level scheme of a spontaneous RAMAN transition. Excitation from the initial state $|1\rangle$ to the intermediate, excited state $|e\rangle$, detuned by Δ, results in a decay into the final state $|2\rangle$. The branching ratio of spontaneous decay is given by the EINSTEIN A-coefficients, A_1 and A_2.

from the atomic absorption transition with frequency ω_A, i. e. $\Delta := \omega - \omega_A$.
In the preceding work of the research group, a model of rate equations was investigated, see Michael SCHUG's thesis [112, p. 26–32]. It yields the same transition rates as the detailed models below, but does neither explain any dynamical effects such as RABI oscillation, nor does it provide detailed spectral information.

3.1 General model based on resolvent theory

To gain a deeper understanding of the spectral properties of spontaneously RAMAN-scattered photons, and their dependency on the spectrum of the exciting light a theoretical study was undertaken, starting with the master thesis of Tristan TENTRUP [121]. That work has been comprehensively revised, extended, and finalised by the author of this thesis, and led to the article:

> P. MÜLLER, T. TENTRUP, M. BIENERT, G. MORIGI & J. ESCHNER «Spectral properties of single photons from quantum emitters» in *Phys. Rev. A* **96** (2017), 23861. DOI: 10.1103/PhysRevA.96.023861, i. e. [82]

The whole study is based on the resolvent theory using the projection method and the residue theorem as presented in the textbook [19], and applies the WEISSKOPF–WIGNER approximation [127].

3.1.1 Resolvent theory

In a first approach, the initial state of the system is

$$|i\rangle = |1\rangle \otimes |1_{\omega_1}\rangle,$$

where the atom is in the state $|1\rangle$ and a single monochromatic photon with the frequency ω_1 is present. To calculate the amplitude spectrum of the emitted photon, the time evolution of this state is regarded. The probability amplitude to end in the final state

$$|f\rangle = |2\rangle \otimes \left|1_{\omega_2}\right\rangle,$$

where the atom changed into the state $|2\rangle$ by emission of a single photon whose spectrum is afterwards projected to the monochromatic frequency ω_2, is already the wanted amplitude spectrum. It is:

$$U_{fi}(t, \omega_2, \omega_1) = \langle f|\hat{U}(t)|i\rangle$$

with the time-evolution operator

$$\hat{U}(t) = \mathrm{e}^{-\frac{\mathrm{i}}{\hbar}\hat{H}t}$$

for a system driven by a time-independent HAMILTON operator $\hat{H}$ for a duration t.
In the second step, the same is calculated for a generic incident photon with an arbitrary amplitude spectrum ψ_1, hence

$$|i\rangle = |1\rangle \otimes \int_0^\infty \psi_1(\omega)|1_\omega\rangle \,\mathrm{d}\omega\,.$$

This leads to the spectrum[1]

$$\psi_2(t, \omega_2) = \int_{-\infty}^{\infty} \psi_1(\omega) U_{fi}(t, \omega_2, \omega)\,\mathrm{d}\omega \qquad (3.1)$$

for the emitted photon. As a function of the observation interval t it exhibits the temporal evolution of the spectrum during the emission process. In the following all calculations are restricted to the limit $t \to \infty$, which means only the spectrum in the asymptote of the completed emission process is considered, $\psi_2(t \to \infty, \omega_2)$. A positive side effect is that this result is far more simpler and cleaner than the general one, and it matches the intuition.

1) For calculational simplification the integration interval is henceforth extended to negative infinity under the assumption that the spectral function $\psi_1(\omega)$ has a negligible contribution for $\omega < 0$, which is the case for linewidths $\Delta\omega \ll \omega$.

To handle $U_{fi}(t, \omega_2, \omega)$ the resolvent theory is used: Following [19, p. 170 f.], the time-evolution operator is rewritten as a complex integral,

$$\hat{U}(t) = \frac{1}{2\pi i} \int_{C_+} \underbrace{\frac{1}{z\mathbb{1} - \hat{H}}}_{=:\hat{G}(z)} e^{-\frac{i}{\hbar} z t} \, dz, \tag{3.2}$$

over the complex variable, $z = \hbar\omega + i\eta$, where the integration path C_+ is the real axis in negative direction, but slightly shifted upward the imaginary axis by a constant η to avoid division by zero, see figure 3.2. After integration this constant is turned to zero again ($\eta \to 0^+$). The path is extended over the lower half-plane to apply the residue theorem, thus solving the integral with ease.

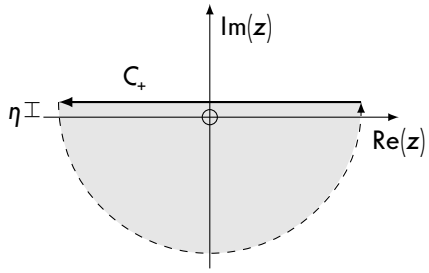

Figure 3.2 – The integration path C_+ of eq. (3.2) in the complex plane (solid arrow). It is extended by a semi-circle with the radius $r \to \infty$ (dashed arrow) to close the integration path for the application of the residue theorem.

The fraction in the integrand of eq. (3.2) is called the resolvent $\hat{G}(z)$ of the Hamilton operator $\hat{H}$. To find the amplitude spectrum, $G_{fi}(z) := \langle f|\hat{G}(z)|i\rangle$ is solved through the so-called projection method.

3.1.2 Projection method

Following [19, p. 174–179], the action of an operator on the excited state is separated from the other states by expressing the unity operator as the sum over the projector onto the excited state, $\hat{P} = |e\rangle\langle e|$, and its complement, $\hat{Q} = \mathbb{1} - \hat{P}$. Hence, $G_{fi}(z) = \langle f|\hat{G}(z)|i\rangle = \langle f|\hat{Q}\hat{G}(z)\hat{Q}|i\rangle$. Considering the interaction $\hat{V}$ between atom and light field as a perturbation, it has been shown that

$$\hat{Q}\hat{G}(z)\hat{Q} = \frac{\hat{Q}}{z\mathbb{1} - \hat{Q}\hat{H}_0\hat{Q} - \hat{Q}\hat{V}\hat{Q}} \cdot \left(\mathbb{1} + \hat{V} \frac{\hat{P}}{z\mathbb{1} - \hat{P}\hat{H}_0\hat{P} - \hat{P}\hat{R}(z)\hat{P}} \hat{V} \frac{\hat{Q}}{z\mathbb{1} - \hat{Q}\hat{H}_0\hat{Q} - \hat{Q}\hat{V}\hat{Q}} \right)$$

with the so-called level-shift operator,

$$\hat{R}(z) = \hat{V} + \hat{V}\frac{\hat{Q}}{z\mathbb{1} - \hat{Q}\hat{H}_0\hat{Q} - \hat{Q}\hat{V}\hat{Q}}\hat{V} + \mathcal{O}(\hat{V}^3).$$

In the following, this is expressed in the unperturbed eigenstates $|1\rangle$, $|e\rangle$, and $|2\rangle$, with the eigenenergies E_1, E_e, and E_2, respectively. As the interaction term governs only transitions, the diagonal terms $\hat{Q}\hat{V}\hat{Q}$ and $\langle e|\hat{V}|e\rangle$ vanish, and the remaining off-diagonals, $\langle e|\hat{V}|1\rangle =: V_{e1}$ and $\langle e|\hat{V}|2\rangle =: V_{e2}$, are the coupling strengths of these transitions.

The only remaining matrix element of $\hat{R}(z)$ is evaluated using the Cauchy principal value $\mathcal{P}$ [44, p. 69 f.],

$$\begin{aligned}\langle e|\hat{R}(z)|e\rangle &= 0 + \sum_q V_{eq}\frac{1}{z - E_q - 0}V_{qe} + \mathcal{O}(\hat{V}^3)\\ &\approx \underbrace{\sum_q V_{eq}V_{qe}\mathcal{P}\left(\frac{1}{z - E_q}\right)}_{=:\hbar\Delta} - \frac{i}{2}\underbrace{2\pi\sum_q V_{eq}V_{qe}\delta(z - E_q)}_{=:\hbar\Gamma},\end{aligned}$$

introducing the line shift Δ and the line width Γ. Hence, the resolvent takes the form

$$G_{fi}(z) = \frac{1}{z - E_f}V_{fe}\frac{1}{z - E_e - \hbar\Delta + i\hbar\frac{\Gamma}{2}}V_{ei}\frac{1}{z - E_i}.$$

In general, it is a product of one fraction for each participating state (here 3 terms), and the coupling strengths of each participating transition (here 2 terms).

Inserting this into the time-evolution operator, eq. (3.2), leads to a complex integral with three poles of first order each, that is easily solvable by the residue theorem. Thus, $U_{fi}(t, \omega_2, \omega)$ results to be a sum over three terms corresponding to the three participating states in this process. In the limit $t \to \infty$ only one of these summands remains, and inserting it into eq. (3.1) yields the emission amplitude spectrum to be

$$\psi_2(\omega_2) = \sqrt{\frac{2\pi A_1 A_2}{\Gamma}}\,\psi_1(\omega_2 - (\omega_E - \omega_A)) \cdot L_\Gamma(\omega_2 - \omega_E) \tag{3.3}$$

with the centre frequency ω_1 of the incident spectrum. That is the product of the incident photon's spectrum ψ_1 (just shifted by the difference in the transition frequencies, $\omega_E - \omega_A$) and the atomic Lorentzian of the emission transition,

$$L_\Gamma(\omega - \omega_E) = \frac{\sqrt{\frac{\Gamma}{2\pi}}}{\omega - \omega_E + i\frac{\Gamma}{2}},$$

with the full atomic linewidth $\Gamma = A_1 + A_2$. The pre-factor in eq. (3.3) reveals the influence of the branching fractions onto the probability that the scattering actually occurs. This success probability is given by the integral over the squared modulus,

$$P_{\text{scatter}} = \int_{-\infty}^{\infty} |\psi_2(\omega_2)|^2 \, \mathrm{d}\omega_2,$$

and thus, the normalised power spectrum is

$$S(\omega_2) = \frac{1}{P_{\text{scatter}}} |\psi_2(\omega_2)|^2 .$$

In the article [82] this is investigated in detail for three different cases of incoming light: rectangular, exponential, and GAUSSian wave packets (or sinc, LORENTZian, and GAUSSian spectra, respectively).

3.1.3 Results for an exponential photon

The most important case for experimental situations are single photons used for excitation that are approximately exponential in their wave form. Thus, their spectrum is a LORENTZian line of a certain width $\Delta\omega_1$ centred at the carrier frequency ω_1 of the wave,

$$\psi_1(\omega) = L_{\Delta\omega_1}(\omega - \omega_1) = \frac{\sqrt{\frac{\Delta\omega_1}{2\pi}}}{\omega - \omega_1 + \mathrm{i}\frac{\Delta\omega_1}{2}}.$$

The resulting amplitude spectrum of the emitted photon, eq. (3.3), is a product of two complex LORENTZian curves. Through partial fraction decomposition, it is rewritten as a sum,

$$L_{\Delta\omega_1}(\Delta_2 - \Delta_1) \cdot L_\Gamma(\Delta_2) = \frac{\sqrt{\Gamma\Delta\omega_1}}{\Delta_1 + \mathrm{i}\frac{\Gamma - \Delta\omega_1}{2}} \left(\frac{1}{\sqrt{\Delta\omega_1}} L_{\Delta\omega_1}(\Delta_2 - \Delta_1) - \frac{1}{\sqrt{\Gamma}} L_\Gamma(\Delta_2) \right), \qquad (3.4)$$

expressed in the detunings, $\Delta_1 = \omega_1 - \omega_A$ and $\Delta_2 = \omega_2 - \omega_E$. This decomposition is invalid only if the two LORENTZian lines are exactly the same (i. e. if both, $\Delta\omega_1 = \Gamma$ and $\Delta_1 = 0$). It shows that the emitted photon is a superposition of two LORENTZian spectral states weighted by the reciprocal square roots of their respective widths. The first part of eq. (3.4) corresponds to the RAMAN peak with detuning and linewidth equal to the excitation detuning and linewidth. The other part is

emitted at resonance with the linewidth of the natural decay, and thus called spontaneous peak. In the usual case of narrowband photons ($\Delta\omega_1 \ll \Gamma$) the RAMAN peak is dominant and just as narrow. In the other extremum only the spontaneous part remains—matching the intuition that then the atom acts as a filter. If the excitation occurs close to resonance ($\Delta_1 \approx 0$) the two peaks merge to a single one.
The success probability for this RAMAN process is,

$$P_{\text{scatter}} = \frac{A_1 A_2}{\Gamma} \frac{\Gamma + \Delta\omega_1}{\Delta_1^2 + \left(\frac{\Gamma+\Delta\omega_1}{2}\right)^2} \leq 1,$$

which reaches unity only in the marginal case of resonant excitation ($\Delta_1 = 0$) by a purely monochromatic photon ($\Delta\omega_1 \to 0$), and additionally with equal branching fractions ($A_1 = A_2 = \Gamma/2$).

3.2 Excitation by laser

If the exciting light source is not a single photon, but many, e. g. a laser beam, several excitations and de-excitations on the first transitions may occur before the final, RAMAN photon is emitted, see figure 3.3. For the calculation, each case of N additionally scattered photons has to be treated individually.

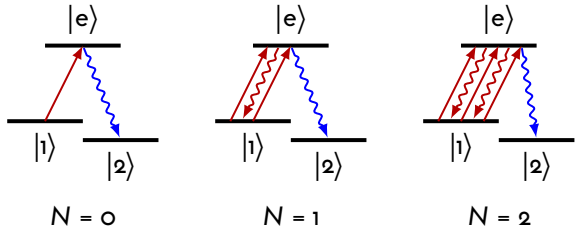

Figure 3.3 – The three cases of RAMAN scattering with 0, 1, or 2 additional photons emitted at the transition $|1\rangle \leftrightarrow |e\rangle$.

Thus, the final states for these cases read,

$$|f_N\rangle = |2\rangle \otimes \left|1_{\omega_1'}, 1_{\omega_1''}, \ldots, 1_{\omega_1^{(N)}}, 1_{\omega_2}\right\rangle,$$

with the occupation number 1 in each mode of the additionally scattered photons and of the final, RAMAN photon.

Under the assumption that all information about the additionally scattered photons is lost (a so-called MARKOV chain), the full spectrum of the final photon is given by the incoherent sum over all possible cases of N additional photon emissions, weighted by the corresponding success probabilities,

$$S(\omega_2) = \sum_{N=0}^{\infty} P_{\text{scatter},N} S_N(\omega_2), \tag{3.5}$$

and including the integration over all their possible frequencies,

$$S_N(\omega_2) = \int \cdots \int \left| U_{f_N i}(\omega_2) \right|^2 \mathrm{d}\omega_1' \ldots \mathrm{d}\omega_1^{(N)}.$$

3.2.1 Dressed states

For the explicit calculation the equivalent reference frame of dressed states is used where the HAMILTON operator takes the form [19],

$$\hat{H}' = \hat{H}_0' + \hat{V} + \hat{V}_L.$$

The eigenfrequency of the initial atomic state is shifted by the laser frequency, $-\omega_A \to -\omega_A + \omega_1 =: \Delta_1$, and the interaction of laser and atom is described by the additional term,

$$\hat{V}_L = \frac{\hbar\Omega}{2} \left(|1\rangle\langle e| + |e\rangle\langle 1| \right),$$

with the on-resonance RABI frequency Ω. Due to this interaction term the states $|1\rangle$ and $|e\rangle$ are replaced by dressed states with the complex eigenfrequencies

$$\omega_\pm = \frac{1}{2} \left(\Delta_1 - \mathrm{i}\frac{\Gamma}{2} \pm \sqrt{|\Omega|^2 + \left(\Delta_1 + \mathrm{i}\frac{\Gamma}{2} \right)^2} \right). \tag{3.6}$$

For each case of N the matrix element of the time-evolution operator is calculated as before, and the resolvent shows again resonances at each involved state. Thus, $U_{f_N i}(t)$ is a sum over $(3+2N)$ terms. For example, the five involved states for $N = 1$ are $|\omega_+\rangle$, $|\omega_-\rangle$, $|\omega_+\rangle \otimes |1_{\omega'}\rangle$, $|\omega_-\rangle \otimes |1_{\omega'}\rangle$, and $|2\rangle \otimes |1_{\omega'}, 1_{\omega_2}\rangle$.
The detailed calculation of the three cases $N = 0$, 1, and 2 including the full expressions for $U_{f_N i}(t)$ are presented in the article [82], and not repeated here. For the limit $t \to \infty$ only one term in $U_{f_N i}$ remains, and the resulting spectral density is the same for all cases,

$$S_N(\Delta_2) = \frac{\kappa(\Gamma - \kappa) \left((\Delta_1 + 2\Delta_S)^2 + \frac{\Gamma^2}{4} \right)}{2\pi\Gamma \left| \left(\Delta_2 - \Delta_1 - \Delta_S + \mathrm{i}\frac{\kappa}{2} \right) \left(\Delta_2 + \Delta_S + \mathrm{i}\frac{\Gamma-\kappa}{2} \right) \right|^2}. \tag{3.7}$$

This is a product of two LORENTZian functions centred at $\Delta_2 = \Delta_1 + \Delta_S$ and $\Delta_2 = -\Delta_S$, and with the respective widths

$$\kappa = \Gamma \frac{\Delta_S}{\Delta_1 + 2\Delta_S} \qquad \text{and} \qquad \Gamma - \kappa.$$

Therein, Δ_S denotes the AC STARK shift due to the presence of the exciting laser field,

$$\Delta_S = -\frac{\Delta_1}{2} + \frac{\operatorname{sgn}\Delta_1}{2\sqrt{2}} \sqrt{\Omega_{\text{eff}}^2 - \frac{\Gamma^2}{4} + \sqrt{\left(\Omega_{\text{eff}}^2 - \frac{\Gamma^2}{4}\right)^2 + \Delta_1^2 \Gamma^2}},$$

introducing the effective RABI frequency, $\Omega_{\text{eff}} = \sqrt{|\Omega|^2 + \Delta_1^2}$. With these characteristic parameters the dressed states' energies (3.6) take the form

$$\omega_+ = \Delta_1 + \Delta_S - \mathrm{i}\frac{\kappa}{2} \qquad \text{and} \qquad \omega_- = -\Delta_S - \mathrm{i}\frac{\Gamma - \kappa}{2}.$$

The success probabilities turn out to be

$$P_{\text{scatter},N} = \frac{A_2}{\Gamma} \left(\frac{A_1}{\Gamma}\right)^N,$$

where the results for the first three cases of $N = 0$, 1, and 2 were explicitly found (see again [82]). Even though a mathematical proof is pending, they are generalised to all cases due to their appearance (a so-called «proof by obviousness»).

3.2.2 Results for laser excitation

In the same manner as before on p. 49, the power spectral density (3.7) is rewritten as a superposition,

$$\begin{aligned} S_N(\Delta_2) &= \frac{C}{2\pi} \cdot \left| \frac{1}{\Delta_2 - \Delta_1 - \Delta_S + \mathrm{i}\frac{\kappa}{2}} - \frac{1}{\Delta_2 + \Delta_S + \mathrm{i}\frac{\Gamma - \kappa}{2}} \right|^2 \\ &= C \cdot \left| \frac{1}{\sqrt{\kappa}} \underbrace{L_\kappa(\Delta_2 - \Delta_1 - \Delta_S)}_{\text{RAMAN}} - \frac{1}{\sqrt{\Gamma - \kappa}} \underbrace{L_{\Gamma-\kappa}(\Delta_2 + \Delta_S)}_{\text{spontaneous}} \right|^2, \end{aligned} \tag{3.8}$$

with the constant pre-factor,

$$C = \frac{\kappa(\Gamma - \kappa)}{\Gamma} \cdot \frac{\left|\Delta_1 + 2\Delta_S + \mathrm{i}\frac{\Gamma}{2}\right|^2}{\left|\Delta_1 + 2\Delta_S + \mathrm{i}\frac{\Gamma - 2\kappa}{2}\right|^2}.$$

Here too, the emitted photon is a superposition of two Lorentzian spectral states weighted by the reciprocal square roots of their respective widths. In this case though, the Raman peak is always narrowband ($\kappa < \Gamma$) and dominates the spectrum. The two peaks are shifted further away from each other to a total difference of $(\Delta_1 + 2\Delta_S)$ instead of Δ_1, and as a result they do not merge in the case of near-resonant excitation if it is strong enough ($\Omega > \Gamma/2$). The emission spectra of figure 3.4 illustrate these characteristics.

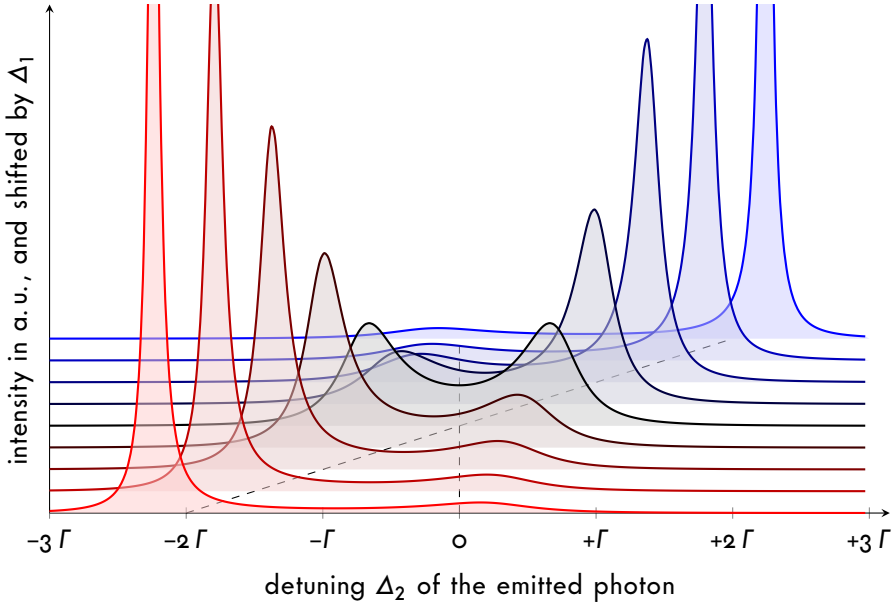

Figure 3.4 – A set of emission spectra for strong laser excitation with $|\Omega| = 3/2\,\Gamma$ and several values of Δ_1 from $-2\,\Gamma$ (red-detuned) to $+2\,\Gamma$ (blue-detuned). Each spectrum consists of two Lorentzian components with considerably different linewidths and weights. The dashed lines indicate the position of the two line centres in the absence of the Stark shift ($\Delta_S = 0$, i.e. for $|\Omega| < \Gamma/2$).

In this regime, the peaks are separated by

$$\sqrt{|\Omega|^2 - \frac{\Gamma^2}{4}}$$

at resonance. This kind of avoided crossing of line centres is known as the Autler–Townes splitting [5], a consequence of the AC Stark effect of the exciting laser field. The energy levels of the dressed states in case of exactly resonant excitation ($\Delta_1 = 0$) are shown in figure 3.5. They exhibit a sudden splitting at a Rabi frequency of $|\Omega| = \Gamma/2$.

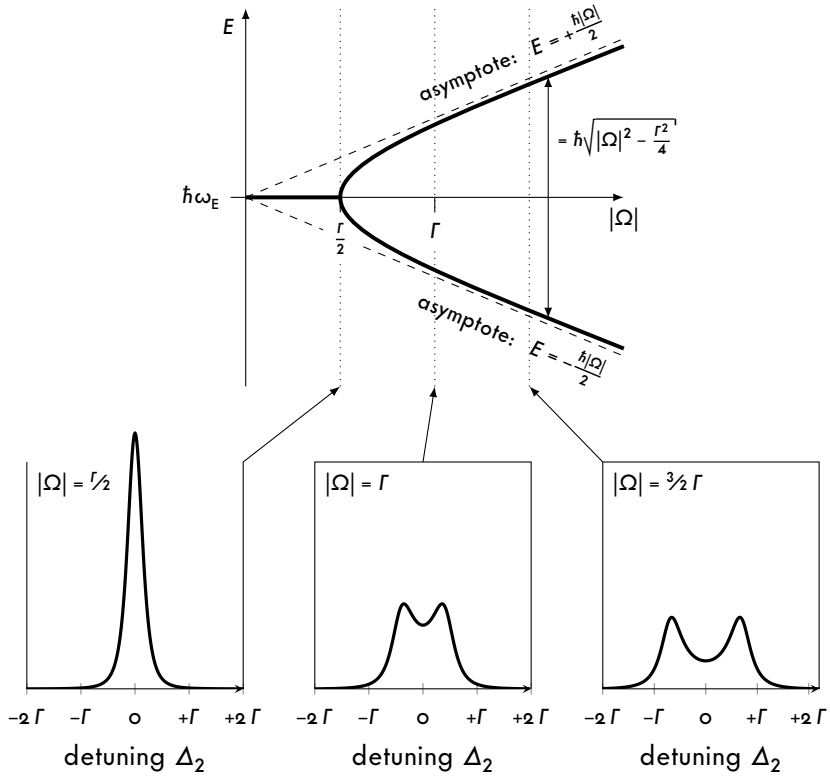

Figure 3.5 – AUTLER–TOWNES splitting of the dressed states' energy E shown for the case of resonant excitation, $\Delta_1 = 0$. The points on the line correspond to the centres of the LORENTZian curves in eq. (3.8). The dotted vertical cuts correspond to three spectra below that illustrate the splitting of the emission line with growing laser power.

The two cases of excitation by a low-intensity laser ($\Omega \to 0$) and a narrow-linewidth single photon ($\Delta\omega_1 \to 0$) converge to the same emission spectrum, $\kappa \to 0$ in eq. (3.7) and $\psi_2(\Delta_2 - \Delta_1) = \delta(\Delta_2 - \Delta_1)$ in eq. (3.3), respectively. This shows that a single narrow-linewidth photon acts in the same manner as an extremely weak laser beam—a statement holding for the spectra only, as the photon statistics of these two sources still differ fundamentally.

Furthermore it is a reasonable presumption that a small, but non-vanishing linewidth of the laser (such as 150 kHz $\ll \Gamma$, see section 1.4.5 on p. 19) does practically not change the results.

3.3 Temporal structures

Spectrum and wave packet of single photons are equally interesting to study and both are two sides of the same coin. It is flipped by FOURIER transformation of the wave function. The following investigation of wave packets results from this method.

3.3.1 Single-photon excitation

In the case of excitation by a single photon the emitted photon is in a pure quantum state $|\psi_2\rangle$ identified as a FOURIER-limited wave packet. Thus, its temporal structure follows from the FOURIER transformation of its spectral amplitude function, eq. (3.3). For excitation by a LORENTZian spectrum (sec. 3.1.3) the arrival-time distribution of the wave packet is a superposition of two exponential decays,

$$R(t) = \frac{2\pi A_1 A_2 \Delta\omega_1}{\Delta_1^2 - \left(\frac{\Gamma-\Delta\omega_1}{2}\right)^2}\Theta(t)\left|e^{-i(\omega_E+\Delta_1)t}e^{-\frac{\Delta\omega_1}{2}t} - e^{-i\omega_E t}e^{-\frac{\Gamma}{2}t}\right|^2. \tag{3.9}$$

If the two linewidths, Γ and $\Delta\omega_1$, are of similar value and distinctly smaller than the detuning Δ_1, the wave packet exhibits an interference pattern with a beat frequency equal to the detuning, see figure 3.6.

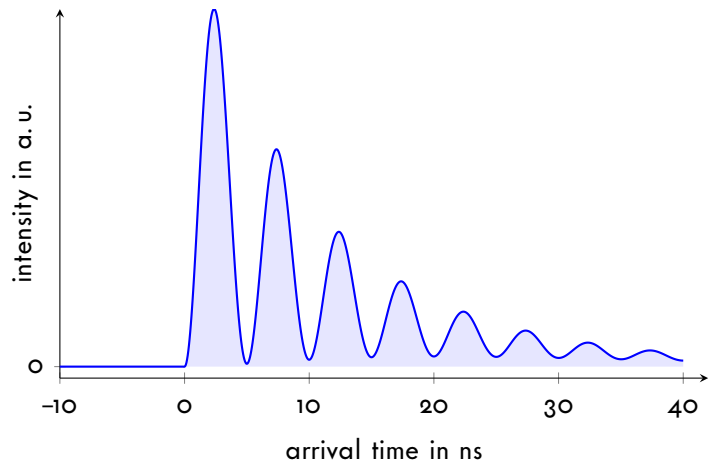

Figure 3.6 – Wave packet of a RAMAN photon generated by single-photon excitation according to eq. (3.9) with $\Gamma = 2\pi \cdot 23\,\text{MHz}$, $\Delta\omega_1 = 2\pi \cdot 10\,\text{MHz}$, and $\Delta_1 = 2\pi \cdot 200\,\text{MHz}$.

3.3.2 laser excitation

To quantify the temporal distribution of the RAMAN photon in the case of laser excitation is more elaborate as all previously emitted photons have to be taken into account: It is assumed that after each spontaneously emitted photon on the transition $|e\rangle \to |1\rangle$, the emitter is projected back onto the initial state $|1\rangle$, and the excitation process starts again. For each photon emitted after such a projection, the temporal shape of its wave packet is the square of the absolute value of the FOURIER transformation of the amplitude spectrum (that on its own is the square root of S_N, eq. (3.8)),

$$p_1(t) = C\Theta(t)\left|e^{-i(\omega_E+\Delta_1+\Delta_S)t}e^{-\frac{\kappa}{2}t} - e^{-i(\omega_E-\Delta_S)t}e^{-\frac{\Gamma-\kappa}{2}t}\right|^2, \tag{3.10}$$

that is again a superposition of two exponential decays. As this distribution describes the uncertain instance of time when the photon is emitted, the wave packet of the next photon is broadened accordingly, i. e. its temporal shape $p_2(t)$ is the convolution of the temporal shape of the first photon with itself.[2] Consequently, the temporal shape of the N-th photon is the convolution of the previous one with $p_1(t)$,

$$p_N(t) = (p_{N-1} * p_1)(t).$$

In the case of a convolution of probability distributions one finds for the first moment,

$$\langle t\rangle_N = \int p_N(t)t\,\mathrm{d}t = \langle t\rangle_{N-1} + \langle t\rangle_1,$$

and for the second central moment,

$$(\Delta t)_N^2 = \langle(t - \langle t\rangle_N)^2\rangle_N = (\Delta t)_{N-1}^2 + (\Delta t)_1^2.$$

Thus, the N-th photon has a mean arrival time of $\langle t\rangle_N = N\langle t\rangle_1$, and a temporal spread of $(\Delta t)_N = \sqrt{N}(\Delta t)_1$.
From this the mean arrival time of the RAMAN photon is finally found by summing over all cases of N previously emitted photons weighted by their probabilities (cf. eq. (3.5)),

$$\langle t\rangle_{\text{Raman}} = \sum_{N=0}^{\infty} P_{\text{scatter},N}\langle t\rangle_{N+1} = (\bar{N}+1)\langle t\rangle_1.$$

2) Note that any possible interference between the spontaneously emitted photons on transition $|1\rangle \leftrightarrow |e\rangle$ are traced out (MARKOV chain).

Through a corresponding calculation the spread of the arrival time of the RAMAN photon is given by

$$(\Delta t)_{\text{Raman}} = (\bar{N} + 1)(\Delta t)_1 .$$

This shows that the RAMAN photon is temporally broadened by a factor equal to the mean number of spontaneously emitted photons including this final one, and with $\bar{N} + 1 = \Gamma/A_2$ it demonstrates the significance of the branching ratio in this case.

3.4 Résumé

The method presented and used in this chapter is a universal tool to calculate the spectra of RAMAN-scattering processes and to understand and quantify many of the emerging effects. The important conclusions are:

- The RAMAN photon created by single-photon excitation is fully coherent, i. e. FOURIER limited.
- The success probability is limited by the product of the branching fractions, $A_1 A_2$.
- Laser excitation on the other hand generates the photon with 100 % probability, but its coherence is reduced due to backscattering.
- This incoherence is not observed as a spectral broadening, but solely as a temporal extension of the wave packet (by the factor Γ/A_2).
- In both excitation scenarios the branching ratio plays an important role, but these two roles are totally different from each other.

RAMAN spectra for some other input spectra are presented in the article [82].

Remarks: If the incident single photon is in fact a stream of single photons, e. g. in the case of an SPDC source (see sec. 1.5), the generated RAMAN photon is in a mixed state, and thus not fully coherent anymore. Its coherence is dependent on the intensity of the single-photon source by means of loosing the information, which photon is absorbed—just as in the case of laser excitation. This effect is negligible in the experiments presented in this thesis, but must be kept in mind for future developments. To overcome it the incident photons could be heralded to filter out the immediate emission events, a well feasible possibility in the case of SPDC photon pairs. The resulting spectrum of that scenario is again equal to the one of a true single photon.

The spectra presented in the last section of the article [82, sec. IV.] are erroneous. It concerns the application of the presented model to quantum beats that result from two simultaneous RAMAN transitions via the same excited state. These errors were noticed not before publication, but far after it. They result from the approximation that the two excitations do not influence each other, i. e. the possibility was neglected that one excitation leads to a transfer of population to the other initial energy eigenstate. It turned out that this effect is too large to be negligible. Thus, these erroneous results are not recapitulated here. For a detailed investigation and the correct spectra see the forthcoming thesis of Matthias KREIS.

3.5 Alternative calculation for laser excitation

Here, the spontaneous RAMAN process is modelled using the LINDBLAD equation (4.1) on p. 64 for a three-level system. A coherent interaction with RABI frequency Ω tuned to the transition $|1\rangle \leftrightarrow |e\rangle$ with a detuning Δ competes with the decay of the upper state $|e\rangle$ to the final state $|2\rangle$ with the rate Γ (see figure 3.7). In opposition to the general case of figure 3.1 on p. 45, the decay back to the initial state $|1\rangle$ is neglected by choosing $A_1 = 0$ and $A_2 = \Gamma$. This is an eligible approximation to the RAMAN transition $D_{5/2}$–$P_{3/2}$–$S_{1/2}$ in $^{40}Ca^+$ with a branching ratio of $A_1/A_2 = 6.28(5)\,\%$, see table 1.1 on p. 12. Thus, the emitted photon has a high coherence close to the FOURIER limit.

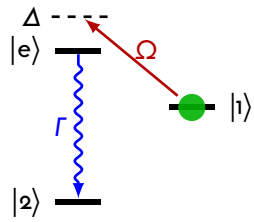

Figure 3.7 – The level scheme of a spontaneous RAMAN transition neglecting decay back to the initial state, cf. figure 3.1.

The coherent interaction is modelled based on the HAMILTON operator of the two-level system $|1\rangle$–$|e\rangle$, eq. (2.8) on p. 32 (cf. section 2.2 for details). Here, the excited state is used as energy reference, and the system is extended by the third state $|2\rangle$

with the energy $\hbar\omega_E$ of one emitted photon missing, thus:

$$\hat{H} = \hbar \begin{pmatrix} \Delta & \frac{\Omega^*}{2} & 0 \\ \frac{\Omega}{2} & 0 & 0 \\ 0 & 0 & -\omega_E \end{pmatrix}.$$

The decay is modelled by the operator $\hat{C} = \sqrt{\Gamma}|2\rangle\langle e|$. Both operators are fed into the LINDBLAD equation (4.1),

$$\frac{d}{dt}\hat{\rho} = \frac{i}{\hbar}\left[\hat{\rho}, \hat{H}\right] + \frac{1}{2}\left(2\hat{C}\hat{\rho}\hat{C}^+ - \hat{\rho}\hat{C}^+\hat{C} - \hat{C}^+\hat{C}\hat{\rho}\right).$$

Starting in the initial state $\hat{\rho}(0) = |1\rangle\langle 1|$ at time $t = 0$, the time evolution

$$\boldsymbol{\rho}'(t) = e^{\hat{\mathcal{L}}t}\boldsymbol{\rho}'(0)$$

for the vectorised operators[3] with the LIOUVILLE superoperator $\hat{\mathcal{L}}$ leads for $t \geq 0$ to the solution

$$\hat{\rho}(t) = |\phi(t)\rangle\langle\phi(t)| + \left(1 - \langle\phi(t)|\phi(t)\rangle\right)|2\rangle\langle 2|.$$

There, $|\phi(t)\rangle$ is a non-normalised superposition state of $|1\rangle$ and $|e\rangle$, corresponding to the not-yet decayed amount of the atomic state,

$$|\phi(t)\rangle = \frac{1}{N}\left(e^{-\frac{\kappa}{2}t - i(\Delta+\Delta_S)t}\begin{pmatrix} \Delta + \Delta_S + i\frac{\Gamma-\kappa}{2} \\ \frac{\Omega}{2} \\ 0 \end{pmatrix} - e^{-\frac{\Gamma-\kappa}{2}t + i\Delta_S t}\begin{pmatrix} -\Delta_S + i\frac{\kappa}{2} \\ \frac{\Omega}{2} \\ 0 \end{pmatrix}\right),$$

with the same characteristic parameters as before (in section 3.2),

$$\kappa = \Gamma\frac{\Delta_S}{\Delta + 2\Delta_S},$$

$$\Delta_S = -\frac{\Delta}{2} + \frac{\operatorname{sgn}\Delta}{2\sqrt{2}}\sqrt{\Omega_{\text{eff}}^2 - \frac{\Gamma^2}{4} + \sqrt{\left(\Omega_{\text{eff}}^2 - \frac{\Gamma^2}{4}\right)^2 + \Delta^2\Gamma^2}},$$

$$\Omega_{\text{eff}} = \sqrt{|\Omega|^2 + \Delta^2},$$

3) See section 4.1 on p. 64 for details.

and a pre-factor,

$$N = \left| \Delta + 2\Delta_S + i\frac{\Gamma - 2\kappa}{2} \right|.$$

The probability amplitude to find the atom in the excited state at the time t is proportional to $\langle e|\phi(t)\rangle$, which leads to the temporal probability-amplitude function of the emitted photon,

$$R(t) = \sqrt{N'}\, e^{-i\omega_E t} \langle e|\phi(t)\rangle = -i\sqrt{C}\,\Theta(t) \left(e^{-\frac{\kappa}{2}t - i(\omega_E + \Delta + \Delta_S)t} - e^{-\frac{\Gamma-\kappa}{2}t - i(\omega_E - \Delta_S)t} \right). \tag{3.11}$$

Therein, a phase factor given by the optical carrier frequency ω_E of the emission transition and a normalisation factor N' complete the formula. The result is the same as the wave packet of the first emitted photon in the general model, eq. (3.10) on p. 56, a fact owed to the neglected back scattering. Its FOURIER transformation leads to the amplitude spectrum,

$$R(\omega) = \sqrt{\frac{C}{2\pi}} \left(\frac{1}{\omega - \omega_E - \Delta - \Delta_S + i\frac{\kappa}{2}} - \frac{1}{\omega - \omega_E + \Delta_S + i\frac{\Gamma-\kappa}{2}} \right), \tag{3.12}$$

depicting a superposition of two LORENTZian amplitude spectra that are weighted by the reciprocal square roots of their respective widths—the same result as before in section 3.2.2.

3.6 The RAMAN operator

Furthermore, the whole process is easily expressed in representation-independent notation through a single operator called RAMAN operator,

$$\hat{R} = \hat{R}_{\omega_E, \Gamma, \Delta, \Omega, \Delta\omega} = |\psi_f\rangle\langle\psi_i| = |2\rangle \otimes \left|R_{\omega_E, \Gamma, \Delta, \Omega, \Delta\omega}\right\rangle \langle 1| \otimes \langle\Phi|, \tag{3.13}$$

that transforms the initial state $|1\rangle$ of the atom into the joint state $|\psi_f\rangle = |\psi(t \to \infty)\rangle = \hat{R}|\psi_i\rangle = |2\rangle \otimes |R\rangle$ of atom and emitted photon through the presence of a light field of the state $|\Phi\rangle$. The characterising parameters are the natural frequency ω_E of the emission transition, the decay constant Γ of the excited state, and the detuning Δ, RABI frequency Ω, and linewidth $\Delta\omega$ of the exciting light. The state in which the exciting light field remains after the process is omitted in this description.
The two cases of the previous sections are hence represented in the following way: Excitation by laser light implies Φ to be a coherent field state in the language of the second quantisation. It is characterised only by detuning (or carrier frequency)

and Rabi frequency as the linewidth of the laser is assumed to be much more narrow than the atomic transition, i. e. $\Delta\omega \ll \Gamma$, practically setting $\Delta\omega \to 0$, thus

$$\hat{R}_{\text{laser}} = \hat{R}_{\omega_E,\Gamma,\Delta,\Omega} = |2\rangle\big|R_{\omega_E,\Gamma,\Delta,\Omega(,\Delta\omega\to 0)}\big\rangle\langle 1|\big\langle\Phi_{\Delta,\Omega}\big|.$$

Photonic excitation, on the other hand, is characterised by the detuning (or carrier frequency) and the (coherent) linewidth of the single photon, and assigning the photon a vanishing Rabi frequency $\Omega \to 0$ in the language of lasers, thus

$$\hat{R}_{\text{photon}} = \hat{R}_{\omega_E,\Gamma,\Delta,\Delta\omega} = |2\rangle\big|R_{\omega_E,\Gamma,\Delta(,\Omega\to 0),\Delta\omega}\big\rangle\langle 1|\big\langle\Phi_{\Delta,\Delta\omega}\big|.$$

The representation in frequency space is thus given by the scalar product with a frequency eigenstate of the emitted photon, $R(\omega) = \langle\omega|R\rangle$, corresponding to eq. (3.12), and the representation in the temporal domain by the product with a temporal eigenstate of the photon, $R(t) = \langle t|R\rangle$, i. e. the Fourier transformation of the aforementioned.
The calculation of the quantum interface in chapter 5 is based on this operator and thereby much more transparent and concise as other approaches.

Chapter 4

The Matlab programme

«Shut up and calculate!»

— ~~R. P. Feynman~~ N. D. Mermin (2004)[77]

To investigate the internal dynamics of the $^{40}Ca^{+}$ ion in detail, a computer programme for the dynamics of its eighteen internal levels has been written. The programming language of choice is Matlab (abbrev. for matrix laboratory), a trademark of «The MathWorks, Inc.». This chapter describes the mathematical principles on which it is based as well as its implementation as a set of easy-to-use Matlab functions.

The programme has already been used over the past years as visible in the theses of the author's co-workers [47, 62, 112] and in some publications [111, 113].

This chapter starts with a recapitulation of the equation of motion that is the mathematical basis of the programme. In section 4.2, it is applied to the relevant electronic energy levels of the calcium ion. The final section (sec. 4.3) concerns the implementation in Matlab including some examples of its use.

4.1 The master-equation formalism in general

The programme is based on the KOSSAKOWSKI–LINDBLAD equation [55, 69, 78]:

$$\frac{\mathrm{d}}{\mathrm{d}t}\hat{\rho} = \frac{\mathrm{i}}{\hbar}\left[\hat{\rho}, \hat{H}\right] + \frac{1}{2}\sum_{k=1}^{m}\left(2\hat{C}_k\hat{\rho}\hat{C}_k^{+} - \hat{\rho}\hat{C}_k^{+}\hat{C}_k - \hat{C}_k^{+}\hat{C}_k\hat{\rho}\right) \tag{4.1}$$

This is an equation of motion for the density operator $\hat{\rho}$ in the n-dimensional HILBERT space $\mathcal{H}$. The reversible/coherent part of the evolution is given by the first term on the right-hand side governed by the HAMILTON operator $\hat{H}$, while the second term treats the irreversible/non-unitary part of the evolution due to dissipation to the environment governed by the so-called relaxation operators $\hat{C}_k$. One example of such dissipative processes is the decay of an internal state $|i\rangle$ into another state $|f\rangle$ under emission of a photon into the environment. The relaxation operator for this example is $\hat{C} = \sqrt{\Gamma}|f\rangle\langle i|$ assuming a decay rate Γ.
As eq. (4.1) is linear in $\hat{\rho}$, a linear superoperator $\hat{\mathcal{L}}$, the LIOUVILLE operator, in the product space $\mathcal{H}\otimes\mathcal{H}$ is found that acts on the n^2-dimensional vector $\boldsymbol{\rho}'$ containing the components of the density operator row-wise stacked, i. e. according to

$$\rho_{i,j} = \rho'_{(i-1)n+j} \tag{4.2}$$

with $i, j \in \{1, \ldots, n\}$. Hence, the equation of motion takes the form

$$\frac{\mathrm{d}}{\mathrm{d}t}\boldsymbol{\rho}' = \hat{\mathcal{L}}\cdot\boldsymbol{\rho}', \tag{4.3}$$

and the time evolution of the system is simply given by

$$\boldsymbol{\rho}'(t) = \mathrm{e}^{\int \hat{\mathcal{L}}\,\mathrm{d}t}\boldsymbol{\rho}'(0).$$

Using the KRONECKER product in $\mathcal{H}\otimes\mathcal{H}$ and introducing the non-HERMITian so-called effective HAMILTON operator

$$\hat{H}_{\mathrm{eff}} = \frac{\hat{H}}{\hbar} - \frac{\mathrm{i}}{2}\sum_{k=1}^{m}\hat{C}_k^{+}\hat{C}_k,$$

eq. (4.1) is rewritten into eq. (4.3) with the LIOUVILLE operator having the form

$$\hat{\mathcal{L}} = \mathrm{i}\left(\mathbb{1}\otimes\hat{H}_{\mathrm{eff}}^{*} - \hat{H}_{\mathrm{eff}}\otimes\mathbb{1}\right) + \sum_{k}\hat{C}_k\otimes\hat{C}_k^{*}. \tag{4.4}$$

Please note that the sign * indicates complex conjugation only. For the explicit derivation of $\hat{\mathcal{L}}$ see the appendix (sec. A1 on p. 113).

4.2 The master equation for the 18-level system

The Matlab programme restricts itself to the internal dynamics of a $^{40}Ca^{+}$ ion, more precisely to its five lowest energy terms that are split into eighteen sub-levels by the present static magnetic field. The relevant additional energy term, due to the linear Zeeman effect, is $-\hat{\boldsymbol{\mu}}_J \cdot \boldsymbol{B}_0$, which shifts all 18 sub-levels according to their magnetic quantum number m_J and the respective Landé factor g_J. In the following description the sub-levels are numbered according to figure 4.1, from 1 to 18.

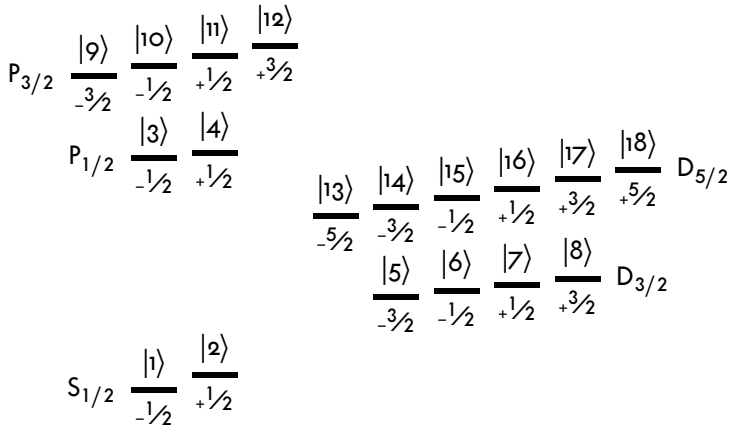

Figure 4.1 – The 18 lowest energy sub-levels of $^{40}Ca^{+}$ (cf. fig. 1.2) showing the numbering used in the Matlab programme. The values below each level indicate the magnetic quantum number m_J of the respective state. Energy differences are not to scale.

Similarly the seven relevant transition channels (fig. 1.2 on p. 11) are split into 56 sub-channels (see fig. A.1 on p. 117). As this splitting is owed to spin–orbital coupling, it connects the photon's spin with the change in the magnetic quantum number of the ion, and thus the geometry as well as the Clebsch–Gordan coefficients (c_{CG}) enter the coupling strength of all these sub-channels. The following subsections provide details to this.

4.2.1 Spontaneous decays

On each transition channel, spontaneous decay is possible, and modelled as relaxation operators in the form $\hat{C} = \sqrt{\Gamma}|f\rangle\langle i|$ as mentioned above. If photons emitted on different (sub-)channels are indistinguishable for the environment, they must be modelled conjointly as a single relaxation operator. For a small Zeeman

splitting compared to the decay rate, this is the case just for sub-channels of the same transition and with the same polarisation. Thus, there are 25 decay operators $\hat{C}_{k,\Delta m}$ for the 56 sub-channels in total, where k stands for the transition number (0–6) and Δm for the change in the z-component of the atomic total angular momentum.
The Einstein coefficients A_k of each transition (given in table 1.1 on p. 12) are distributed to the sub-channels according to the spin–orbital coupling, thus the Clebsch–Gordan coefficients (given in fig. A.1 on p. 117) appear as factors in the relaxation operators of the spontaneous decay.
In detail, these operators are:

1. for transition no. 1 ($P_{1/2} \to S_{1/2}$)

$$\hat{C}_{1,+1} = -\sqrt{A_1}\sqrt{2/3}\,|1\rangle\langle 4|$$
$$\hat{C}_{1,\pm 0} = \sqrt{A_1}\sqrt{1/3}\,(|2\rangle\langle 4| - |1\rangle\langle 3|)$$
$$\hat{C}_{1,-1} = \sqrt{A_1}\sqrt{2/3}\,|2\rangle\langle 3|$$

2. for transition no. 2 ($P_{1/2} \to D_{3/2}$)

$$\hat{C}_{2,+1} = \sqrt{A_2}\left(\sqrt{1/2}\,|5\rangle\langle 3| + \sqrt{1/6}\,|6\rangle\langle 4|\right)$$
$$\hat{C}_{2,\pm 0} = -\sqrt{A_2}\sqrt{1/3}\,(|6\rangle\langle 3| + |7\rangle\langle 4|)$$
$$\hat{C}_{2,-1} = \sqrt{A_2}\sqrt{1/6}\left(|7\rangle\langle 3| + \sqrt{1/2}\,|8\rangle\langle 4|\right)$$

3. for transition no. 3 ($P_{3/2} \to S_{1/2}$)

$$\hat{C}_{3,+1} = \sqrt{A_3}\sqrt{1/3}\,(|1\rangle\langle 11| + \sqrt{3}|2\rangle\langle 12|)$$
$$\hat{C}_{3,\pm 0} = \sqrt{A_3}\sqrt{2/3}\,(|1\rangle\langle 10| + |2\rangle\langle 11|)$$
$$\hat{C}_{3,-1} = \sqrt{A_3}\sqrt{1/3}\,(\sqrt{3}|1\rangle\langle 9| + |2\rangle\langle 10|)$$

4. for transition no. 4 ($P_{3/2} \to D_{3/2}$)

$$\hat{C}_{4,+1} = \sqrt{A_4}\sqrt{1/15}\left(-\sqrt{6}|5\rangle\langle 10| - \sqrt{8}|6\rangle\langle 11| - \sqrt{6}|7\rangle\langle 12|\right)$$
$$\hat{C}_{4,\pm 0} = \sqrt{A_4}\sqrt{1/15}\,(-3|5\rangle\langle 9| - |6\rangle\langle 10| + |7\rangle\langle 11| + 3|8\rangle\langle 12|)$$
$$\hat{C}_{4,-1} = \sqrt{A_4}\sqrt{1/15}\left(+\sqrt{6}|6\rangle\langle 9| + \sqrt{8}|7\rangle\langle 10| + \sqrt{6}|8\rangle\langle 11|\right)$$

5. for transition no. 5 ($D_{5/2} \rightarrow S_{1/2}$)

$$\begin{aligned}
\hat{C}_{5,+2} &= \sqrt{A_5}\sqrt{1/5}\,(|1\rangle\langle 17| + \sqrt{5}|2\rangle\langle 18|)\\
\hat{C}_{5,+1} &= \sqrt{A_5}\sqrt{1/5}\,(\sqrt{2}|1\rangle\langle 16| + 2|2\rangle\langle 17|)\\
\hat{C}_{5,\pm 0} &= \sqrt{A_5}\sqrt{1/5}\,(\sqrt{3}|1\rangle\langle 15| + \sqrt{3}|2\rangle\langle 16|)\\
\hat{C}_{5,-1} &= \sqrt{A_5}\sqrt{1/5}\,(2|1\rangle\langle 14| + \sqrt{2}|2\rangle\langle 15|)\\
\hat{C}_{5,-2} &= \sqrt{A_5}\sqrt{1/5}\,(\sqrt{5}|1\rangle\langle 13| + |2\rangle\langle 14|)
\end{aligned}$$

6. for transition no. 6 ($P_{3/2} \rightarrow D_{5/2}$)

$$\begin{aligned}
\hat{C}_{6,+1} &= \sqrt{A_6}\sqrt{1/15}\left(|16\rangle\langle 12| + \sqrt{3}|15\rangle\langle 11| + \sqrt{6}|14\rangle\langle 10| + \sqrt{10}|13\rangle\langle 9|\right)\\
\hat{C}_{6,\pm 0} &= -\sqrt{A_6}\sqrt{1/15}\left(\sqrt{4}|17\rangle\langle 12| + \sqrt{6}|16\rangle\langle 11| + \sqrt{6}|15\rangle\langle 10| + \sqrt{4}|14\rangle\langle 9|\right)\\
\hat{C}_{6,-1} &= \sqrt{A_6}\sqrt{1/15}\left(\sqrt{10}|18\rangle\langle 12| + \sqrt{6}|17\rangle\langle 11| + \sqrt{3}|16\rangle\langle 10| + |15\rangle\langle 9|\right)
\end{aligned}$$

7. for transition no. 0 ($D_{3/2} \rightarrow S_{1/2}$)

$$\begin{aligned}
\hat{C}_{0,+2} &= -\sqrt{A_0}\sqrt{4/5}\,|1\rangle\langle 8|\\
\hat{C}_{0,+1} &= \sqrt{A_0}\sqrt{1/5}\,(-\sqrt{3}|1\rangle\langle 7| + |2\rangle\langle 8|)\\
\hat{C}_{0,\pm 0} &= \sqrt{A_0}\sqrt{1/5}\,(-\sqrt{2}|1\rangle\langle 6| + \sqrt{2}|2\rangle\langle 7|)\\
\hat{C}_{0,-1} &= \sqrt{A_0}\sqrt{1/5}\,(-|1\rangle\langle 5| + \sqrt{3}|2\rangle\langle 6|)\\
\hat{C}_{0,-2} &= \sqrt{A_0}\sqrt{4/5}\,|2\rangle\langle 5|
\end{aligned}$$

4.2.2 Coherent interactions

As described in chapter 2, the coherent interaction at each sub-channel $|g\rangle \leftrightarrow |e\rangle$ is expressed by a HAMILTON operator in the form of

$$\hat{H} = \frac{\hbar}{2}\left(\Omega_{ge}|e\rangle\langle g| + \Omega_{ge}^{*}|g\rangle\langle e| + \Delta(|g\rangle\langle g| - |e\rangle\langle e|)\right) = \frac{\hbar}{2}\begin{pmatrix} +\Delta & \Omega_{ge}^{*} \\ \Omega_{ge} & -\Delta \end{pmatrix} \qquad (4.5)$$

in the time-independent reference frame rotating with the laser frequency, cf. eq. (2.8) on p. 32. To keep such a reference frame for each transition, the detuning of the laser from the atomic resonance, $\Delta = \omega_L - \omega_A$, enters not only the two states $|g\rangle$ and $|e\rangle$, but also all states connected with these two via other laser

beams. Thus, all states connected with $|g\rangle$ receive a detuning of $+\frac{\Delta}{2}$, and all states connected with $|e\rangle$ receive a detuning of $-\frac{\Delta}{2}$. The same consideration must be done for the laser linewidths (see sec. 4.2.3).
To get the actual value of Ω_{ge} for a certain sub-channel, the total RABI frequency of the laser has to be multiplied by the proper CLEBSCH–GORDAN coefficient c_{CG} as well as the geometry factor $g_{|\Delta l|,\Delta m}$ according to section 2.3 on p. 33. In this way the direction and polarisation of each laser beam enters the coupling strength for each of the 56 sub-channels.

Remarks: For each laser only the transition to which it is close to resonance is taken into account. Its detuning to the other transitions is several orders of magnitude larger, in the regime of optical frequencies, and thus, these interactions are negligibly weak.
The magnetic dipole interaction between the two ZEEMAN sub-levels of $S_{1/2}$ is driven by the RF coil (sec. 1.4.5 on p. 20) but mathematically treated in the same way as the laser transitions. This requires a re-examination of the rotating-wave approximation as the transition is at radio frequency ($\approx 8\,\mathrm{MHz}$). But nevertheless, for typical RABI frequencies of about 1 MHz, this leads to a neglected BLOCH–SIEGERT shift [11] in the single-digit kHz-regime.

4.2.3 Linewidths of the lasers

Fluctuations of the laser frequencies wash out the coherent interaction of the lasers with the ion. These reduce the so-called coherences, the off-diagonal elements of the density operator. In the simulation, this is modelled by relaxation operators that take into account the couplings done by the respective laser and all couplings that the upper and lower states have via the other lasers. So, for a laser that is incoherently broadened with a linewidth of $\Delta\omega_L$ and connects the states $|g_i\rangle$ with the states $|e_i\rangle$ the corresponding operator is,

$$\hat{C}_L = \sqrt{\frac{\Delta\omega_L}{2}} \left(\sum_i |g_i\rangle\langle g_i| + \sum_k |k\rangle\langle k| - \sum_i |e_i\rangle\langle e_i| - \sum_l |l\rangle\langle l| \right), \tag{4.6}$$

where $|k\rangle$ and $|l\rangle$ are all states connected with $|g_i\rangle$ and $|e_i\rangle$, respectively, via other lasers. This formalism follows the example of a «Relaxation of Type T_2» as presented in [78].

4.2.4 Closed paths of atomic states

If the different laser beams allow more than one connection between two states of the atom, these excitation pathways interfere with each other dependent on the phase difference of the participating lasers. E. g. the states $S_{1/2}$ and $P_{3/2}$ are connected via the $D_{5/2}$ state by the 729 nm and the 854 nm transition, or directly by the 393 nm transition. As the different lasers are not necessarily phase-stable to each other, and the actual values of their phases at every point in time are unknown, it is not possible to simulate their interference. Thus, the programme has to assert, that there are no such closed paths for the given set of lasers that are switched on at the same time.
In the 18-level scheme of $^{40}Ca^{+}$ (fig. 1.2 on p. 11) without a 732 nm laser, only three closed paths exist:

- 393 nm ↔ 854 nm ↔ 729 nm
- 397 nm ↔ 866 nm ↔ 850 nm ↔ 393 nm
- 397 nm ↔ 866 nm ↔ 850 nm ↔ 854 nm ↔ 729 nm

In addition, the radio-frequency transition may close paths if it is switched on simultaneously with one of the blue lasers. This is also excluded by the programme.

4.2.5 Connections between atomic states

It is necessary to known, for a given set of lasers, which states are connected with each other to set up the linewidth operators of section 4.2.3. In the same manner the detuning values that fill up the diagonal of the total HAMILTON operator $\hat{H}_{\mathrm{tot}}$ are calculated. These connections are determined by the programme after closed paths have been excluded.
As a simple example, consider the cooling cycle in which only the 397 nm and the 866 nm lasers shine on the ion. In this case, according to eq. (4.5), the detuning of the first laser, or precisely $\hbar\Delta_{397}/2$, is added to both sub-levels of the $S_{1/2}$ manifold, and subtracted from $P_{1/2}$ as well as from $D_{3/2}$. The latter because of the connection by the 866 nm laser. This second laser's detuning is added to the four $D_{3/2}$ sub-levels, and subtracted from the other four ($S_{1/2}$ and $P_{1/2}$). Thus, the diagonal entries of $\hat{H}_{\mathrm{tot}}$ result to be $\Delta_{S_{1/2}} = \hbar(\Delta_{397}-\Delta_{866})/2$, $\Delta_{P_{1/2}} = -\hbar(\Delta_{397}+\Delta_{866})/2$, $\Delta_{D_{3/2}} = \hbar(-\Delta_{397}+\Delta_{866})/2$, and zero for the other ten sub-levels.
In addition to this, every sub-level is shifted individually by $g_J m_J \mu_B B_0$ due to the static magnetic field, hence e. g. $\Delta_6 = \hbar(\Delta_{866}-\Delta_{397})/2 - g_{D_{3/2}}\mu_B B_0/2$.

4.2.6 Everything together

Combining the previous considerations of this section leads to the resulting total HAMILTON operator as a block matrix in the unperturbed eigenbasis,

$$\hat{H}_{\mathrm{tot}} = \left(\begin{array}{c|c|c|c|c} \begin{matrix}\Delta_1 & \Omega_{\mathrm{RF}}^* \\ \Omega_{\mathrm{RF}} & \Delta_2\end{matrix} & \hat{H}_1^+ & \mathbb{0} & \hat{H}_3^+ & \hat{H}_5^+ \\ \hline \hat{H}_1 & \begin{matrix}\Delta_3 & \circ \\ \circ & \Delta_4\end{matrix} & \hat{H}_2 & \mathbb{0} & \mathbb{0} \\ \hline \mathbb{0} & \hat{H}_2^+ & \begin{matrix}\Delta_5 & \circ & \circ & \circ \\ \circ & \Delta_6 & \circ & \circ \\ \circ & \circ & \Delta_7 & \circ \\ \circ & \circ & \circ & \Delta_8\end{matrix} & \hat{H}_4^+ & \mathbb{0} \\ \hline \hat{H}_3 & \mathbb{0} & \hat{H}_4 & \begin{matrix}\Delta_9 & \circ & \circ & \circ \\ \circ & \Delta_{10} & \circ & \circ \\ \circ & \circ & \Delta_{11} & \circ \\ \circ & \circ & \circ & \Delta_{12}\end{matrix} & \hat{H}_6 \\ \hline \hat{H}_5 & \mathbb{0} & \mathbb{0} & \hat{H}_6^+ & \begin{matrix}\Delta_{13} & \circ & \circ & \circ & \circ & \circ \\ \circ & \Delta_{14} & \circ & \circ & \circ & \circ \\ \circ & \circ & \Delta_{15} & \circ & \circ & \circ \\ \circ & \circ & \circ & \Delta_{16} & \circ & \circ \\ \circ & \circ & \circ & \circ & \Delta_{17} & \circ \\ \circ & \circ & \circ & \circ & \circ & \Delta_{18}\end{matrix} \end{array}\right)$$

where each off-diagonal submatrix $\hat{H}_i$ covers the distribution of a RABI frequency Ω_i to the sub-channels of the respective transition (no. i). This results from the spin–orbital coupling and the coupling to the electromagnetic field, which are expressed by the CLEBSCH–GORDAN coefficients and the geometrical weighting factors, c_{CG} and $g_{|\Delta l|,\Delta m}$, respectively:

$$\hat{H}_1 = \frac{\hbar\Omega_1}{2}\begin{pmatrix} -\sqrt{1/3}\, g_{1,0}^{(1)} & \sqrt{2/3}\, g_{1,-1}^{(1)} \\ -\sqrt{2/3}\, g_{1,+1}^{(1)} & \sqrt{1/3}\, g_{1,0}^{(1)} \end{pmatrix}$$

$$\hat{H}_2 = \frac{\hbar\Omega_2}{2}\begin{pmatrix} \sqrt{1/2}\, g_{1,+1}^{(2)} & -\sqrt{1/3}\, g_{1,0}^{(2)} & \sqrt{1/6}\, g_{1,-1}^{(2)} & 0 \\ 0 & \sqrt{1/6}\, g_{1,+1}^{(2)} & -\sqrt{1/3}\, g_{1,0}^{(2)} & \sqrt{1/2}\, g_{1,-1}^{(2)} \end{pmatrix}$$

$$\hat{H}_3 = \frac{\hbar\Omega_3}{2}\begin{pmatrix} g^{(3)}_{1,-1} & 0 \\ \sqrt{2/3}\, g^{(3)}_{1,0} & \sqrt{1/3}\, g^{(3)}_{1,-1} \\ \sqrt{1/3}\, g^{(3)}_{1,+1} & \sqrt{2/3}\, g^{(3)}_{1,0} \\ 0 & g^{(3)}_{1,+1} \end{pmatrix}$$

$$\hat{H}_4 = \frac{\hbar\Omega_4}{2}\begin{pmatrix} -\sqrt{3/5}\, g^{(4)}_{1,0} & \sqrt{2/5}\, g^{(4)}_{1,-1} & 0 & 0 \\ -\sqrt{2/5}\, g^{(4)}_{1,+1} & -\sqrt{1/15}\, g^{(4)}_{1,0} & \sqrt{8/15}\, g^{(4)}_{1,-1} & 0 \\ 0 & -\sqrt{8/15}\, g^{(4)}_{1,+1} & \sqrt{1/15}\, g^{(4)}_{1,0} & \sqrt{2/5}\, g^{(4)}_{1,-1} \\ 0 & 0 & -\sqrt{2/5}\, g^{(4)}_{1,+1} & \sqrt{3/5}\, g^{(4)}_{1,0} \end{pmatrix}$$

$$\hat{H}_5 = \frac{\hbar\Omega_5}{2}\begin{pmatrix} 1\cdot g^{(5)}_{2,-2} & 0 \\ \sqrt{4/5}\, g^{(5)}_{2,-1} & \sqrt{1/5}\, g^{(5)}_{2,-2} \\ \sqrt{3/5}\, g^{(5)}_{2,0} & \sqrt{2/5}\, g^{(5)}_{2,-1} \\ \sqrt{2/5}\, g^{(5)}_{2,+1} & \sqrt{3/5}\, g^{(5)}_{2,0} \\ \sqrt{1/5}\, g^{(5)}_{2,+2} & \sqrt{4/5}\, g^{(5)}_{2,+1} \\ 0 & 1\cdot g^{(5)}_{2,+2} \end{pmatrix}$$

and

$$\hat{H}_6 = \frac{\hbar\Omega_6}{2\sqrt{15}}\begin{pmatrix} \sqrt{10}\, g^{(6)}_{1,+1} & -2g^{(6)}_{1,0} & g^{(6)}_{1,-1} & 0 & 0 & 0 \\ 0 & \sqrt{6}\, g^{(6)}_{1,+1} & -\sqrt{6}\, g^{(6)}_{1,0} & \sqrt{3}\, g^{(6)}_{1,-1} & 0 & 0 \\ 0 & 0 & \sqrt{3}\, g^{(6)}_{1,+1} & -\sqrt{6}\, g^{(6)}_{1,0} & \sqrt{6}\, g^{(6)}_{1,-1} & 0 \\ 0 & 0 & 0 & g^{(6)}_{1,+1} & -2g^{(6)}_{1,0} & \sqrt{10}\, g^{(6)}_{1,-1} \end{pmatrix}.$$

4.3 Implementation in Matlab

This section may be used as a manual for the Matlab programme as it explains the different implemented functions in detail. The author hopes that it serves users of the programme as a guide to build their own scripts of data analysis or modelling.

The kernel of the implementation is the file Liou18.m which calculates the LIOUVILLE operator $\hat{\mathcal{L}}$, eq. (4.4), out of the laser parameters and the magnetic field. Only laser excitations at six of the seven transitions are considered, the 732 nm transition (no. 0) is omitted. All parameters for these six possible laser beams have to

be input collectively as a single input argument, the so-called «laser matrix». Each laser is characterised by seven parameters: its total RABI frequency Ω, the detuning Δ off the natural atomic transition frequency, the linewidth $\Delta\omega$, two angles for the orientation, α and ε (acc. to sec. 2.3 on p. 33), and two angles of polarisation, θ and ϕ (acc. to sec. 1.1 on p. 7). The first three are given as technical frequencies in hertz, the four angles in radians. Thus, the laser matrix is a 6×7-dimensional array:

$$\text{LASER} = \begin{pmatrix} \Omega_1 & \Delta_1 & \Delta\omega_1 & \alpha_1 & \varepsilon_1 & \theta_1 & \phi_1 \\ \Omega_2 & \Delta_2 & \Delta\omega_2 & \alpha_2 & \varepsilon_2 & \theta_2 & \phi_2 \\ \Omega_3 & \Delta_3 & \Delta\omega_3 & \alpha_3 & \varepsilon_3 & \theta_3 & \phi_3 \\ \Omega_4 & \Delta_4 & \Delta\omega_4 & \alpha_4 & \varepsilon_4 & \theta_4 & \phi_4 \\ \Omega_5 & \Delta_5 & \Delta\omega_5 & \alpha_5 & \varepsilon_5 & \theta_5 & \phi_5 \\ \Omega_6 & \Delta_6 & \Delta\omega_6 & \alpha_6 & \varepsilon_6 & \theta_6 & \phi_6 \end{pmatrix} \begin{matrix} \text{for } 397\,\text{nm} \\ \text{for } 866\,\text{nm} \\ \text{for } 393\,\text{nm} \\ \text{for } 850\,\text{nm} \\ \text{for } 729\,\text{nm} \\ \text{for } 854\,\text{nm} \end{matrix}$$

The second input argument, called «Mag», is the value of the static magnetic field $|\boldsymbol{B}_0|$ in gauss ($= 10^{-4}$ tesla). If the radio-frequency transition in the $S_{1/2}$ is driven this is extended to a vector carrying additionally the strength (as a RABI frequency), radio frequency, and phase of that drive:

$$\text{Mag} = \left(|\boldsymbol{B}_0|\,,\, \Omega_{\text{RF}},\, \omega_{\text{RF}},\, \phi_{\text{RF}}\right)$$

4.3.1 Steady-state calculation

To simulate the ion's behaviour in continuous-wave excitation like most cases of spectroscopy, one has to determine the equilibrium or steady state of the ion under given conditions. The density operator of the steady state, $\hat{\rho}_{\text{st}}$, fulfils the condition

$$\frac{\mathrm{d}}{\mathrm{d}t}\hat{\rho}_{\text{st}} = \mathbb{0}.$$

This means the steady states lie in the null space of the LIOUVILLE operator, $\hat{\mathcal{L}}\boldsymbol{\rho}'_{\text{st}} = \mathbb{0}'$. It can be found by the Matlab function null.m through singular-value decomposition (SVD), but here a different method is used: GAUSSian elimination with partial pivoting through Matlab's fast backslash operation «\». This would lead to a problem as the inverse of the LIOUVILLE operator has to be applied to the zero vector, $\boldsymbol{\rho}'_{\text{st}} = \hat{\mathcal{L}}^{-1}\mathbb{0}'$, which is mathematically absurd. So, a simple trick is used. One row of $\hat{\mathcal{L}}$ is replaced by the unit matrix $\mathbb{1}$ written as a row vector $\mathbb{1}'$ the same way as eq. (4.2) with $\mathbb{1}'_{(i-1)n+i} = \delta_{i,i}$ and the respective entry of $\mathbb{0}'$ is replaced by the trace of $\hat{\rho}$, i. e. the number one. This keeps the information content unchanged, but makes the new equation solvable. The function ststi8.m

calculates the steady state using this trick. It is about two times faster than the corresponding function using SVD, but is fruitful only if the steady state is unique, otherwise it will give an error message. In case of success stst18.m gives the steady state of the ion as an 18 × 18-density matrix.

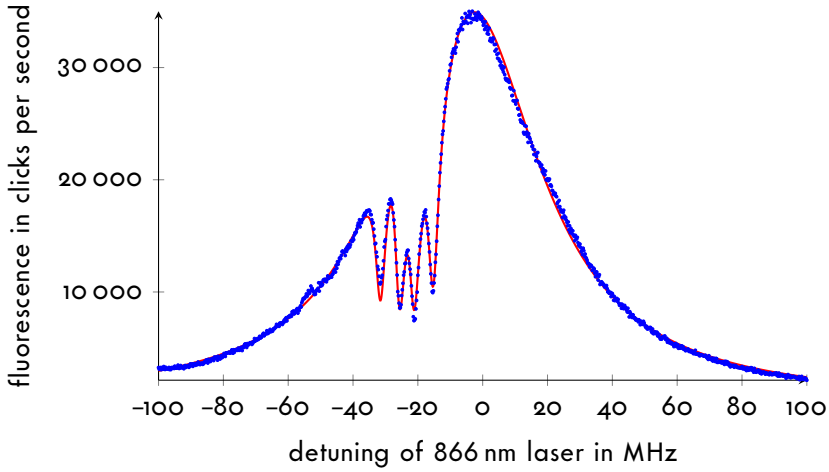

Figure 4.2 – Fluorescence spectrum of $^{40}Ca^{+}$ at the $P_{1/2}$–$D_{3/2}$ transition: The dots are measured data, the line is calculated with stst18.m using the parameters $\Omega_{397} = 24.5\,\text{MHz}$, $\Omega_{866} = 11\,\text{MHz}$, $\Delta_{397} = -17.4\,\text{MHz}$ and $\Delta\omega_{397} = \Delta\omega_{866} = 150\,\text{kHz}$. Four dark resonances are clearly visible.

As an example, figure 4.2 shows a spectroscopy at 866 nm wavelength of a single $^{40}Ca^{+}$ ion during the cooling cycle. Each data point is the number of fluorescence clicks detected in 500 ms at the respective detuning value of the 866 nm laser. The fluorescence rate is directly proportional to the population of the excited state $P_{1/2}$, which is calculated with Matlab and compared. By varying the model parameters globally and calculating the steady state for each point using the function stst18.m, the optimal parameters are found. This can be done manually or by a regression analysis. Here, the RABI frequencies of both lasers, and the detuning of the 397 nm laser are varied manually. All other parameters are kept fixed, the laser linewidths are determined by earlier measurements of laser specification (see sec. 1.4.5), and the angles are given through the experimental set-up.
The model does not only depict the general atomic resonance curve, but explains the four narrow dips as dark resonances that are associated to transitions between certain ZEEMAN sub-levels.

4.3.2 Simulation of dynamics

The time evolution of the density operator (in row-vector form) is given by, $\boldsymbol{\rho}'(t) = e^{\hat{\mathcal{L}}t}\boldsymbol{\rho}'(0)$, see section 4.1. To simulate dynamical behaviour in $^{40}Ca^{+}$ the density matrices for a number s of steps in time with the step size Δt are calculated using a given LIOUVILLE operator $\hat{\mathcal{L}}$ defined by LASER and Mag. There are two functions conducting this:
→ **dyn18init.m** starts the simulation from an initial state ρ_0:

obj = dyn18init(ρ_0, s, Δt, LASER, Mag)

→ **dyn18_steps.m** starts the simulation from the last density matrix of a previously calculated «obj»:

obj = dyn18_steps(obj, s, Δt, LASER, Mag)

The «obj» is a big matrix of the calculated data. It has one row per time step with the time values in the first column and the density matrices as 324-dimensional row vectors in the other columns.
The dynamics in the case of a time-dependent LIOUVILLE operator are simulated by approximating it with a stepwise-changing operator and using a sequence of several calls of dyn18_steps.m, one for each step. This allows for the analysis of arbitrary complex dynamics. To show the power of this modelling method, the example of a rather complex wave packet of a RAMAN photon at 393 nm is analysed in the following:
A single $^{40}Ca^{+}$ ion is initially prepared in $D_{5/2}$ in a pure state, the ZEEMAN sublevel with $m_J = +5/2$ (state no. 18 in figure 4.1), and then excited by an 854 nm laser beam. For details to the state preparation see [61]. The driven Λ-shaped transition $D_{5/2}$–$P_{3/2}$–$S_{1/2}$ results in the emission of a RAMAN photon of 393 nm wavelength. A laser power of 3.1 μW tightly focused by a HALO corresponds to a RABI frequency higher than the decay rate of the excited level $P_{3/2}$. This leads to RABI oscillations between the $D_{5/2}$ and $P_{3/2}$ level, visible as a modulation of the exponential decay. The detection of this photon with a time resolution of 0.4 ns in 33 562 runs of the experiment leads to the arrival-time distribution shown in figure 4.3 as a histogram of blue dots. These data were recorded on 5. 3. 2012 (lab book 6, p. 30) and published in [61] for the first time, but only now a quantitative explanation is given.
A single call of dyn18init.m can simulate the oscillating decay of the wave packet, but not the shape of its initial rise (from about 20 to 33 ns in the plot). As the strong excitation leads to a very short wave packet, the switching behaviour of the

AOM that directs the laser beam to the ion becomes relevant. This is simulated as a temporal step function of increasing RABI frequency over a switching time τ, thus a sequence of dyn18_steps.m. Assuming a GAUSSian beam profile, the intensity at the ion increases as the integral of the GAUSS curve with the switching time as standard deviation. The step function approximates the course of this function by 21 equidistant steps over a time span of 2τ where the integral increases from 0.02 to 0.98. Thus, the relative intensity increases from 0.2 to 0.8 over a time span of τ.

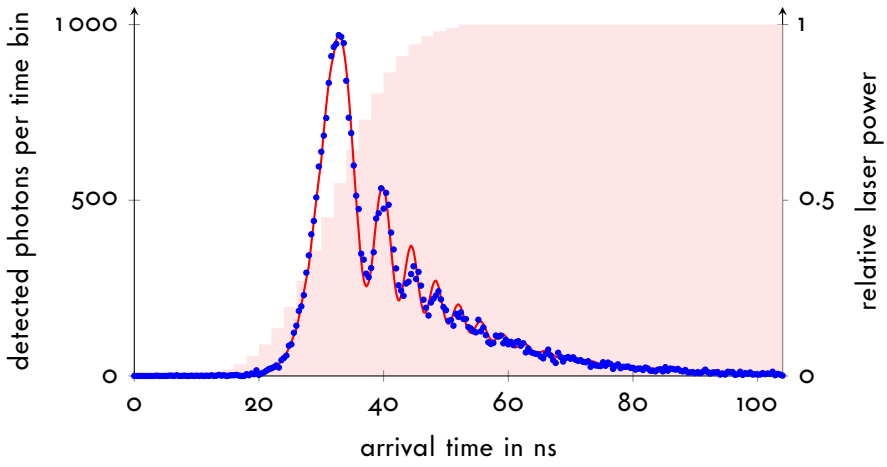

Figure 4.3 – Wave packet of a 393 nm RAMAN photon generated by high-intensity laser light at 854 nm wavelength. The blue dots form a histogram of 33 562 successful repetitions of the experiment with a binning of 0.4 ns. The red line is the simulation fitted to the measurement; the light-red area indicates the relative power of the exciting laser, see main text.

Using this sequence to simulate the dynamics in a standard χ-squared fitting routine gives the RABI frequency, detuning, and linewidth of the laser to be $\Omega = 350$ MHz, $\Delta = -5$ MHz, and $\Delta\omega = 15.6$ MHz, as well as the switching time of the AOM, $\tau = 22$ ns. The line in figure 4.3 corresponds to these values, and shows a good agreement with the data and the actual experimental parameters. The only conspicuous value is the fitted laser linewidth $\Delta\omega$, which is two orders of magnitude bigger than the measured linewidth of about 150 kHz (see section 1.4.5). This is attributed to other sources of incoherence in the measurement, e. g. the temporal spread of the electric signal in the photon detectors, and the fluctuation of the magnetic field.

4.3.3 Summary of the Matlab functions

The following summarises the provided functions and may serve as a reference guide for users of the programme.

→ **Liou18.m** calculates the Liouville superoperator $\hat{\mathcal{L}}$:

L = Liou18(LASER, Mag)

→ **dyn18init.m** calculates the dynamics for $\hat{\mathcal{L}}$ starting in a pure state (n = 1–18), a mixed orbital state (n = 's', 'p', 'd', 'P' or 'D'), or any given state (full 18×18 density matrix n):

obj = dyn18init(n, steps, Δt, LASER, Mag)

This is a generalised version of the following function.

→ **dyn18_init.m** calculates the dynamics for $\hat{\mathcal{L}}$ starting in the state $|1\rangle = |S_{1/2}, -1/2\rangle$:

obj = dyn18_init(steps, Δt, LASER, Mag)

→ **dyn18_steps.m** calculates the dynamics for $\hat{\mathcal{L}}$, continuing from a given «obj»:

obj = dyn18_steps(obj, steps, Δt, LASER, Mag)

→ **stst18.m** calculates the steady state of $\hat{\mathcal{L}}$:

rho = stst18(LASER, Mag)

→ **script18stst.m** runs «stst18» multiple times (with different values for one of the laser parameters):

obj = script18stst(LASER, Mag, laser no., laser pmt, interval)

→ **plot18.m** plots the population of one state (n = 1–18) or one orbital (n = 's', 'p', 'd', 'P' or 'D') of an «obj»:

plot18(obj, n)

→ **laststate.m** extracts the density matrix of the last state out of an «obj»:

rho = laststate(obj)

→ **plotstate.m** plots the absolute values of rho as a fancy 3D bar diagramme:

plotstate(rho)

→ **entropy.m** calculates the relative entropy S (scaled to the interval $[0, 1]$) of a

state rho or of all states in an «obj»:

S = entropy(rho or obj)

→ **purity.m** calculates the relative purity r ($\neq P = \mathrm{tr}(\rho^2)$, but scaled to the interval $[0, 1]$) of a state rho or of all states in «obj»:

r = purity(rho or obj)

As the simple purity $\mathrm{tr}(\hat{\rho}^2)$ of a density matrix is a non-intuitive physical quantity, a «more intuitive» one, the relative purity r, ranging from 0 to 1, is used here. It derives from the comparison of the (arbitrary) density matrix $\hat{\rho}$ with the weighted sum

$$\hat{\rho}' = (1 - r)\frac{\mathbb{1}}{d} + r|\psi\rangle\langle\psi|$$

of a total mixture and a pure state such that $\mathrm{tr}(\hat{\rho}'^2) = \mathrm{tr}(\hat{\rho}^2)$. Herein, $\mathbb{1}$ denotes the unity matrix, d the dimension of the HILBERT space (here $d = 18$), and $|\psi\rangle$ the unknown pure part that is not necessarily unique. Thus, the relative purity is given by

$$r = \sqrt{\frac{d \cdot \mathrm{tr}(\hat{\rho}^2) - 1}{d - 1}}\,.$$

In the case of a single q-bit ($d = 2$) the relative purity r coincides with the length $|\boldsymbol{r}|$ of the BLOCH vector as introduced in section 1.1 on p. 7. For a maximally entangled state $|\psi\rangle$, the density matrix $\hat{\rho}'$ is a WERNER state [132].

Chapter 5

The atom–photon quantum interface

«At any rate, it seems that the laws of physics present no barrier to reducing the size of computers until bits are the size of atoms, and quantum behavior holds dominant sway.»

— R. P. Feynman (1986)[32]

This chapter presents the quantum interface implemented by our research group over the recent years. It gives a general description of the interface and completes the published material [62–64, 80]. As a fundamental building block, the interface makes use of a single calcium-40 ion as the memory for a single q-bit, i. e. a node of a quantum communication network. Via spontaneous Raman scattering the ion is interfaced with single photons, acting as channels for quantum information. Therefore, the polarisation state of the participating single photons acts as the flying q-bit whereas the orientation of the atomic magnetic moment represents the stationary q-bit.

At first, the different modes of operation are introduced in section 5.1, and the roles they play in a quantum-network node are explained. In the subsequent section (sec. 5.2) based on [80], the necessary atom-physical principles are discussed in detail, which lead to different possible schemes how to implement the quantum interface. In the end, these are compared with each other. The last section (sec. 5.3) compiles some experimental realisations implemented by the research group [59, 60, 62–64].

5.1 Modes of operation

On the long route to quantum networking several experiments were carried out to show the implementation and versatility of the quantum interface based on a single calcium ion and photons at wavelengths of 854 nm and 393 nm. Four essentially different modes of operation of the interface were put into practice: receiver, sender, entangler, and converter mode.
All modes of operation are based on the same principle: The ion is prepared in a pure state in the $D_{5/2}$ manifold, labelled ψ_D, ready to absorb a photon at 854 nm wavelength in a certain polarisation state, ψ_{854}. Such an absorption initiates the emission of a single spontaneous RAMAN photon at 393 nm in a polarisation state labelled ψ_{393}. The ion is thus left in the $S_{1/2}$ manifold in the state labelled ψ_S. The treatment of the initial and final states of photon and atom sets the mode of operation. In the following each mode of operation is outlined separately; all four are summarised in table 5.1.

Table 5.1 – Overview of the four modes of operation of the quantum interface. Each of the four participating quantum properties play a different role depending on the mode. Some being input and output while others are fixed or projected to a certain state.

operation mode	ψ_{854}	ψ_D	ψ_S	ψ_{393}
receiver [62, 64]	**input**	fixed	**output**	projected
sender [63]	fixed	**input**	projected	**output**
entangler [62, 63]	fixed	fixed	**output**	
converter	**input**	fixed	projected	**output**

5.1.1 The receiver mode

The receiver or storage mode is a possibility to transfer a q-bit of information from a single photon at 854 nm to a $^{40}Ca^{+}$ ion. To do so, the quantum node has to be prepared initially in a fixed state, i. e. a certain well-known and pure state ψ_D. In particular, such a state is a balanced superposition of two states sensitive to two orthogonal polarisation states, and thus leading to a superposition of two individual RAMAN scattering processes. After this scattering the RAMAN photon needs to be projected to a fixed basis, and its arrival time measured with respect to the initialisation time of the ion.
In the case of success, heralded by the RAMAN photon, the q-bit is stored in the $S_{1/2}$ manifold preserving the superposition except for a phase shift due to

the frequency difference of the LARMOR precessions between ψ_D and ψ_S. The projection of the herald, both in polarisation and time, gives the exact value of this phase.
The whole process leaves the stored q-bit untouched, revealing no information that might be therein.

5.1.2 The sender mode

The opposite of the above-mentioned is the read-out of the ion's state, i. e. the ion acts as a sender of quantum information.
In this mode, a q-bit is initially stored in the ion as a potentially unknown state ψ_D. Then, the ion is excited by laser light at 854 nm wavelength with a known fixed polarisation ψ_{854}. This induces the RAMAN-scattering process with near unity probability bringing the ion into the $S_{1/2}$ manifold. A final projective measurement of the ion's state erases the sprouted entanglement, and the emitted 393 nm photon carries away the q-bit as its polarisation state.
Not every scheme presented in section 5.2 may serve the sender mode; a initial superposition state to carry the q-bit is needed.

5.1.3 The entangler mode

It is also possible to use the interface as a source of atom–photon entanglement.
This mode is the same as the sender mode except for the final, projective measurement of the $S_{1/2}$ manifold. For this mode one has more freedom in the choice of the initial atomic state ψ_D as it does not need to carry any quantum information. But the state must be known if the entanglement is created only between these two final q-bits.
The generation of entanglement of this kind is a natural consequence of a conservation principle, in this case, the conservation of total angular momentum.

5.1.4 The converter mode

The fourth mode of operation is the frequency conversion of a single photon under conservation of its polarisation state.
In this case, the initial state of the ion is fixed, and its final state is projected to a fixed basis. This combination transfers the q-bit state of the absorbed photon at 854 nm wavelength to the RAMAN photon at 393 nm. As with the other operations, a potential phase shift of π is induced depending on the result of the projection of ψ_S. As this phase shift is known, it can be incorporated in any subsequent processing.

5.2 Schemes of Implementation

This section is an updated and extended version of the publication:

> P. Müller & J. Eschner «Single calcium-40 ion as quantum memory for photon polarization: a case study» in *Appl. Phys. B* **114** (2014), 303, i. e. [80], see arXiv:1309.7863

To use a single atom and single photons as fundamental building blocks of a quantum communication network, their interaction has to be well controlled, and the mapping of the quantum states from one medium to the other one has to preserve the coherence and purity of each state. To fulfil these requirements, spontaneous Raman scattering of single photons is chosen for each elementary process of quantum information transfer.
Each single-photon Raman-scattering process consists of three participants, the incoming/absorbed photon, the atom and the outgoing/emitted photon. The crux is, that one of them carries the information initially and another one carries it after the process, while the third one serves as a herald of the whole process. This herald tells the experimenters, if and when the process took place, but it does not reveal the quantum information that has been processed. In addition, only the successful cases, defined by the heralding, are evaluated in the post-processing, and thereby the fidelity of the process is increased close to unity despite the low efficiency of the Raman scattering.

5.2.1 The choice of calcium

In our experiments the Raman transition $D_{5/2}$–$P_{3/2}$–$S_{1/2}$ in $^{40}Ca^{+}$ was mainly chosen because of the branching ratio (see fig. 1.2 on p. 11). An initial state in $D_{5/2}$ excited by light of 854 nm wavelength will end up in a final state in $S_{1/2}$ by emission of a single photon at 393 nm with preferably less additional scattering in between. In $^{40}Ca^{+}$ this is possible with a high probability of about 93.5 %. The additional scattering is the main source of impurity of the interface. On the other hand, a Raman transition with an extremer, more unbalanced branching ratio demands a stronger excitation, or will lead to a lower efficiency.
In the same way, the transition $D_{3/2}$–$P_{1/2}$–$S_{1/2}$ with the wavelengths of 866 nm and 397 nm could be used, but in our set-up these levels are already used for the cooling cycle and for fluorescence detection. In addition due to the lower total angular momenta, 3/2 and 1/2 instead of 5/2 and 3/2, respectively, the interface would be less versatile due to the lower number of possible schemes.
Here, in opposition to the earlier publications [63, 80, 113], the nomenclature for

polarisation states of section 1.1 is used, recapitulating the general polarisation state of eq. (1.3) on p. 10,

$$|\theta,\phi\rangle = \underbrace{e^{-i\frac{\phi}{2}}\cos\frac{\theta}{2}}_{=:p_+}|R\rangle + \underbrace{e^{+i\frac{\phi}{2}}\sin\frac{\theta}{2}}_{=:p_-}|L\rangle. \tag{5.1}$$

The variables θ, ϕ, and $p_\pm$ are used to characterise the polarisation state of the incoming light as a possible q-bit. In the same manner the polarisation state of the emitted photon is denoted by θ', ϕ', and $p'_\pm$, just adding a prime. The same general form is also used to describe an atomic q-bit state, but the basis is of course a different one, see for example eq. (5.3) below for the final atomic superposition in the $S_{1/2}$ manifold.

In general, the procedure starts with the preparation of the ion in a certain pure state $|\psi_D\rangle = \sum c_{m_D}|D_{5/2}, m_D\rangle$ in the $D_{5/2}$ multiplet. Then, light at the wavelength of 854 nm is shone onto the ion. Depending on the mode of operation, this is either laser light or a single photon. In any case, its polarisation state $|\theta,\phi\rangle$, given by eq. (1.3), translates into the atomic transitions depending on the angle α between the propagation direction $\boldsymbol{k}$ of the 854 nm beam and the quantisation axis of the ion defined by the external magnetic field $\boldsymbol{B}$. This resembles a rotation of the coordinate system about the angle α out of the z-direction. It is conveyed by the unitary transformation

$$\begin{aligned}\hat{P}_\alpha = {} & |{+1}\rangle\left(\cos^2\frac{\alpha}{2}\langle R| - \sin^2\frac{\alpha}{2}\langle L|\right) \\ & + |{-1}\rangle\left(\cos^2\frac{\alpha}{2}\langle L| - \sin^2\frac{\alpha}{2}\langle R|\right) \\ & - \frac{\sin\alpha}{\sqrt{2}}|0\rangle\left(\langle R| + \langle L|\right)\end{aligned}$$

onto the atomic transitions $|0\rangle$ and $|\pm1\rangle$ labelled by the change in the magnetic quantum number of the ion, $m_{854} = m_P - m_D$, thus corresponding to the π- and $\sigma^\pm$-channels of the $D_{5/2}$–$P_{3/2}$ transition, respectively.

The RAMAN operator of chapter 3 (see eq. (3.13) on p. 60 for details) is used to express each single spontaneous RAMAN process at the sub-channels of the transition $D_{5/2}$–$P_{3/2}$–$S_{1/2}$. For this purpose it is extended by the angular-momentum states of the two light fields and the three atomic levels. These states are determined by their respective magnetic quantum numbers, m_{854}, m_{393}, m_D, m_P, and m_S. Thus, the resulting RAMAN operator is

$$\hat{R}_{m_D,m_P,m_S}(\omega_{854}) = |S_{1/2}, m_S\rangle\big|R_{\omega_{393},\Gamma,\Delta_{854}};m_{393}\big\rangle\langle D_{5/2}, m_D|\langle\omega_{854};m_{854}|.$$

Herein $\Delta_{854} = \omega_{854} - \omega_P + \omega_D - (m_P g_P - m_D g_D)\zeta$ denotes the detuning of the incident light from the atomic absorption transition, $\omega_{393} = \omega_P - \omega_S + (m_P g_P - m_S g_S)\zeta$ the centre frequency of the emission transition (both using the abbreviation $\zeta = \mu_B B/\hbar$ for the ZEEMAN factor), and Γ is the decay constant of the $P_{3/2}$ state. To let this process happen, the two involved photonic spin states have to satisfy $m_{854} = m_P - m_D$ and $m_{393} = m_P - m_S$, in order to obey the conservation of angular momentum.
To model all possible transitions, the sum over all combinations of the three magnetic quantum numbers has to be performed:

$$\hat{R}(\omega_{854}) = \sum_{m_D=-5/2}^{+5/2} \sum_{m_P=-3/2}^{+3/2} \sum_{m_S=-1/2}^{+1/2} C^{(CG)}_{m_D, m_P} C^{(CG)}_{m_P, m_S} \hat{R}_{m_D, m_P, m_S}(\omega_{854}).$$

The weights account for the respective relative transition strengths, i. e. the CLEBSCH–GORDAN coefficients (cf. section 2.3.1 on p. 33, and for $^{40}Ca^+$, see section A 3 on p. 117). This procedure transforms the initial state into a joint (and in general entangled) state of the ion in the $S_{1/2}$ manifold and the emitted 393 nm photon.
Furthermore, collecting this photon under the angle α' to the quantisation axis results in

$$\left|\psi_{\text{joint}}\right\rangle = \hat{P}^+_{\alpha'} \hat{R}(\omega_{854}) \left(|\psi_D\rangle \otimes \hat{P}_\alpha |\omega_{854}; \theta, \phi\rangle \right). \tag{5.2}$$

Again depending on the mode of operation, a final projection may complete the process, either of the atom to a certain superposition state

$$|\psi_S\rangle = \underbrace{e^{-i\frac{\phi_S}{2}} \cos\frac{\theta_S}{2}}_{=:s_+} |S_{1/2}, +\tfrac{1}{2}\rangle + \underbrace{e^{+i\frac{\phi_S}{2}} \sin\frac{\theta_S}{2}}_{=:s_-} |S_{1/2}, -\tfrac{1}{2}\rangle \tag{5.3}$$

or the photon to a certain polarisation state

$$|\theta', \phi'\rangle = \underbrace{e^{-i\frac{\phi'}{2}} \cos\frac{\theta'}{2}}_{=:p'_+} |R\rangle + \underbrace{e^{+i\frac{\phi'}{2}} \sin\frac{\theta'}{2}}_{=:p'_-} |L\rangle.$$

In the latter case, fast temporal detection (as by a bare photomultiplier or avalanche photodiode) projects the photon further, fixing its arrival time to a certain value t. With an uncertainty lower than the inverse bandwidth of the photon, the detection erases all spectral information, and the final atomic state, $|\psi_S(t)\rangle \sim \langle t; \theta', \phi' | \psi_{\text{joint}} \rangle$, depends only on the six angles θ, ϕ, α, α', θ', ϕ' and on the initial atomic state ψ_D.

The relative efficiency of the quantum interface is defined as the probability to detect the RAMAN photon at any time in relation to the maximal probability of a single RAMAN process[1]:

$$\varepsilon = \int_0^\infty \langle \psi_S(t) | \psi_S(t) \rangle \, \mathrm{d}t \cdot \frac{1}{\langle R_{\Delta_{854}} | R_{\Delta_{854}} \rangle}.$$

The different modes of operation as mentioned above are achieved by setting some of these parameters to fixed values. The remaining degrees of freedom may serve to maximise the efficiency of the process. In addition, the efficiency has to be independent of the parameters that indicate the input state of the corresponding mode (θ and ϕ, or c_{m_D}, resp., see table 5.1 on p. 80).
If the projection is done by a polariser (a WOLLASTON prism or a polarising beam splitter), the photon may leave the other possible output channel and is projected to the orthogonal state leaving the ion in the state orthogonal to ψ_S.

5.2.2 An exemplary calculation

Possible sets of the parameter values are found by choosing a certain initial state of the ion, ψ_D, and calculating with the other six parameters kept variable. The results of this calculation for the five schemes introduced in article [80] are presented in figure 5.1.
As a notable example the calculation that leads to scheme (a) is presented in detail because it is the one most frequently utilised in the laboratory. An arbitrary superposition of the two outermost ZEEMAN states is chosen as a starting point,

$$|\psi_D\rangle = \underbrace{e^{-i\frac{\phi_D}{2}} \cos\frac{\theta_D}{2}}_{=:d_+} |D_{5/2}, +5/2\rangle + \underbrace{e^{+i\frac{\phi_D}{2}} \sin\frac{\theta_D}{2}}_{=:d_-} |D_{5/2}, -5/2\rangle$$

with general, complex coefficients d_+ and d_-. Together with a general polarisation state of the input photon, $|\theta, \phi\rangle = p_+|R\rangle + p_-|L\rangle$, as mentioned above, this leads to a joint state of ion and RAMAN photon according to eq. (5.2),

$$|\psi_{\text{joint}}\rangle = \sum_{\pm} d_\pm \left(p_\mp \cos^2\left(\tfrac{\alpha}{2}\right) - p_\pm \sin^2\left(\tfrac{\alpha}{2}\right)\right) |S_{1/2}, \pm 1/2\rangle \otimes |R_{\omega_p - \omega_S \pm \zeta, \Delta_1 \pm \zeta}\rangle \left(\cos^2\left(\tfrac{\alpha'}{2}\right)|\pm 1\rangle - \sin^2\left(\tfrac{\alpha'}{2}\right)|\mp 1\rangle\right),$$

1) In this context, «maximised» concerns the optimal input and output polarisation, but keeps the detuning Δ_{854} fixed to the value used in the interface. Only in the case of excitation by a laser the normalisation factor equals unity: $\langle R_{\Delta_{854}} | R_{\Delta_{854}} \rangle = 1$.

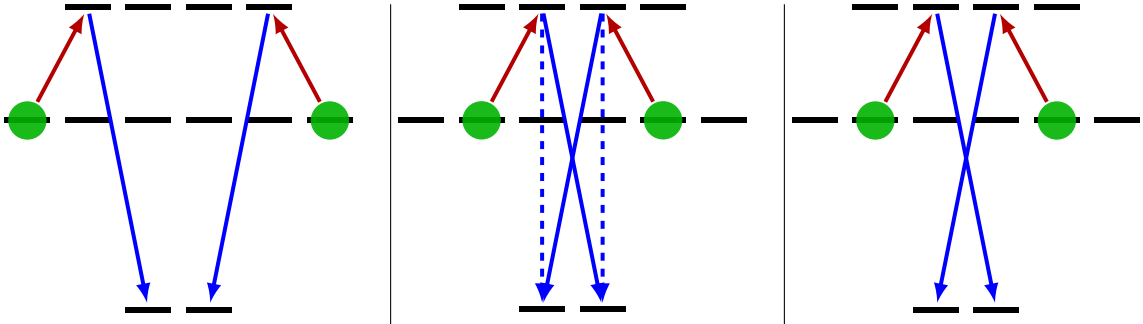

(**a**) $|\psi_D\rangle = d_-|-5/2\rangle + d_+|+5/2\rangle$
$\alpha = 0^\circ$, $\alpha' = 0^\circ$
receiver: $\theta_D = \frac{\pi}{2}$, $\theta' = \frac{\pi}{2}$
$|R\rangle \to |-1/2\rangle$
$|L\rangle \to |+1/2\rangle$
sender: $\theta = \frac{\pi}{2}$, $\theta_S = \frac{\pi}{2}$
$|+5/2\rangle \to |R\rangle$
$|-5/2\rangle \to |L\rangle$
$\varepsilon = 50\,\%$

(**b**) $|\psi_D\rangle = d_-|-3/2\rangle + d_+|+3/2\rangle$
$\alpha = 0^\circ$, $\alpha' = 90^\circ$
receiver: $\theta_D = \frac{\pi}{2}$, $\theta' = \frac{\pi}{2}$
$|R\rangle \to |\mp 1/2\rangle$
$|L\rangle \to |\pm 1/2\rangle$
sender: $\theta = \frac{\pi}{2}$, $\theta_S = \frac{\pi}{2}$
$|+3/2\rangle \to |R\rangle$
$|-3/2\rangle \to |L\rangle$
$\varepsilon = 25\,\%$

(**c**) $|\psi_D\rangle = d_-|-3/2\rangle + d_+|+3/2\rangle$
$\alpha = 0^\circ$, $\alpha' = 0^\circ$
receiver: $\theta_D = \frac{\pi}{2}$, $\theta' = \frac{\pi}{2}$
$|R\rangle \to |+1/2\rangle$
$|L\rangle \to |-1/2\rangle$
sender: $\theta = \frac{\pi}{2}$, $\theta_S = \frac{\pi}{2}$
$|+3/2\rangle \to |R\rangle$
$|-3/2\rangle \to |L\rangle$
$\varepsilon = 10\,\%$

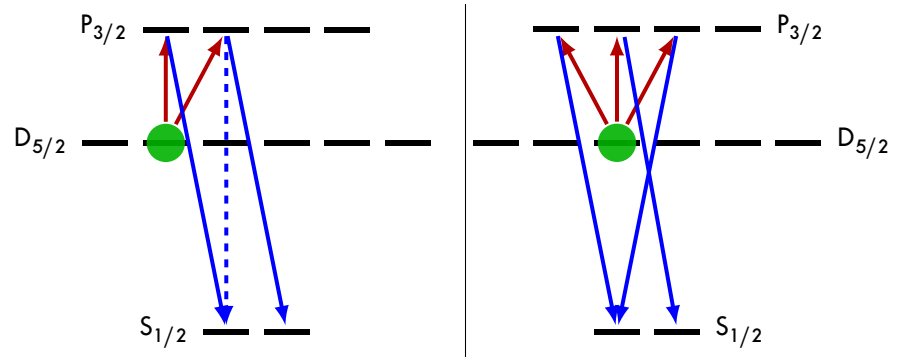

(**d**) $|\psi_D\rangle = |-3/2\rangle$
$\alpha = 47.06^\circ$, $\alpha' = 47.06^\circ$
receiver: $\theta' = 100.74^\circ$, $\phi' = 0^\circ$
$|R\rangle \to 0.98|+1/2\rangle - 0.19|-1/2\rangle$
$|L\rangle \to 0.19|+1/2\rangle + 0.98|-1/2\rangle$
$\varepsilon = 10.72\,\%$

(**e**) $|\psi_D\rangle = |-1/2\rangle$
$\alpha = 90^\circ$, $\alpha' = 90^\circ$
receiver: $\theta' = \frac{\pi}{2}$, $\phi' = \pi$
$|H\rangle \to |+1/2\rangle$
$|V\rangle \to |-1/2\rangle$
$\varepsilon = 10\,\%$

Figure 5.1 – Five possible schemes of implementation of the quantum interface. The pictures show the ZEEMAN manifolds of $P_{3/2}$, $D_{5/2}$, and $S_{1/2}$ with the prepared initial state ψ_D and the driven RAMAN transitions. The mappings are given for receiver and sender mode as well as the relative efficiency ε. All five schemes qualify as receiver and entangler, but (d) and (e) are obviously not suitable for the sender mode.

with $\Delta_1 = \omega_{854} - \omega_P + \omega_D$ being the detuning of the incident photon from the centre frequency of the absorption transition.
If the incident light is resonant with the absorption transition, $\Delta_1 = 0$, the wave packets of the two parts of the RAMAN photon, $R_\pm(t) = \langle t | R_{\omega_p - \omega_S \pm \zeta, \pm\zeta} \rangle$, have the same envelope and intensity, and differ only in their time-dependent phase (with a beat frequency ω_R), $R_\pm(t) = |R(t)|\, e^{\pm i\omega_R t/2}$. Thus, the starting point for the following application to the modes of operation is the joint state

$$|\psi_{\text{joint}}(t)\rangle = |R(t)| \sum_\pm e^{\pm\frac{i}{2}\omega_R t}\, d_\pm \left(p_\mp \cos^2\left(\tfrac{\alpha}{2}\right) - p_\pm \sin^2\left(\tfrac{\alpha}{2}\right)\right) |S_{1/2}, \pm\tfrac{1}{2}\rangle \otimes \left(\cos^2\left(\tfrac{\alpha'}{2}\right)|\pm 1\rangle - \sin^2\left(\tfrac{\alpha'}{2}\right)|\mp 1\rangle\right). \quad (5.4)$$

5.2.3 Application to the modes of operation

To get an entangled state, a balanced superposition is used for both initial states, i. e. $|d_\pm|^2 = \frac{1}{2} = |p_\pm|^2$. Thus, eq. (5.4) leads to

$$|\psi_{\text{joint}}(t)\rangle = \frac{|R(t)|}{2} \sum_\pm e^{\pm\frac{i}{2}(\omega_R t - \phi_D)} \left(\cos\tfrac{\phi}{2} \cos\alpha \pm i \sin\tfrac{\phi}{2}\right) |S_{1/2}, \pm\tfrac{1}{2}\rangle \otimes \left(\cos^2\left(\tfrac{\alpha'}{2}\right)|\pm 1\rangle - \sin^2\left(\tfrac{\alpha'}{2}\right)|\mp 1\rangle\right),$$

which is already a good candidate for the **entangler** mode. The relative efficiency is

$$\varepsilon = \frac{1}{4}\left(\cos^2\left(\tfrac{\phi}{2}\right)\cos^2\alpha + \sin^2\left(\tfrac{\phi}{2}\right)\right)\left(1 + \cos^2\alpha'\right)$$

and maximises to ½ for $\alpha' = 0°$ and $\alpha = 0°$ (on axis) or $\phi = 180°$ (vertical polarisation). In the experimental set-up $\alpha = \alpha' = 0°$ is chosen for maximal coupling efficiency leading to the BELL state

$$|\psi_{\text{joint}}(t)\rangle = \frac{|R(t)|}{2} \sum_\pm e^{\pm\frac{i}{2}(\omega_R t - \phi_D + \phi)} |S_{1/2}, \pm\tfrac{1}{2}\rangle \otimes |\pm 1\rangle = \frac{|R(t)|}{\sqrt{2}} |\Phi_{\phi_B(t)}\rangle$$

with the phase $\phi_B(t) = \omega_R t - \phi_D + \phi$ depending on the arrival time of the 393 nm photon.
For the **receiver** mode, the emitted photon is projected to a certain polarisation state reducing eq. (5.4) to the final atomic state

$$|\psi_S(t)\rangle = |R(t)| \sum_\pm e^{\pm\frac{i}{2}\omega_R t}\, d_\pm \left(p_\mp \cos^2\left(\tfrac{\alpha}{2}\right) - p_\pm \sin^2\left(\tfrac{\alpha}{2}\right)\right) \cdot \left(p'_\pm \cos^2\left(\tfrac{\alpha'}{2}\right) - p'_\mp \sin^2\left(\tfrac{\alpha'}{2}\right)\right) |S_{1/2}, \pm\tfrac{1}{2}\rangle.$$

If both the initial atomic state is set to a fixed balanced superposition, $|d_\pm|^2 = \frac{1}{2}$, and the emitted photon projected to a balanced superposition, i. e. a linear polarisation ($\theta' = \frac{\pi}{2}$), the ion is afterwards left in the state

$$|\psi_S(t)\rangle = \frac{|R(t)|}{2} \sum_\pm e^{\pm\frac{i}{2}(\omega_R t+\phi_D)} \left(p_\mp \cos^2(\tfrac{\alpha}{2}) - p_\pm \sin^2(\tfrac{\alpha}{2})\right) \cdot (\cos\tfrac{\phi'}{2} \cos\alpha' \pm i \sin\tfrac{\phi'}{2})|S_{1/2}, \pm\tfrac{1}{2}\rangle.$$

Again, for coupling and collection on the quantisation axis, $\alpha = 0° = \alpha'$, the efficiency is maximal, here $\varepsilon = \frac{1}{4}$, and the final atomic state reads

$$|\psi_S(t)\rangle = \frac{1}{2} \sum_\pm \underbrace{e^{\pm\frac{i}{2}(\omega_R t+\phi_D+\phi')} p_\mp}_{=s_\pm} |S_{1/2}, \pm\tfrac{1}{2}\rangle.$$

This shows the direct mapping of the initial photonic q-bit given by $p_\pm$ onto the atomic one given by $s_\pm$ with an additional phase depending on the detection time of the herald. The angles on the Bloch sphere are accordingly transformed, $\phi_S(t) = -\phi - \phi' - \phi_D - \omega_R t$ and $\theta_S = \pi - \theta$. E.g. the two circular polarisations are stored in the ion as the corresponding energy eigenstates while a linear polarisation is stored as an equal superposition:

$$\begin{aligned}
|R\rangle &\to |S_{1/2}, -\tfrac{1}{2}\rangle \\
|L\rangle &\to |S_{1/2}, +\tfrac{1}{2}\rangle \\
|H\rangle &\to \tfrac{1}{\sqrt{2}}(e^{i\phi_S(t)}|S_{1/2}, +\tfrac{1}{2}\rangle + e^{-i\phi_S(t)}|S_{1/2}, -\tfrac{1}{2}\rangle)
\end{aligned}$$

Emitted photons that leave the other output of the projection lead to the same process except for a phase shift of π in ϕ'. Including this information in the following processes, both cases are usable, thus doubling the efficiency of the receiver to $\varepsilon = \frac{1}{2}$.

Similarly, in the case of **sender** or **converter**, the final state of the ion is projected to a certain balanced superposition, $|s_\pm|^2 = \frac{1}{2}$. Thus, reducing eq. (5.4) to the state of the emitted photon,

$$|\psi_{393}(t)\rangle = \frac{|R(t)|}{\sqrt{2}} \sum_\pm e^{\pm\frac{i}{2}(\omega_R t+\phi_S)} d_\pm \left(p_\mp \cos^2(\frac{\alpha}{2}) - p_\pm \sin^2(\frac{\alpha}{2})\right) \cdot \left(\cos^2(\frac{\alpha'}{2})|\pm 1\rangle - \sin^2(\frac{\alpha'}{2})|\mp 1\rangle\right).$$

For the sender mode, the initial polarisation is fixed and linear, $|p_\pm|^2 = \frac{1}{2}$, whereas for conversion, the initial state of the ion is a fixed and balanced superposition, $|d_\pm|^2 = \frac{1}{2}$. With $\alpha = 0° = \alpha'$, the final states are

$$|\psi_{393}(t)\rangle = \frac{|R(t)|}{2} \sum_\pm \underbrace{e^{\pm\frac{i}{2}(\omega_R t+\phi_S-\phi)} d_\pm}_{=p'_\pm} |\pm 1\rangle$$

for sender and

$$|\psi_{393}(t)\rangle = \frac{|R(t)|}{2} \sum_{\pm} \underbrace{e^{\pm\frac{i}{2}(\omega_R t+\phi_S+\phi_D)} p_{\pm}}_{=p'_{\pm}} |\pm 1\rangle$$

for converter, respectively, both with efficiency $\varepsilon = 1/4$.
This means for the sender mode, the BLOCH angles are $\phi'(t) = \phi_D + \phi - \phi_S - \omega_R t$ and $\theta' = \theta_D$, and thus the states $|D_{5/2}, \pm 5/2\rangle$ are mapped to the circular polarisations while equal superpositions are mapped to linear polarisations with an additional phase depending on the point in time when the photon is emitted:

$$|D_{5/2}, +5/2\rangle \to |R\rangle$$
$$|D_{5/2}, -5/2\rangle \to |L\rangle$$
$$\frac{1}{\sqrt{2}}(|D_{5/2}, +5/2\rangle + |D_{5/2}, +5/2\rangle) \to \frac{1}{\sqrt{2}}(e^{i\phi(t)}|R\rangle + e^{-i\phi(t)}|L\rangle)$$

On the other hand, the single-photon conversion from 854 nm to 393 nm is done with an additional transformation on the BLOCH sphere, $\phi' = \phi - \phi_S - \phi_D - \omega_R t$ and $\theta' = \theta$, i. e. just a time-dependent rotation of the equatorial plane.
Again, using both projection outcomes (here, of the atomic state) doubles the efficiency to $\varepsilon = 1/2$. This is the general maximum for all modes of operation that is owed to the average overlap of the arbitrary or random polarisation state with the arbitrary initial atomic state, i. e. only in one half of the cases the two states match for absorption. Under certain conditions even this limitation can be overcome by the use of entanglement of the initial states (ψ_{854} or ψ_D) with further quantum systems instead of fixed states as described in this chapter. The entanglement-swapping protocol proposed in [47, p. 27 ff.] uses this idea quite naturally. There, one photon of an entangled pair is stored in the ion by implementing the receiver mode in scheme (c). As a result the entanglement of the pair is transferred to the ion and the remaining partner photon. With a maximally entangled photon-pair state the efficiency of the interface will be doubled, but the additional q-bit brings further complexity to the overall set-up.

5.3 Experimental realisation

The realisation of individual modes of operation as done by the author and others is published in several articles and summarised in this section. For details see the theses of Christoph KURZ [62] for section 5.3.1 and 5.3.3, and Stephan KUCERA [59] for section 5.3.2.

5.3.1 Receiver mode with laser photons

The first implementation of the receiver mode was done using photons of a laser beam instead of proper single photons:

> C. Kurz, M. Schug, P. Eich, J. Huwer, P. Müller & J. Eschner «Experimental protocol for high-fidelity heralded photon-to-atom quantum state transfer» in *Nat. Commun.* **5** (2014), 5527.
> DOI: 10.1038/ncomms6527, i. e. [64]

It was achieved in scheme (b), see figure 5.1 (b) on p. 86. The data were recorded at 4. 11. 2013 (p. 89 f. in lab book 11). The received photon in this case is not a true single photon but taken from a laser beam at 854 nm wavelength. Thus, the stored q-bit state is accessible by analysis of the laser's polarisation state. This fact makes the set-up useless for actual quantum communication scenarios, but it still serves as a proof-of-principle experiment for the receiver mode.
The mapping of the laser's polarisation state to the atomic q-bit is verified by the analysis of the atomic state after the projection and detection of the 393 nm Raman photon. This is done for several different polarisation settings to achieve a full quantum process tomography. Linear polarisations drive both transitions equally strong leading to full interference in the emission. This is observable as oscillations in the arrival-time distribution of the 393 nm photon, if the atomic state is projected to a superposition basis. The polarisation angle is directly identified by the phase of the oscillation. To make it visible the wave packet is elongated over several periods of the oscillation through weak excitation. With 12 µW of laser power and a beam waist of 125 µm a Rabi frequency of about 9 MHz is reached.
Due to the possible backscattering from the excited state in $P_{3/2}$ to the initial state in $D_{5/2}$ the coherence is reduced over time. A short detection-time window for the Raman photon is chosen to overcome this drawback, at least partially. This means only the cases of photon detection up to a maximum arrival time are evaluated. Thus, a compromise between efficiency and fidelity was found: For a time window of 450 ns the detection efficiency is 0.438(2) %, and the process fidelity 95.0(2) %. The quantum process tomography for this case is visualised as a deformed Bloch sphere in figure 5.2.
The same measurement was done also in scheme (a), see p. 86 again. But due to the higher sensitivity of the prepared superposition state to magnetic field fluctuations the efficiency and fidelity are lower in this case. For details, see [62, p. 91 f.].
As mentioned above, this experiment is just a proof of principle as the stored

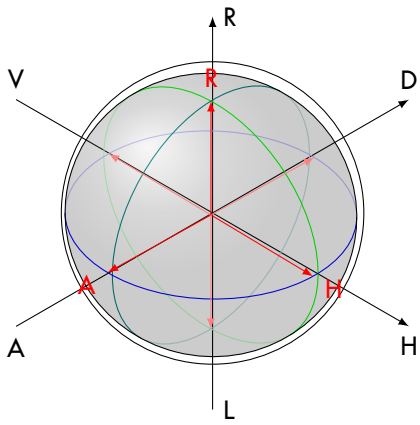

Figure 5.2 – Visualisation of the receiver mode with laser photons as a deformed BLOCH sphere according to section 1.1. The shown grey surface corresponds to the set of final states out of pure initial states, the red arrows indicate how the six basic states end up in this process.

photon is not a true single one, but one out of a laser beam. The next section shows how this flaw is overcome.

5.3.2 Receiver mode with single photons

The storage of single photons from an SPDC source has been implemented and will be published as a part of:

> S. KUCERA, J. ARENSKÖTTER, M. KREIS, P. EICH, P. MÜLLER & J. ESCHNER «Photon-photon to atom-photon entanglement transfer to a $^{40}Ca^{+}$ quantum node and state readout by teleportation», i. e. [60]

Using the SPDC source as characterised in [4] (see section 1.5 on p. 20) with a fibre-coupled photon rate of $2.5 \cdot 10^6/\mathrm{s}$, the receiver mode has been implemented in scheme (a), see figure 5.1 (a) on p. 86. With a repetition period of 558 µs including 56 µs exposure time of the photons to the prepared ion a process fidelity of $\chi_{00} = 89.9\,\%$ has been achieved. The main drawback in this measurement is owed to the source-sided detectors. A post-processed background correction resembling ideal detectors increases the value to 94.8 %. The complete quantum process tomography is visualised as a deformed BLOCH sphere in figure 5.3.
The fluctuations of the magnetic field that reduce the coherence of the superposition state during the exposure time are identified as the main drawback in this

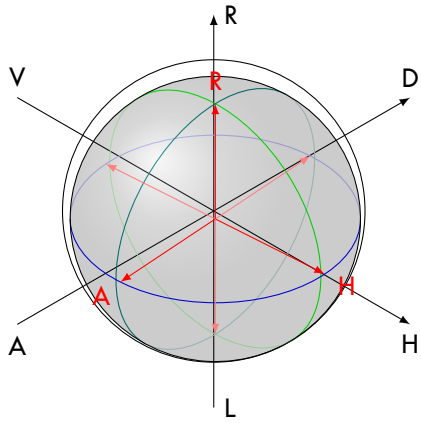

Figure 5.3 – Visualisation of the receiver mode with SPDC photons as a deformed BLOCH sphere according to section 1.1. The shown grey surface corresponds to the set of final states out of pure initial states, the red arrows indicate how the six basic states end up in this process.

set-up.[2] The reconstructed success probability for a fibre-coupled photon to be stored in the ion is $\eta_{\text{abs}} = 7.4 \cdot 10^{-4}$ in this experiment. This value is in agreement with previous absorption measurements [15, 66]. As the successful storage is heralded by a 393 nm photon the low success probability does not reduce the fidelity of the interface, only its speed. For more details, see [59, p. 81–92].

5.3.3 Sender and entangler mode

The implementation of sender and entangler mode was published for the first time as:

> C. KURZ, P. EICH, M. SCHUG, P. MÜLLER & J. ESCHNER «Programmable atom-photon quantum interface» in *Phys. Rev. A* **93** (2016), 62348. DOI: 10.1103/PhysRevA.93.062348, i. e. [63]

It is the implementation of scheme (a), see figure 5.1 (a) on p. 86, but with the 854 nm laser beam perpendicular to the quantisation axis, $\alpha = 90°$. This is irrelevant as it solely reduces the interaction strength of that laser with the ion. It has no influence on the protocol in sender or entangler mode, but the receiver mode is

2) Several measurements of the coherence times yield a range from 130 to 400 µs for the concerned superposition state in $D_{5/2}$.

impossible in this configuration.
The experiment was performed at 15. 2. 2015 (p. 15–17 in lab book 18). To prove and evaluate the quantum interface, the 393 nm photons are sent through a polarisation-analysis set-up consisting of a half- and a quarter-wave plate to project the polarisation onto different bases in consecutive measurements. In addition—in the case of sender mode—six different initial states are prepared in the ion, while in the case of entangler the final atomic state is projected to different bases.

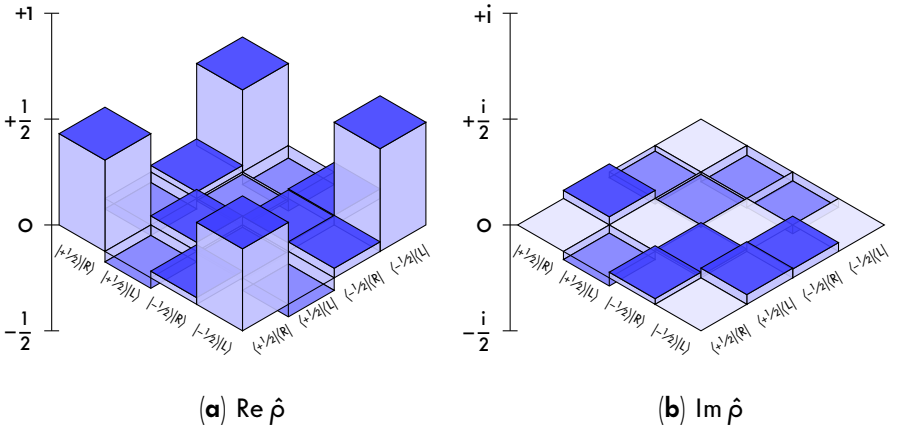

Figure 5.4 – Visualisation of the entangler mode. The left and right plot respectively display the real and imaginary part of the density matrix $\hat{\rho}$ of the joint atom–photon state.

Figure 5.4 shows the reconstructed density matrix of the joint atom–photon state. Its proximity to the maximally entangled state, $|\phi^+\rangle = \frac{1}{\sqrt{2}}(|+1/2\rangle|R\rangle + |-1/2\rangle|L\rangle)$, is clearly visible. Due to improper calibration of the wave plates the overlap fidelity of this state with respect to $|\phi^+\rangle$, is found to be $F = 84.6(2)\,\%$. This relatively low value lies still 89 standard deviations above the threshold of ⅔ for classical correlation, thus verifying the non-local entanglement of atom and photon. The corresponding concurrence or entanglement of formation [134] is 76.75 %.
For the sender mode the six polarisation states, R, L, H, V, D, and A, of the 393 nm photon are correlated with the six corresponding initial atomic states. From the evaluation of these 36 individual measurements the process fidelity for the sender is determined (and published) to be 90.2(1.0) % using the maximum-likelihood method [48]. If the improper calibration of the polarisation-analysis set-up is taken into account by disclosure of the actual polarisation in each of the six cases through Bayesian inference (sec. 6.5), and using these for the evaluation,

the process fidelity goes up to 94.0(1.5) %. This value is compatible with the expected maximum due to parasitic backscattering given by the branching fraction of 93.47(5) % (see sec. 1.2). The corresponding quantum process tomography is visualised as before as a deformed BLOCH sphere in figure 5.5.

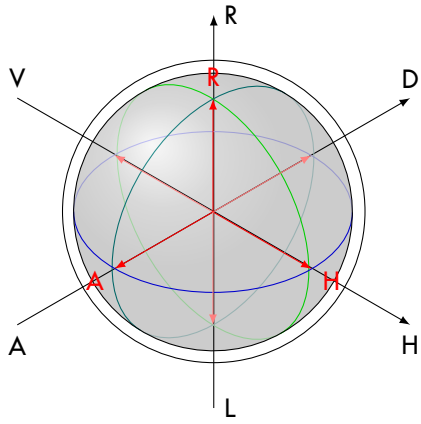

Figure 5.5 – Visualisation (as in fig. 5.2) of the sender mode as a deformed BLOCH sphere. The shown grey surface corresponds to the set of final states out of pure initial states, the red arrows indicate how the six basic states end up in this process.

5.4 Conclusion

This chapter has shown the implementation of a versatile, programmable, and bidirectional interface between single photons and ions as flying and stationary q-bits, respectively. It demonstrates the single $^{40}Ca^{+}$ ion in free space as a possible building block for quantum networking.
The general use of the RAMAN photon as a herald for the single transfer process enables high fidelities even though the efficiencies of absorption, emission, and collection of the photons are low. This makes it possible to use the quantum interface as the fundament for reliable quantum gates.

Chapter 6

Measurement of the scattering phase in a spontaneous Raman process

«Don't keep forever on the public road,
going only where others have gone.
Leave the beaten track behind occasionally
and ... You will be certain to find
something you have never seen before.»

— A. G. Bell (1847–1922)

This chapter anticipates the forthcoming publication of the same title:

> P. Müller, M. Kreis, P. Eich & J. Eschner «Measurement of the scattering phase in a spontaneous Raman process», i. e. [81]

By preparing a single ion in a superposition state and driving two equally strong Raman transitions, a single photon is scattered that embodies the interference of the two transitions. Its phase was measured to reveal the phase difference of the two corresponding complex absorption profiles. The results are in good agreement with numerical simulations. The details of the applied model of spontaneous Raman scattering is presented in chapter 3.

6.1 Experimental set-up

For the experimental realisation a singly ionised calcium-40 ion trapped in a linear Paul trap is used (see figure 6.1). The experimental protocol for heralded photon-to-atom state transfer as published in [64] is implemented, i. e. the receiver mode of the quantum interface as presented in section 5.3.1 on p. 90, using laser photons

at 854 nm wavelength. The $^{40}Ca^{+}$ ion is excited by beams of various frequency-stabilised diode lasers. It is Doppler cooled on the $S_{1/2}$–$P_{1/2}$ transition using a laser at 397 nm while a laser at 866 nm repumps the population from the metastable $D_{5/2}$ level (see figure 1.2 on p. 11).

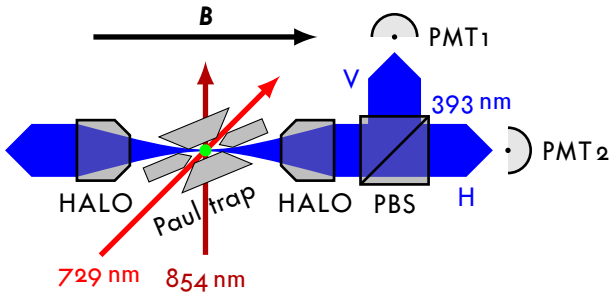

Figure 6.1 – Sketch of the experimental set-up. The calcium ion (green dot) at the centre of the PAUL trap emits blue photons at 393 nm wavelength. Those that are collected by one of the HALOs, are analysed by a PBS and detected by two PMTs.

A static magnetic field of flux density $|\boldsymbol{B}| = 284.195(6)\,\mu T$ defines the quantisation axis and lifts the degeneracy of the atomic levels due to ZEEMAN splitting. To drive the magnetic dipole transition in the $S_{1/2}$ manifold at $\omega_{L,S} = 7.9643(2)$ MHz, a radio-frequency signal (RF) is applied to a simple copper-wire coil underneath the trap's vacuum vessel. A narrowband laser at 729 nm drives the $S_{1/2}$–$D_{5/2}$ quadrupole transition, whereupon a single transition between two ZEEMAN sub-levels is selected by tuning the laser frequency. This enables us to coherently manipulate the internal state of the calcium ion, e. g. to prepare a superposition in the $D_{5/2}$ manifold by a set of laser pulses of certain duration and frequency. A laser at 854 nm drives the $D_{5/2}$–$P_{3/2}$ transition to release the single spontaneous RAMAN photon at 393 nm.
A high-numerical-aperture laser objective (HALO) [36] is used to collect the 393 nm photons emitted into 4.18 % of the solid angle (NA = 0.4) in direction of the quantisation axis. Thereafter, a polarising beam splitter (PBS) is used to separate the photons, enabling us to measure the polarisation state and arrival time through two photo-multiplying tubes (PMT), see figure 6.1.

6.2 Theoretical model

For the quantum-mechanical description of spontaneous RAMAN scattering, a three-level system of two stable states and one short-lived excited state is considered,

see figure 6.2. The respective levels in $^{40}Ca^{+}$ are the $S_{1/2}$, $D_{5/2}$, and $P_{3/2}$ fine structure manifolds, for details see figure 1.2 on p. 11. A laser field at 854 nm wavelength couples one of the stable states ($D_{5/2}$) to the excited state ($P_{3/2}$), tuned away from the resonance by a certain detuning Δ.

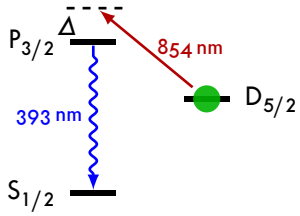

Figure 6.2 – The level scheme of the spontaneous RAMAN transition.

The theory of RAMAN scattering (see [82], or chapter 3 on p. 43 ff.) predicts the amplitude spectrum of the scattered photon at frequency ω to be a superposition (or product) of two complex LORENTZian lines,

$$R(\omega) = \sqrt{\frac{C}{2\pi}} \left(\frac{1}{\omega - \omega_E - \Delta - \Delta_S + i\frac{\kappa}{2}} - \frac{1}{\omega - \omega_E + \Delta_S + i\frac{\Gamma-\kappa}{2}} \right), \tag{3.12'}$$

with different linewidths and detunings from the natural frequency ω_E of the emission transition. The first term is the RAMAN peak that is narrowband ($\kappa < \Gamma$) and dominates the spectrum. It is detuned by Δ from the emission transition as the exciting laser is from the absorption transition. The minor part given by the other peak corresponds to the spontaneous emission at resonance. Additionally, both peaks are separated further by the AC STARK shift moving their line centres by $\pm\Delta_S$ from the ideal positions.
The FOURIER transformation of the spectrum is the temporal wave function of the photon,

$$R(t) = -i\sqrt{C}\,\Theta(t) \left(e^{-\frac{\kappa}{2}t - i(\omega_E + \Delta + \Delta_S)t} - e^{-\frac{\Gamma-\kappa}{2}t - i(\omega_E - \Delta_S)t} \right). \tag{3.11'}$$

A measurement of the arrival-time distribution or the power spectrum, i. e. the absolute squares $|R(\omega)|^2$ or $|R(t)|^2$, respectively, is easily done, but the phase of the wave packet, $\arg(R(t))$, is inaccessible without a suitable reference. Several experiments [2, 45, 97] were done using the exciting light as reference, i. e. the phase shift of the exciting laser beam induced by the scattering from a single atom or molecule was measured. A good theoretical treatment thereof is given in [118]. The largest phase shift measured in those experiments was 6°. Here,

the emitted photon itself is used as reference, which enables significantly higher values.
This is accomplished by preparing the ion in a symmetric superposition of the two outermost ZEEMAN sub-levels of the $D_{5/2}$ manifold (filled circles in fig. 6.3), and driving the two RAMAN transitions with the one and same laser. Thus, the ion ends up in the $S_{1/2}$ (empty circles) in a state entangled with the polarisation of the scattered 393 nm photon.

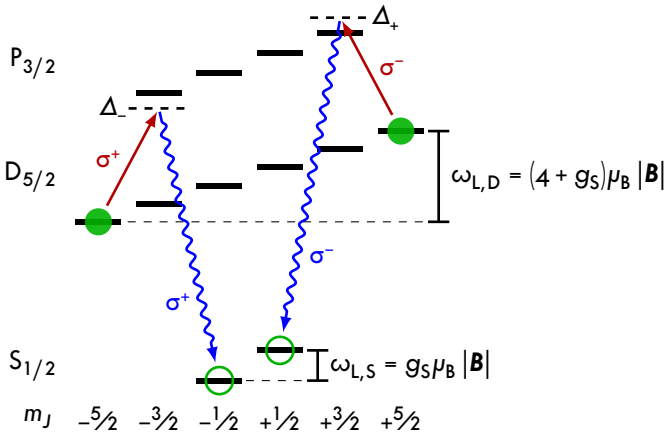

Figure 6.3 – Detailed level scheme showing the ZEEMAN-split states (as bars) with the magnetic quantum number m_J and the two RAMAN transitions (as arrows). The two red arrows indicate the excitation by the same laser.

Expressed in the nomenclature of chapter 3 this state reads,

$$|\psi\rangle = \frac{1}{\sqrt{2}} \left(\left|-\tfrac{1}{2}\right\rangle \otimes |R_-; \sigma^+\rangle + \left|+\tfrac{1}{2}\right\rangle \otimes |R_+; \sigma^-\rangle \right),$$

with the RAMAN modes $R_\pm$ (according to eq. (3.11)) for the two different detunings $\Delta_\pm$ due to the ZEEMAN splitting, and with the corresponding circular polarisations $\sigma^\mp$. The two final atomic states $|S_{1/2}, m_J = \pm\tfrac{1}{2}\rangle$ are abbreviated as $|\pm\tfrac{1}{2}\rangle$.
Measuring, i. e. projecting, the ion and the emitted photon in a respective basis of symmetric superpositions, and recording the photon's arrival time t leads to four combinations of outcomes, each showing the beating of the two RAMAN transitions. The chosen basis states are $|\pm\rangle = \frac{1}{\sqrt{2}}(|-\tfrac{1}{2}\rangle \pm |+\tfrac{1}{2}\rangle)$ for the ion and the linear polarisations, H and V, for the photon. With $|H\rangle = \frac{1}{\sqrt{2}}(|R\rangle + |L\rangle)$ and

$|V\rangle = \frac{-i}{\sqrt{2}}(|R\rangle - |L\rangle)$ the temporal probability distributions are

$$\begin{aligned} P_{\pm,H/V}(t) &= \left|(\langle\pm| \otimes \langle H/V; t|)|\psi\rangle\right|^2 \\ &= \frac{1}{8}\Theta(t)\left|\pm\sqrt{C_+}\left(e^{-\frac{\kappa_+}{2}t - i(\omega_+ + \Delta_+ + \Delta_{S,+})t} - e^{-\frac{\Gamma-\kappa_+}{2}t - i(\omega_+ - \Delta_{S,+})t}\right)\right. \\ &\qquad \left.\pm\sqrt{C_-}\left(e^{-\frac{\kappa_-}{2}t - i(\omega_- + \Delta_- + \Delta_{S,-})t} - e^{-\frac{\Gamma-\kappa_-}{2}t - i(\omega_- - \Delta_{S,-})t}\right)\right|^2 \end{aligned} \quad (6.3)$$

with the Zeeman-shifted transition frequencies and detunings, $\omega_\pm = \omega_E \pm \mu_B |\boldsymbol{B}|$ and $\Delta_\pm = \Delta \pm \mu_B |\boldsymbol{B}|$, respectively. The «±» sign in the second row of eq. (6.3) corresponds to the measured ionic state $|\pm\rangle$ while the «±» sign in the third row corresponds to the measured photonic state («+» for H, «–» for V). For low excitation power $\Omega \ll \Gamma$, the respective first terms in the parentheses are dominant, yielding the same beat frequency in all four cases, which is close to the difference between the Larmor frequencies of the initial and final superposition state, $\omega_L = \omega_{L,D} - \omega_{L,S} = 4\mu_B |\boldsymbol{B}|$ (see figure 6.3). The detuning Δ of the 854 nm laser causes tiny changes in the beating that result in small frequency and phase shifts in the wave packet. These are the key point of the experiment and become visible through the following high-precision measurement and analysis.

6.3 Experimental sequence

The experimental sequence is the following: After 100 µs of Doppler cooling, the ion is optically pumped to the pure state $|S_{1/2}, m_J = -1/2\rangle$ by driving the transition $|S_{1/2}, +1/2\rangle \leftrightarrow |D_{5/2}, -3/2\rangle$ with the narrowband laser at 729 nm while the 854 nm laser is switched on. After 60 µs the probability to find the ion in $|S_{1/2}, -1/2\rangle$ is 99.6(3) % [66]. Afterwards, three consecutive Rabi pulses prepare the initial superposition of the two outermost sub-levels of the $D_{5/2}$ manifold: An RF π/2-pulse (5 µs) creates a superposition in the $S_{1/2}$ followed by two 729 nm π-pulses (7 µs each) at different frequencies to transfer this state to the $D_{5/2}$. The phase relationship between these pulses has to be fixed to get a superposition, not a mixture. After the preparation, laser light at 854 nm is shone to the ion driving two possible transitions (red arrows in figure 6.3) and causing the scattering of a single 393 nm photon at some instance during the 20 µs of this pulse. In 4.18 % of all cases the photon is scattered into the HALO, and thus detected with a total probability of 1 %. Its arrival time is recorded with a resolution of 320 ps.
If a photon is detected, the measurement basis $\{|+\rangle, |-\rangle\}$ of the final atomic state is chosen by a second RF π/2-pulse. This completes the Ramsey interference [101] started by the first RF π/2-pulse. A final 729 nm π-pulse transfers the population

that is in $|S_{1/2}, -1/2\rangle$ to the now empty $|D_{5/2}, -5/2\rangle$ (electron shelving). Finally, the cooling is switched on again and fluorescence is detected if the ion is in $|S_{1/2}, +1/2\rangle$ (called bright state). If no fluorescence photon is detected after 100 µs, the ion is deemed to be in the $D_{5/2}$ (dark state).
Then, in any case, the 854 nm laser is switched on again to repump the dark ion into the cooling cycle and to start over the whole sequence. Every 5 000 repetitions of this sequence, the power levels of the 729 nm and 854 nm laser beams are stabilised by PID control loops. After 15 of these cycles (≈ 17 s), the resonance of the RF transition is measured, and the drift of the magnetic field is compensated.
The whole procedure is repeated for nine different frequency settings of the 854 nm excitation pulse, from −40 to +40 MHz detuned from the centre frequency. For every setting and for each of the four combinations of photonic state (H or V polarisation) and atomic state (bright or dark), the arrival times of the 393 nm photon with respect to the start of the excitation are compiled into a histogram. These 36 histograms or arrival-time distributions display nothing but different projections of the single photon's wave packet, eq. (3.9). As an example, one such histogram is shown in figure 6.4.

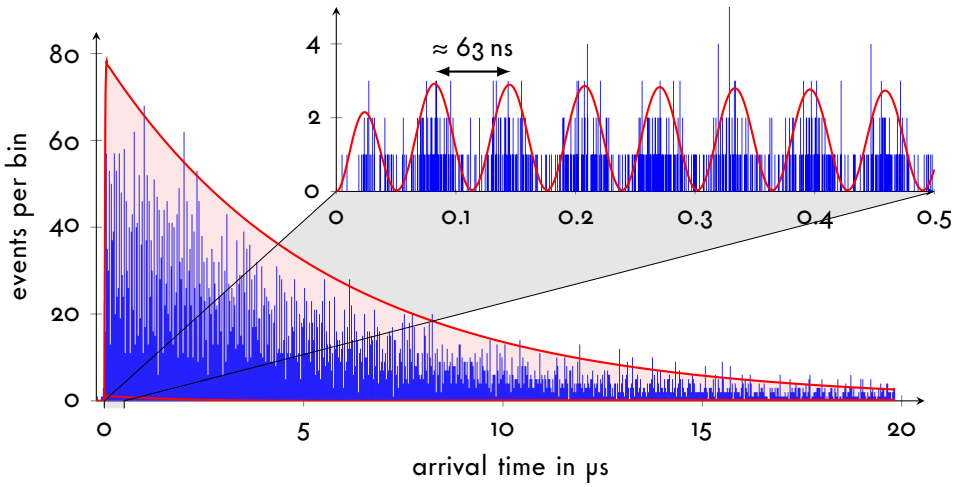

Figure 6.4 – Exemplary plot of an arrival-time distribution: for vertically polarised 393 nm photons conditioned to the dark state of the ion, measurement at +10 MHz detuning. The inset shows a zoom into raw time-tag data of 320 ps resolution, while the main plot shows the entire detection window binned to 25 ns intervals. Blue bars depict the measured data, the red line in the inset corresponds to the wave packet according to eq. (6.3) fitted to the data, and the red lines in the main diagram illustrate the envelope thereof.

As predicted by the model, a beating with an exponential envelope arises. The inset shows an oscillation period of about 63 ns, i. e. a beat frequency of about 16 MHz. Comparing the histograms for different frequency values of the 854 nm laser reveals the phase of the oscillation to shift forward and backward again when the detuning is varied over the centre of the two resonances.

6.4 Data analysis

Quantifying the small phase shift took a big effort as the methods of data analysis that the research group usually applies failed in this case, and a wholly new one had to be introduced.

The first and naïve approach was to directly apply the least-squares method (especially the χ^2 test) to fit a model function to the arrival-time distributions. A simple sine function, with and without an exponential envelope, as well as the detailed function of section 6.2 were tested. But all these have yielded no useful result due to the low number of counts (≈ 1 on average) per time tag of 320 ps. Increasing this number to an adequate level by binning several time tags together (as in the main plot of figure 6.4) leads to an extreme reduction of temporal resolution and contrast. This is owed to the information lost that accompanies the binning.

A second and intuitive approach was to convert the arrival-time histograms into phase histograms by modulo calculation of the time t with the beat period $T \approx 63$ ns, i. e. $\phi = 2\pi(t \bmod T)$. This would give sufficiently high count numbers per phase bin to fit a single sine period to the 2π-scope using the χ^2 test—a method used fruitfully in the past, e. g. [63, 64]. But here this method failed because the period T has to be known very accurately in advance, which was not given due to the fact that it also changes with the detuning of the laser.

Finally, the method of Bayesian inference [50] was studied and introduced by the author. It determines the probability distribution for the parameters of an assumed model to fit the data set. Even though its numerical effort is much larger than for the common methods, there are three main advantages: It is applicable to arbitrary low counting numbers with no need for binning; the probability distribution yields mean values and standard deviations for each model parameter directly, i. e. without additional considerations about uncertainties as in other regression analyses; and the tested models may even lack some of the features seen in the data, but give still good results for the considered parameters. The complete procedure is explained in the following section.

6.5 Bayesian inference

The empirical sciences are based on the interplay between observation and experiments on the one hand and modelling or theory formation on the other hand. Following Popper's idea of falsification [96] we assume every model to be false, and proved so at some time in the future. Thus, the question is not «if», but «how» false a certain model or hypothesis is; or in other words, how good the model supports the experimentally found data.
In recent times, a new method for hypothesis testing has been established and is applied more and more in many fields of science. It is called Bayesian inference due to the fact that it uses the theorem of Bayes as the central point of reasoning.
The underlying idea is to calculate first the probability $P(D|H)$ to find the data set D under the assumption of a hypothesis H. Then, by the application of Bayes' theorem of conditional probabilities [6, 50],

$$P(H|D) = \frac{P(D|H) \cdot P(H)}{P(D)}, \tag{6.4}$$

the constraining $D|H$ is reversed, leading to the probability $P(H|D)$ that the hypothesis suits to the measured data set. If this is done not only for one hypothesis, but for a set of hypotheses characterised by different values of one or more model parameters $\{m_1, m_2, \ldots\}$, then $P(H|D)$ itself is a function of hypotheses, or more precisely a probability distribution of the model parameters—a property that is often called likelihood or plausibility function. Expectation values for the parameters and their deviations can easily be calculated out of this, and taken as a «replacement» for the fitted parameters of frequentistic regressions like the maximum-likelihood estimation or the least-squares method.

6.5.1 Application to histograms

Here, Bayesian inference is applied to histogram data, where D is a set of integers n_i that count how often certain events E_i occurred. In this case hypotheses H are evaluated, which predict the probabilities $p_i(H)$ to get in a single run the event E_i. In the said experiment, the events E_i are the photon clicks detected in a corresponding time tag t_i. In the first place, the probabilities $p_i(H)$ are calculated in dependence on the model parameters $H = \{m_1, m_2, \ldots\}$. For the whole data set, this leads to a multinomial distribution,

$$P(D|H) = \frac{N!}{\prod_{i=1}^{k} n_i!} \prod_{i=1}^{k} (p_i(H))^{n_i},$$

wherein $N = \sum_{i=1}^{k} n_i$ is the total number of events in the total number of k time tags.

From this, the probability distribution $P(H|D)$ of the parameters is inferred through application of Bayes' theorem, eq. (6.4). In this calculation the probability $P(D)$ to find the data set D independent of any hypothesis is determined by the law of total probability, $P(D) = \sum_H P(D|H)\,P(H)$, with the so-called prior distribution $P(H)$. Its name «prior» is owed to the image of this function as the probability distribution expressing the knowledge of the experimenter «prior» to any measurement. Under the principle of maximum entropy [49], it is assumed constant (and of course normalised to unity). In this case, eq. (6.4) reduces to

$$P(H|D) = \frac{P(D|H)}{\sum_H P(D|H)} \sim \prod_{i=1}^{k} (p_i(H))^{n_i} =: f(H) \tag{6.5}$$

where $f(H)$ serves as a non-normalised distribution to find the mean values and standard deviations of the model parameters, $\langle m_i \rangle \pm \Delta m_i$, by integration over the whole parameter space, e. g.

$$\langle m_i \rangle = \frac{\int \cdots \int m_i f(H)\,\mathrm{d}m_1\,\mathrm{d}m_2 \ldots}{\int \cdots \int f(H)\,\mathrm{d}m_1\,\mathrm{d}m_2 \ldots}.$$

The advantage over the well-known χ^2 test is that it gives valid results even in the case of small numbers n_i (see the ordinate of the inset in fig. 6.4). Furthermore, the uncertainties (standard deviations Δm_i) are thrown in directly. This is an advantage over the maximum-likelihood method [1, 34] where the likelihood function $f(H)$ is just maximised, and the uncertainties have to be found through additional considerations, which are often not treated with the necessary care. Here, the whole distribution $f(H)$ is used to get mean values (instead of values at maximum) and their uncertainties directly.

The essence of this evaluation is that the estimated parameter values are computed directly out of the primary data, and all of this data is used at once—in particular without intermediate evaluation steps, grouping of data, or loss of information through binning and so on.

6.5.2 Numerical approximation

To use this method for a numerical mean-value estimation, every integral is replaced by a sum over a well-chosen interval around the mean value and with a discretisation far below the standard deviation.

For a high number of events (say $N > 1000$) the values of the total probability distributions (as eq. (6.5) for example) become very small, and may result in

rounding errors on a computing machine. In such cases, it is preferable to calculate the logarithms of the single probabilities p_i and normalise the logarithmic distribution,

$$L_H := \log f(H) = \sum_{i=1}^{k} n_i \log p_i(H) \leq 0,$$

to a maximum value of zero: Thus, using $\tilde{f}(H) := e^{L_H - \max L_H}$ instead of $f(H)$ leads to the same mean values and standard deviations, but prevents the rounding errors of small numbers.

6.5.3 The ψ-test

As a figure of merit for a hypothesis H the measure

$$\psi(H) := L_{\text{rf}} - L_H = \sum_{i=1}^{k} n_i \log\left(\frac{n_i}{N p_i(H)}\right) \geq 0 \tag{6.6}$$

is introduced. It discloses a comparison of the hypothesis H with the best possible, but usually unknown hypothesis H_{rf}, i.e. the one that would yield exactly the relative frequencies as single-event probabilities for all events, $p_i(H_{\text{rf}}) = \frac{n_i}{N}$. The ψ-value tells how far-off a hypothesis is from this ideal one since obviously $\psi(H_{\text{rf}}) = 0$.
To show the meaning of ψ quantitatively the following approximation is examined. In the case where the relative frequencies are close to the calculated probabilities, $\left|\frac{n_i}{N} - p_i\right| \ll p_i$, the Taylor expansion of $x \log x$ at $x = 1$ leads to an approximation of eq. (6.6)[1]:

$$\begin{aligned}
\psi(H) &= \sum_{i=1}^{k} N p_i(H) \frac{n_i}{N p_i(H)} \log\left(\frac{n_i}{N p_i(H)}\right) \\
&= \sum_{i=1}^{k} N p_i(H) \left(\frac{n_i}{N p_i(H)} - 1 + \frac{1}{2}\left(\frac{n_i}{N p_i(H)} - 1\right)^2\right) + \mathcal{O}\left(\frac{1}{\sqrt{N}}\right) \\
&= \underbrace{\sum_{i=1}^{k} n_i}_{=N} - N \underbrace{\sum_{i=1}^{k} p_i(H)}_{=1} + \frac{1}{2} \underbrace{\sum_{i=1}^{k} \frac{(n_i - N p_i(H))^2}{N p_i(H)}}_{= \chi^2|_{\sigma_i^2 = N p_i}} + \mathcal{O}\left(\frac{1}{\sqrt{N}}\right)
\end{aligned}$$

The lowest remaining order corresponds to the goodness of fit of the well-known χ^2-test [92] under the assumption that the frequencies n_i obey the Poissonian

1) In detail $x \log x = 0 + (x-1) + \frac{1}{2}(x-1)^2 + \mathcal{O}((x-1)^3)$.

distribution with the rate parameter Np_i ($= \langle n_i \rangle = \sigma_i^2$) [95]. This shows that the χ^2-value is just an approximation, only valid for large numbers n_i. For further details, see [50, p. 298 f.]. Thus, a good ψ-value is about $k/2$, or in other words (in comparison to the reduced χ^2-value) a reduced ψ-value defined by

$$\psi_{\text{red}}(H) = \frac{\psi(H)}{k/2}$$

indicates a good hypothesis if $\psi_{\text{red}}(H) \approx 1$.

6.6 Results

The BAYESian inference is applied to two different models for the arrival-time distributions of the measured RAMAN scattering process. The first one is a simple sine function used to find the phase and frequency shifts,

$$f(t|\omega, \phi) = \tfrac{1}{2} + \tfrac{1}{2} \sin(\omega t + \phi), \tag{6.7}$$

with the beat frequency ω and the phase ϕ as the only model parameters. It does not at all concern the envelope of the wave packet (cf. figure 6.4), which is possible in and a big advantage of BAYESian inference as mentioned above in section 6.4. The analysis is done separately for each detuning value, but for all four bases combinations in one run including correction for the 180° phase jump between the two pairs of combinations (H, bright and V, dark vs. H, dark and V, bright). The resulting phase and frequency shifts including their standard deviations are shown as nine points for each of three separate measurement series in figure 6.5 (a) and (b), respectively. A total phase shift of over 35° and a total frequency shift of about 10 kHz are clearly visible.

The second analysis uses the more complex model of interference of two RAMAN transitions, eq. (6.3), and applies the BAYESian method to the full data set of all 36 histograms at once. This yields mean values and standard deviations for the RABI frequency, and the LARMOR frequency as well as an offset Δ_0 that the detuning has compared to the imprecise pre-measurements (using $\Delta - \Delta_0$ instead of Δ in eq. (6.3)). Table 6.1 shows these values for three independent measurement series. With these parameters the lines in figure 6.5 are drawn, showing good agreement with the directly retrieved shifts.
The standard deviation of the LARMOR frequency and an additional uncertainty due to the temporal resolution of 320 ps are both in the same order of magnitude, about $5 \cdot 10^{-6}$. Their interplay is even more precise than the independently

measured magnetic-field uncertainty of about 6 nT that corresponds to a relative uncertainty of $2 \cdot 10^{-5}$ and proves the magnetic field fluctuations as the main limitation of the experiment.

Table 6.1 – Values of the model parameters RABI frequency Ω, LARMOR frequency ω_L, and detuning offset Δ_0 for three measurement series.

measurements	$\Omega/2\pi$	$\omega_L/2\pi$	$\Delta_0/2\pi$
series 1 (blue)	894(2) kHz	15.91103(9) MHz	+4.82(6) MHz
series 2 (green)	696(3) kHz	15.91095(16) MHz	+5.75(9) MHz
series 3 (red)	845(3) kHz	15.91111(16) MHz	+6.04(9) MHz

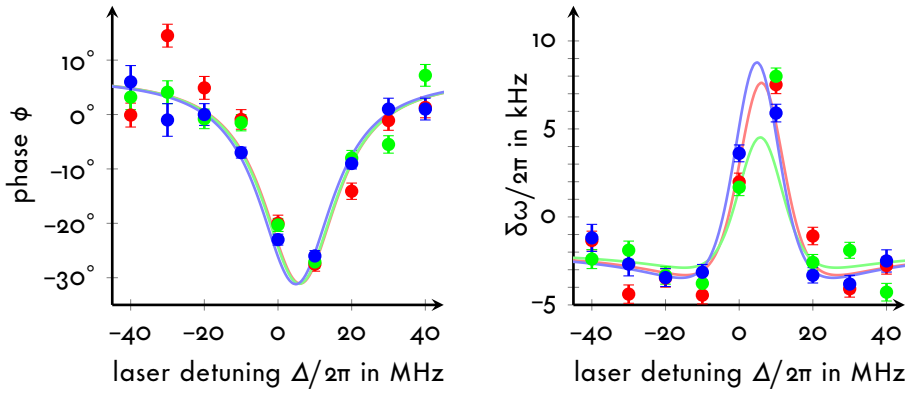

(**a**) Phase shift (**b**) Frequency shift

Figure 6.5 – Phase ϕ and light shift $\delta\omega$ of the LARMOR precession as functions of the detuning Δ. Points indicate the measured data, extracted using the simple sine function, eq. (6.7), lines the full model of section 6.2, and colours different series of measurements.

From the LARMOR frequency ω_L and the radio frequency $\omega_{L,S}$ the LANDÉ factor of the valence electron is inferred to $g_S = 4\omega_{L,S}/\omega_L = 2.002\,21(6)$. This value shows a significant distance of two standard deviations to the LANDÉ factor of the free electron [122], 2.002 319 304 362 56(35), but matches the one for the valence electron of $^{40}Ca^+$, 2.002 256 64(9), found in high-precision measurements using a PENNING trap [123]. It demonstrates the necessity to take even the small energy corrections due to the electromagnetic field of the core electrons into account, and is one of the most remarkable results of the experiment.

6.7 Conclusion

This chapter presents the measurement of a phase shift larger than 35° in the wave function of a single photon. Thereby the photon is used as a self-reference in contrast to other experiments where the exciting laser light serves as reference, and only phase shifts up to 6° were accessible.
The high contrast of the beating as seen in the inset of figure 6.4 reveals that the emitted photons are close to the FOURIER limit. Moreover, it confirms the possibility that the linewidth of RAMAN photons can be much narrower than the natural atomic linewidth of their emitter. This is the case for weak excitation, and it is owed to the temporal stretching of the wave packet.
The method enables a very accurate measurement of the magnetic field down to its fluctuations, more than five orders of magnitude in our case—a degree of precision where not only the small quantum electrodynamical corrections to the LANDÉ factor of 2 in general become relevant, but even the tiny differences between free and bound electrons. The results also demonstrates the importance of, as well as a precise method for the calibration of scattering phases in single-photon-based quantum-networking protocols.

Outlook

«Like the legend of the Phoenix,
All ends with beginnings ...»

— Daft Punk, *Get Lucky* (2012)

The work on this thesis did not start the experimental set-up nor the theory of the Raman scattering, and so it will not finish with any of both or even the development of a quantum computer. But it demonstrates again the fruitfulness of several hybridisations: of different quantum systems, trapped ions and SPDC photon pairs, as well as the marvellous unison of experiment and theory, and not to forget the interplay of experts from different fields in this research group. As it's time to pass on the torch, some issues for the further evolution should be addressed.

As already mentioned in the introduction one of DiVincenzo's criteria that is still missing to advance our quantum interface to a quantum computer is the needed universal set of quantum gates. A fruitful approach is the Mølmer–Sørensen gate [79, 119] on multiple q-bits in combination with all single-q-bit gates. Our first steps in this direction are found in the Ph. D. thesis of Pascal Eich [28]. We have already demonstrated the trapping and cooling of a string of several ions in one trap, and addressing single sites of this string by the application of an acousto-optical deflector.

A new approach to the stabilisation of the static magnetic field following [105] is the change from DC electromagnets (coils) to sets of permanent magnets. This should remove the influence of the fluctuations of the electric current, and thus increase the coherence time of the quantum memory even further. The first step in this direction is the master thesis of Omar Elshehy [30].

With a new trap design including an optical resonator directly around the trap centre, the coupling efficiencies of the light to and from the trapped ion(s) can be improved. This might increase the success probability of the quantum interface by two to three orders of magnitude, which is the best prospect of improvement at the moment.

The control electronics of the set-up are reconditioned at the moment by a new generation of cavity lockers, see the forthcoming Ph. D. thesis of Matthias Kreis. This will enable the next step of automation in the laboratory, where the detection of an error in the laser stabilisation and its re-stabilisation in a fully-automated manner seems a reachable goal.

To complete the picture of the spontaneous Raman scattering, direct measurements of the spectra of Raman-scattered single photons will be a future work of the research group. This would be a validation of our theoretical work (chapter 3 and [82]), and the final evidence that Raman photons—under certain circumstances—are narrower in frequency than their emitter. First steps in this direction are the bachelor theses of Christian Haen [42] and Max Bergerhoff [7].

On the theory side it would be desirable to expand the description of the spontaneous Raman transition by coherent as well as incoherent broadening of the exciting laser's frequency. Another improvement, on a more fundamental level, would be to correct the model by restricting the spectra to exclusively positive frequencies. The negative frequencies are a subsequent error owed to the Weisskopf–Wigner approximation; the correction could be based on a variant of the rotating-wave approximation presented in [8]. Furthermore, the Markovian assumption in section 3.2 could be proved by mathematical induction over the number of scattered photons.

A personal desire of the author is the prosperity of the application of Bayesian inference in the analysis of measurement data as this method is in many cases superior to the more established methods. One of these cases is the quantum tomography with the expected goal to find a simple formula for the entries of the density matrix including reliable uncertainties out of the ratios of detector clicks in a manner similar to the analysis of a Bernoulli process (as tossing a coin).

Danksagung

An dieser Stelle danke ich allen, die mich bei der Erstellung dieser Arbeit unterstützt haben. Als erstes möchte ich meiner Familie danken, zwei Menschen ganz besonders: Kerstin Birster für ihre unerschütterliche Liebe, die Unterstützung in allen Belangen und den beständigen Antrieb, ohne den diese Arbeit wohl kein Ende gefunden hätte, sowie meinem Vater Klaus Müller, der die Vollendung dieser Arbeit leider nicht mehr miterleben konnte.
Die größte Unterstützung auf wissenschaftlicher Seite verdanke ich dem anderen Vater – meinem Doktorvater Jürgen Eschner – der mir den Weg von der Theorie zum Experiment ermöglicht hat und viel zu meinem Verständnis der Atom- und Quantenphysik beigetragen hat. Außerdem hat er immer ein familiäres Verhältnis und eine angenehme Arbeitsatmosphäre gefördert sowie für die Einbindung von Experten unterschiedlicher Richtungen gesorgt – eine große Stärke der Arbeitsgruppe. Zu all dem hat jedes Mitglieder der Gruppe beigetragen. Danken möchte ich insbesondere denen, mit denen ich tagtäglich in den Laboren und Bureaux zusammengearbeitet habe:
Jan Huwer, der das Experiment auf dem Weg von Barcelona nach Saarbrücken begleitet hat, danke ich für seinen freundlichen und ruhigen Umgang und da-

für, dass er mich so angenehm und geduldig in die praktische Arbeit in einem Optiklabor eingeführt hat.
Christoph Kurz und Michael Schug, die mit mir zusammen ihr Doktorat am Ionenexperiment verbracht haben, danke ich für das gute Zusammenspiel bei der Arbeit; unsere unterschiedlichen fachlichen Vorgeschichten haben sich immer gut ergänzt.
Pascal Eich, der den Dialekt laborfähig gemacht hat, und Matthias Kreis, danke ich für die unterhaltsamen und heiteren Stunden in Labor und Bureau sowie für die gewissenhafte Weiterführung und -entwicklung des Ionenexperiments.
Stephan Kucera danke ich für den Pragmatismus, den er allgemein in die Gruppe und speziell mir näher gebracht hat, obwohl das im Gegensatz zu meiner Pedanterie steht.
José Brito und Hannes Gothe danke ich für den andauernden kulturellen und sprachlichen Austausch über die Grenzen des Saarlandes hinweg.
Sicherlich werde ich Euch alle und die AG Quantenphotonik vermissen, schon jetzt vermisse ich die Whisky-Tastings in der Kaffeeküche und die Nachkolloquien in St. Johann.
Da mit dieser Arbeit auch meine Zeit an der Universität zu Ende geht, möchte ich hier auch meinen Kommilitonen danken für eine wundervolle Studienzeit, ohne die diese Arbeit wohl auch anders aussähe: Carsten Volz, Benjamin Sauer, Mathias Grün, Christoph Eisinger, Christian Zeitz, Dominic Scherer, Ramona Servatius, Benjamin Franz, Karsten Schwarz und insbesondere Thomas Sokolowski (ΘΣ).
Erwähnt, wenn auch ungenannt, sollen die vielen sonstigen Forscher, Studenten und Freunde sein, die mir während der ganzen Zeit des Doktorats auf Konferenzen, im Hörsaal und beim Kaffee immer wieder Denkanstöße und neue Ideen gaben.
Abschließend möchte ich es auch nicht missen, Christian Lang und Jürgen Markmann zu danken, die mich in die Welt des Satzprogramms TEX einführten sowie Peter Reichard, der mir die Eleganz der Schriftart «Futura» in Erinnerung rief – beides Dinge, die die Gestaltung dieser Arbeit in einem Höchstmaß beeinflusst haben, so weit, dass darin kein Schriftzeichen enthalten ist, das nicht von mir selbst gestaltet wurde.

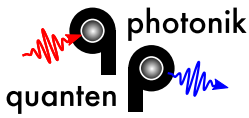

Appendix

«There are only two perfectly useless things in the world.
One is an appendix and the other is Poincaré!»

— G. Clemenceau (1919)[72, p. 33]

A1 Derivation of the Liouville operator

The Liouville operator, eq. (4.4) on p. 64, is derived by rewriting the Lindblad equation (4.1) component-wise using eq. (4.2) and identifying the effective Hamilton operator and some Kronecker products

$$A_{i,s}B_{j,t} = (A \otimes B)_{(i-1)n+j,(s-1)n+t}.$$

The explicit calculation is:

$$
\begin{aligned}
\frac{\mathrm{d}}{\mathrm{d}t}\rho'_{(i-1)n+j} = \frac{\mathrm{d}}{\mathrm{d}t}\rho_{i,j} &= \left(\frac{\mathrm{i}}{\hbar}\left[\hat{\rho},\,\hat{H}\right] + \frac{1}{2}\sum_k\left(2\hat{C}_k\hat{\rho}\hat{C}_k^+ - \hat{\rho}\hat{C}_k^+\hat{C}_k - \hat{C}_k^+\hat{C}_k\hat{\rho}\right)\right)_{i,j} \\
&= \left(\frac{\mathrm{i}}{\hbar}\hat{\rho}\hat{H} - \frac{\mathrm{i}}{\hbar}\hat{H}\hat{\rho} + \sum_k \hat{C}_k\hat{\rho}\hat{C}_k^+ - \frac{1}{2}\sum_k\hat{\rho}\hat{C}_k^+\hat{C}_k - \frac{1}{2}\sum_k\hat{C}_k^+\hat{C}_k\hat{\rho}\right)_{i,j} \\
&= \left(\mathrm{i}\left(\hat{\rho}\left(\frac{\hat{H}}{\hbar} + \frac{\mathrm{i}}{2}\sum_k\hat{C}_k^+\hat{C}_k\right) - \left(\frac{\hat{H}}{\hbar} - \frac{\mathrm{i}}{2}\sum_k\hat{C}_k^+\hat{C}_k\right)\hat{\rho}\right) + \sum_k\hat{C}_k\hat{\rho}\hat{C}_k^+\right)_{i,j} \\
&= \left(\mathrm{i}\left(\hat{\rho}\hat{H}_{\mathrm{eff}}^+ - \hat{H}_{\mathrm{eff}}\hat{\rho}\right) + \sum_k\hat{C}_k\hat{\rho}\hat{C}_k^+\right)_{i,j} \\
&= \mathrm{i}\left(\sum_{t=1}^n \rho_{i,t}\left(H_{\mathrm{eff}}^+\right)_{t,j} - \sum_{s=1}^n\left(H_{\mathrm{eff}}\right)_{i,s}\rho_{s,j}\right) + \sum_k\sum_{s=1}^n\sum_{t=1}^n\left(C_k\right)_{i,s}\rho_{s,t}\left(C_k^+\right)_{t,j} \\
&= \mathrm{i}\left(\sum_{t=1}^n \rho_{i,t}\left(H_{\mathrm{eff}}^*\right)_{j,t} - \sum_{s=1}^n\left(H_{\mathrm{eff}}\right)_{i,s}\rho_{s,j}\right) + \sum_k\sum_{s,t=1}^n\left(C_k\right)_{i,s}\rho_{s,t}\left(C_k^*\right)_{j,t} \\
&= \mathrm{i}\sum_{t=1}^n\sum_{s=1}^n\left(\delta_{i,s}\rho_{s,t}\left(H_{\mathrm{eff}}^*\right)_{j,t} - \left(H_{\mathrm{eff}}\right)_{i,s}\rho_{s,t}\delta_{t,j}\right) + \sum_k\sum_{s,t=1}^n\left(C_k\right)_{i,s}\rho_{s,t}\left(C_k^*\right)_{j,t} \\
&= \sum_{s,t=1}^n\left(\mathrm{i}\left(\delta_{i,s}\left(H_{\mathrm{eff}}^*\right)_{j,t} - \left(H_{\mathrm{eff}}\right)_{i,s}\delta_{j,t}\right) + \sum_k\left(C_k\right)_{i,s}\left(C_k^*\right)_{j,t}\right)\rho_{s,t} \\
&= \sum_{s,t=1}^n\left(\mathrm{i}\left(\mathbb{1}\otimes\hat{H}_{\mathrm{eff}}^* - \hat{H}_{\mathrm{eff}}\otimes\mathbb{1}\right) + \sum_k\hat{C}_k\otimes\hat{C}_k^*\right)_{(i-1)n+j,(s-1)n+t}\rho'_{(s-1)n+t} \\
&= \left(\underbrace{\left(\mathrm{i}\left(\mathbb{1}\otimes\hat{H}_{\mathrm{eff}}^* - \hat{H}_{\mathrm{eff}}\otimes\mathbb{1}\right) + \sum_k\hat{C}_k\otimes\hat{C}_k^*\right)}_{=\hat{\mathcal{L}}}\cdot\boldsymbol{\rho}'\right)_{(i-1)n+j}
\end{aligned}
$$

A 2 Quantum process tomography

To judge the quality of the mapping of one q-bit $\hat{\rho}_{in}$ onto another one $\hat{\rho}_{ex}$, the process matrix $\hat{\chi}$ is reconstructed following the definition in [17]. In the case of a single q-bit, it is a four-dimensional matrix fulfilling the transformation equation

$$\hat{\rho}_{ex} = \sum_{m,n=0}^{3} \chi_{mn} \hat{A}_m \hat{\rho}_{in} \hat{A}_n^+$$

for all possible pairs of $\hat{\rho}_{in}$ and $\hat{\rho}_{ex}$. Herein, the operators $\{\hat{A}_m\}$ are $\mathbb{1}$, $\hat{\sigma}_x$, $-i\hat{\sigma}_y$, and $\hat{\sigma}_z$, respectively. The process matrix can be calculated out of the four reconstructed density matrices, $\hat{\rho}_R$, $\hat{\rho}_L$, $\hat{\rho}_H$, and $\hat{\rho}_D$, after performing the mapping of the initial states, $|R\rangle$, $|L\rangle$, $|H\rangle$, and $|D\rangle$, respectively, onto a photon. The explicit formula is

$$\hat{\chi} = \hat{\lambda} \hat{\rho}' \hat{\lambda}$$

with

$$\hat{\lambda} = \frac{1}{2} \begin{pmatrix} \mathbb{1} & \hat{\sigma}_x \\ \hat{\sigma}_x & -\mathbb{1} \end{pmatrix} = \frac{1}{2} \begin{pmatrix} 1 & 0 & 0 & 1 \\ 0 & 1 & 1 & 0 \\ 0 & 1 & -1 & 0 \\ 1 & 0 & 0 & -1 \end{pmatrix} \qquad \text{and} \qquad \hat{\rho}' = \begin{pmatrix} \hat{\rho}_R & \hat{\rho}_+ \\ \hat{\rho}_- & \hat{\rho}_L \end{pmatrix}$$

wherein $\hat{\rho}_\pm = \hat{\rho}_H \pm i\hat{\rho}_D - \frac{1}{2}(1 \pm i)(\hat{\rho}_R + \hat{\rho}_L)$.
Alternatively, many textbooks define the process matrix slightly different through

$$\hat{\rho}_{ex} = \sum_{m,n=0}^{3} \bar{\chi}_{mn} \hat{\sigma}_m \hat{\rho}_{in} \hat{\sigma}_n^+ \tag{1}$$

with the unity matrix and the PAULI matrices directly, $\hat{\sigma}_m = \{\mathbb{1}, \hat{\sigma}_x, \hat{\sigma}_y, \hat{\sigma}_z\}$. This obviously leads to a different process matrix, $\hat{\bar{\chi}} = \hat{U}\hat{\chi}\hat{U}^+ \neq \hat{\chi}$, with $\hat{U} = \mathrm{diag}(1, 1, -i, 1)$, but both share the same properties inherited from the density matrix. They are positive semi-definite, HERMITian, and have trace 1.
The value of interest is the first entry, $\bar{\chi}_{00} = \chi_{00}$, indicating the identity part of the process. It tells how good the information of the q-bit is preserved, and thus is called process fidelity. It is connected with the overlap fidelity, $F = \mathrm{tr}(\hat{\rho}_{in}\hat{\rho}_{ex})$, averaged over all pure input states, through $\langle F \rangle = (2\chi_{00} + 1)/3$.

Furthermore, reference [17] gives a very clear visualisation of the mapping for the case of a single q-bit. With the quantum states written as BLOCH vectors, $\boldsymbol{r}_{in}$ and

$\boldsymbol{r}_{\mathrm{ex}}$, according to eq. (1.1) on p. 8, the transformation (1) takes the shape

$$\boldsymbol{r}_{\mathrm{ex}} = M\boldsymbol{r}_{\mathrm{in}} + \boldsymbol{c}.$$

Therein, the three-dimensional, real matrix M and the constant, real vector $\boldsymbol{c}$ are directly determined by $\hat{\bar{\chi}}$ through,

$$\begin{aligned} M_{ij} &= (2\bar{\chi}_{00} - 1)\delta_{ij} + 2\,\mathrm{Re}(\bar{\chi}_{ij}) - 2\sum_{k=1}^{3} \varepsilon_{ijk}\,\mathrm{Im}(\bar{\chi}_{0k}), \\ c_i &= 4\,\mathrm{Re}(\bar{\chi}_{0i}), \end{aligned}$$

and vice versa,

$$\begin{aligned} \bar{\chi}_{00} &= \frac{1}{4}(1 + \mathrm{tr}(M)), \\ \bar{\chi}_{0i} &= \frac{1}{4}\left(c_i - \mathrm{i}\sum_{k=1}^{3}\sum_{j=1}^{3} \varepsilon_{ijk}M_{jk}\right), \\ \bar{\chi}_{ij} &= \frac{1}{4}\left((1 - \mathrm{tr}(M))\delta_{ij} + M_{ij} + M_{ji} - \mathrm{i}\sum_{k=1}^{3} \varepsilon_{ijk}c_k\right), \end{aligned}$$

wherein the indices i and j only go from 1 to 3, and ε_{ijk} denotes the three-dimensional Levi-Civita tensor.
This shows, that the Bloch sphere defined by all possible states $\{\boldsymbol{r}_{\mathrm{in}}\}$ is shrunk into an ellipsoid with semi-axes less than 1, possibly rotated, and shifted off the origin by the vector $\boldsymbol{c}$. The explicit values for shrinkage and rotation are found by singular value decomposition (SVD) of the matrix M. Several examples of such «deformed Bloch spheres» are found in section 5.3 on p. 89.

A 3 The Clebsch–Gordan coefficients

This section presents the Clebsch–Gordan coefficients (c_{CG}) of all seven transitions in $^{40}Ca^{+}$ (see figure 1.2 on p. 11). They are displayed in the following energy schemes, figure A.1. For clarity, each c_{CG} is written at its respective transition line, the square-root sign is omitted, and the constant factor is written aside, e. g. the coefficient for the transition from $|S_{1/2}, -\frac{1}{2}\rangle$ to $|P_{1/2}, +\frac{1}{2}\rangle$, see figure A.1 (c), is $c_{CG} = -\sqrt{2/3}$. It pertains to the angular momentum values $J_1 = \frac{1}{2}$, $m_{J_1} = -\frac{1}{2}$, $J_2 = 1$, $m_{J_2} = +1$, $J = \frac{1}{2}$, and $m_J = +\frac{1}{2}$.

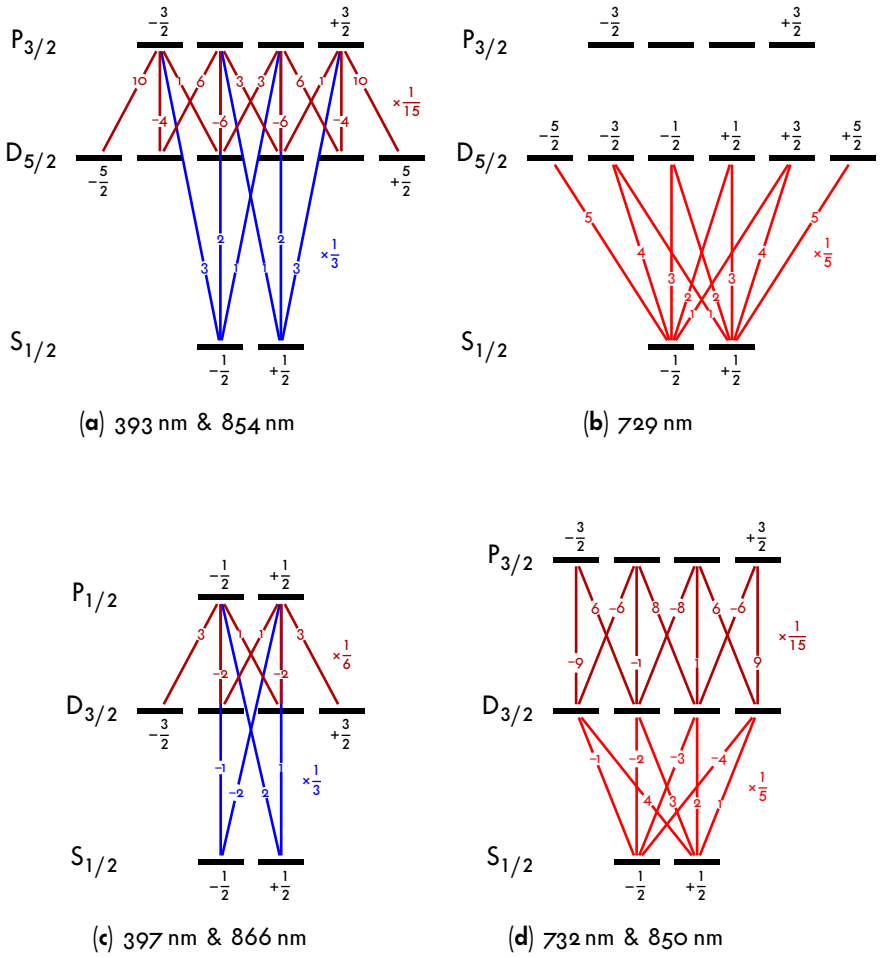

(a) 393 nm & 854 nm (b) 729 nm

(c) 397 nm & 866 nm (d) 732 nm & 850 nm

Figure A.1 – The Clebsch–Gordan coefficients of $^{40}Ca^{+}$.

Remark: In the case of different multiplicities of the lower and upper manifold, the values presented in this figure are valid only for expressing an upper state as a composition of lower states (corresponding to an emission process). Regarding the 866 nm transition as an example (see figure A.1 (c)), one gets

$$\left|P_{1/2},+\tfrac{1}{2}\right\rangle \to \sqrt{\tfrac{1}{6}}\left|D_{3/2},-\tfrac{1}{2}\right\rangle|\sigma^+\rangle - \sqrt{\tfrac{2}{6}}\left|D_{3/2},+\tfrac{1}{2}\right\rangle|\pi\rangle + \sqrt{\tfrac{3}{6}}\left|D_{3/2},+\tfrac{3}{2}\right\rangle|\sigma^-\rangle.$$

Expressing a lower state as a composition of upper states (corresponding to an absorption of a photon with polarisation coefficients c_-, c_0, c_+), the Clebsch–Gordan coefficients have to be renormalised by the square root of the quotient of these multiplicities (4 : 2 in the example above), e. g.

$$\left|D_{3/2},+\tfrac{1}{2}\right\rangle (c_-|\sigma^-\rangle + c_0|\pi\rangle + c_+|\sigma^+\rangle) \to c_-\sqrt{\tfrac{1}{3}}\left|P_{1/2},-\tfrac{1}{2}\right\rangle - c_0\sqrt{\tfrac{2}{3}}\left|P_{1/2},+\tfrac{1}{2}\right\rangle.$$

Bibliography

[1] J. Aldrich «R. A. Fisher and the Making of Maximum Likelihood 1912–1922» in *Statistical Science* **12**.3 (1997), 162. DOI: 10.1214/ss/1030037906 (→ 103).

[2] S. A. Aljunid, M. K. Tey, B. Chng, T. Liew, G. Maslennikov, V. Scarani & C. Kurtsiefer «Phase Shift of a Weak Coherent Beam Induced by a Single Atom» in *Phys. Rev. Lett.* **103** (2009), 153601 (→ 97).

[3] M. Almendros «Towards Long-Distance Quantum Communication» Ph. D. thesis at *Institut de Ciències Fotòniques & Universitat Politècnica de Catalunya*, 2009 (→ 15, 20, 22).

[4] J. Arenskötter «Photonenpaarquelle für Einzelatom-Einzelphoton Wechselwirkung» Master thesis at *Universität des Saarlandes*, 2016 (→ 21, 91).

[5] S. H. Autler & C. H. Townes «Stark Effect in Rapidly Varying Fields» in *Phys. Rev.* **100**.2 (1955), 703 (→ 53).

[6] T. Bayes & R. Price «An Essay towards solving a Problem in the Doctrine of Chance» in *Philosophical Transactions of the Royal Society of London* **53** (1763), 370 (→ 102).

[7] M. L. Bergerhoff «Spektren der Resonanzfluoreszenz eines einzelnen Calciumions» Bachelor thesis at *Universität des Saarlandes*, 2019 (→ 110).

[8] P. R. Berman & G.W. Ford «Spectrum in spontaneous emission: Beyond the Weisskopf-Wigner approximation» in *Phys. Rev. A* **82** (2010), 23818. DOI: 10.1103/PhysRevA.82.023818 (→ 110).

[9] E. D. Black «An introduction to Pound–Drever–Hall laser frequency stabilization» in *Am. J. Phys.* **69** (2001), 79. DOI: 10.1119/1.1286663 (→ 20).

[10] R. Blatt «Rechnen mit Quanten» in *Physik Journal* **11**.8/9 (2012), 35. DOI: 10.1103/PhysRevLett.109.080501 (→ 12).

[11] F. Bloch & A. Siegert «Magnetic Resonance for Nonrotating Fields» in *Phys. Rev.* **57** (1940), 522. DOI: 10.1103/PhysRev.57.522 (→ 68).

[12] M. Bock, P. Eich, S. Kucera, M. Kreis, A. Lenhard, C. Becher & J. Eschner «High-fidelity entanglement between a trapped ion and a telecom photon via quantum frequency conversion» in *Nat. Commun.* **9** (2018), 1998. DOI: 10.1038/s41467-018-04341-2 (→ 4).

[13] H-J. Briegel, T. Calarco, D. Jaksch, J. I. Cirac & P. Zoller «Quantum computing with neutral atoms» in *J. Mod. Opt.* **47** (2000), 415. DOI: 10.1080/09500340008244052 (→ 3).

[14] H-J. Briegel, W. Dür, J. I. Cirac & P. Zoller «Quantum Repeaters: The Role of Imperfect Local Operations in Quantum Communication» in *Phys. Rev. Lett.* **81** (1998), 5932. DOI: 10.1103/PhysRevLett.81.5932 (→ 3).

[15] J. Brito, S. Kucera, P. Eich, P. Müller & J. Eschner «Doubly heralded single-photon absorption by a single atom» in *Appl. Phys. B* **122** (2016), 36. DOI: 10.1007/s00340-015-6276-9 (→ 6, 92).

[16] I. L. Chuang, N. Gershenfeld, M. G. Kubinec & D. W. Leung «Bulk quantum computation with nuclear magnetic resonance: theory and experiment» in *Proc. R. Soc. A* **454**.1969 (1998), 447. DOI: 10.1098/rspa.1998.0170 (→ 3).

[17] I. L. Chuang & M. A. Nielsen «Prescription for experimental determination of the dynamics of a quantum black box» in *J. Mod. Opt.* **44**.11-12 (1997), 2455. DOI: 10.1080/09500349708231894 (→ 115).

[18] J. Clarke & F. K. Wilhelm «Superconducting quantum bits» in *Nature* **453** (2008), 1031. DOI: 10.1038/nature07128 (→ 3).

[19] C. Cohen-Tannoudji, J. Dupont-Roc & G. Grynberg «Atom-Photon Interactions – Basic Processes and Applications» Wiley-VCH Verlag, 2004 (→ 45, 47, 51).

[20] D. Deutsch «Quantum theory, the Church-Turing principle and the universal quantum computer» in *Proc. Royal Soc. Lond. A* **400** (1985), 97. DOI: 10.1098/rspa.1985.0070 (→ 2).

[21] D. Deutsch & R. Jozsa «Rapid solution of problems by quantum computation» in *Proc. Royal Soc. Lond. A* **439** (1992), 553. DOI: 10.1098/rspa.1992.0167 (→ 2).

[22] D. P. DiVincenzo «Topics in Quantum Computers» in «Mesoscopic Electron Transport» Lydia L. Sohn, Leo P. Kouwenhoven and Gerd Schön, 1997. DOI: 10.1007/978-94-015-8839-3 (→ 3).

[23] D. P. DiVincenzo «The Physical Implementation of Quantum Computation» in *Fortschr. Phys.* **48**.9–11 (2000), 771. DOI: 10.1002/1521-3978(200009)48:9/11<771::AID-PROP771>3.0.CO;2-E (→ 3).

[24] R. W. P. Drever, J. L. Hall, F. V. Kowalski, J. Hough, G. M. Ford, A. J. Munley & H. Ward «Laser phase and frequency stabilization using an optical resonator» in *Appl. Phys. B* **31**.2 (1983), 97. DOI: 10.1007/BF00702605 (→ 20).

[25] W. Dür, H-J. Briegel, J. I. Cirac & P. Zoller «Quantum repeaters based on entanglement purification» in *Phys. Rev. A* **59** (1999), 169. DOI: 10.1103/PhysRevA.59.169 (→ 4).

[26] S. Earnshaw «On the Nature of the Molecular Forces which regulate the Constitution of the Luminiferous Ether» in *Trans. Camb. Phil. Soc.* **7** (1842), 97 (→ 13).

[27] G. Eckhardt, R. W. Hellwarth, F. J. McClung, S. E. Schwarz, D. Weiner & E. J. Woodbury «Stimulated Raman Scattering From Organic Liquids» in *Phys. Rev. Lett.* **9** (1962), 455. DOI: 10.1103/PhysRevLett.9.455 (→ 44).

[28] P. Eich «Single-ion based quantum interfaces for quantum-network applications» Ph. D. thesis at *Universität des Saarlandes*, 2019 (→ 16, 109).

[29] A. Einstein «A letter to Michele Besso» 12. Dec. 1951 (→ 43).

[30] O. Elshehy «Permanent-magnet-based Zeeman field genertion in an ion trap» Master thesis at *Universität des Saarlandes*, 2018 (→ 110).

[31] R. P. Feynman «Simulating Physics with Computers» in *Int. J. Theor. Phys.* **21**.6/7 (1982), 467. DOI: 10.1007/BF02650179 (→ 2).

[32] R. P. Feynman «Quantum mechanical computers» in *Found. Phys.* **16**.6 (1986), 507. DOI: 10.1007/BF01886518 (→ 79).

[33] R. P. Feynman, F. L. Vernon Jr. & R. W. Hellwarth «Geometrical Representation of the Schrödinger Equation for Solving Maser Problems» in *J. Appl. Phys.* **28** (1957), 49. DOI: 10.1063/1.1722572 (→ 8).

[34] R. A. Fisher «An absolute criterion for fitting frequency curves» in *Messenger of Math.* **41** (1912), 155 (→ 103).

[35] J. Fraunhofer «Bestimmung des Brechungs- und des Farbenzerstreungs-Vermögens verschiedener Glasarten, in Bezug auf die Vervollkommnung achromatischer Fernröhre» in *Annalen der Physik* **56**.7 (1817), 264. DOI: 10.1002/andp.18170560706 (→ 13).

[36] S. Gerber, D. Rotter, M. Hennrich, R. Blatt, F. Rohde, C. Schuck, M. Almendros, R. Gehr, F. Dubin & J. Eschner «Quantum interference from remotely trapped ions» in *New J. Phys.* **11** (2009), 13032 (→ 17, 96).

[37] L. K. Grover «Quantum Mechanics Helps in Searching for a Needle in a Haystack» in *Proceedings of the Annual Symposium on the Theory of Computing* **28** (1996), 212 (→ 2).

[38] L. K. Grover «Quantum Mechanics Helps in Searching for a Needle in a Haystack» in *Phys. Rev. Lett.* **79**.2 (1997), 325. DOI: 10.1103/PhysRevLett.79.325 (→ 2).

[39] S. Gulde, M. Riebe, G. P. T. Lancaster, C. Becher, J. Eschner, H. Häffner, F. Schmidt-Kaler, I. L. Chuang & R. Blatt «Implementation of the Deutsch–Jozsa algorithm on an ion-trap quantum computer» in *Nature* **421** (2003), 48. DOI: 10.1038/nature01336 (→ 3, 12).

[40] S. T. Gulde «Experimental Realization of Quantum Gates and the Deutsch-Jozsa Algorithm with Trapped $^{40}Ca^{+}$ Ions» Ph. D. thesis at *Leopold-Franzens-Universität Innsbruck*, 2003 (→ 15).

[41] A. Haase, N. Piro, J. Eschner & M. W. Mitchell «Tunable narrowband entangled photon pair source for resonant single-photon single-atom interaction» in *Opt. Lett.* **34** (2009), 55. DOI: 10.1364/OL.34.000055 (→ 21).

[42] C. Haen «Spektralanalyse von Einzelphotonen» Bachelor thesis at *Universität des Saarlandes*, 2017 (→ 110).

[43] H. Heald & H. P. Lovecraft «The Horror in the Museum» in *Weird Tales* **22**.1 (1933), 49 (→ 7).

[44] W. Heitler «The Quantum Theory of Radiation» 3rd ed. Dover Publications, Inc., 1984 (→ 48).

[45] G. Hétet, L. Slodička, N. Röck & R. Blatt «Free-space read-out and control of single-ion dispersion using quantum interference» in *Phys. Rev. A* **88** (2013), 41804(R) (→ 97).

[46] R. Horodecki, P. Horodecki, M. Horodecki & K. Horodecki «Quantum entanglement» in *Rev. Mod. Phys.* **81** (2009), 865.
DOI: 10.1103/RevModPhys.81.865 (→ 2).

[47] J. Huwer «Experimental tools for quantum networking operations with single photons and single ions» Ph. D. thesis at *Institut de Ciències Fotòniques & Universitat Politècnica de Catalunya & Universität des Saarlandes*, 2013 (→ 11, 16, 19, 63, 89).

[48] D. F. V. James, P. G. Kwiat, W. J. Munro & A. G. White «Measurement of qubits» in *Phys. Rev. A* **64** (2001), 52312. DOI: 10.1103/PhysRevA.64.052312 (→ 93).

[49] E. T. Jaynes «Information Theory and Statistical Mechanics» in *Phys. Rev.* **106**.4 (1957), 620. DOI: 10.1103/PhysRev.106.620 (→ 103).

[50] E. T. Jaynes «Probability Theory – The Logic of Science» ed. by G. L. Bretthorst Cambridge University Press, 2003 (→ 101, 102, 105).

[51] F. Jelezko & J. Wrachtrup «Single defect centres in diamond: A review» in *Phys. stat. sol. (a)* **203**.13 (2006), 3207. DOI: 10.1002/pssa.200671403 (→ 3).

[52] J. Jin & D. A. Church «Precision Lifetimes for the Ca^+ $4p\,^2P$ Levels: Experiment Challenges Theory at a 1% Level» in *Phys. Rev. Lett.* **70** (1993), 3213 (→ 12).

[53] H. Kaufmann, T. Ruster, C. T. Schmiegelow, M. A. Luda, V. Kaushal, J. Schulz, D. von Lindenfels, F. Schmidt-Kaler & U. G. Poschinger «Scalable Creation of Long-Lived Multipartite Entanglement» in *Phys. Rev. Lett.* **119** (2017), 150503.
DOI: 10.1103/PhysRevLett.119.150503 (→ 12).

[54] P. L. Knight «Theory of near-resonant spontaneous Raman scattering» in *J. Phys. B* **13** (1980), 4551 (→ 44).

[55] A. Kossakowski «On quantum statistical mechanics of non-Hamiltonian systems» in *Rep. Math. Phys.* **3**.4 (1972), 247 (→ 64).

[56] M. Kreis «Magnetfeldstabilisierung für Hochpräzise Einzelatom Spektroskopie» Master thesis at *Universität des Saarlandes*, 2014 (→ 18).

[57] A. Kreuter, C. Becher, G. P. T. Lancaster, A. B. Mundt, C. Russo, H. Häffner, C. Roos, W. Hänsel, F. Schmidt-Kaler & R. Blatt «Experimental and theoretical study of the $3d\,^2D$–level lifetimes of $^{40}Ca^+$» in *Phys. Rev. A* **71** (2005), 32504 (→ 12).

[58] S. Kucera «Digitale LASER-Leistungsstabilisierung für Einzelatomspektroskopie» Diploma thesis at *Universität des Saarlandes*, 2013 (→ 16, 22).

[59] S. Kucera «Experimental distribution of entanglement in ion-photon quantum networks: Photon-pairs as resource» Ph. D. thesis at *Universität des Saarlandes*, 2019 (→ 21, 23, 79, 89, 92).

[60] S. Kucera, J. Arenskötter, M. Kreis, P. Eich, P. Müller & J. Eschner «Photon-photon to atom-photon entanglement transfer to a $^{40}Ca^{+}$ quantum node and state readout by teleportation» (→ 6, 21, 79, 91).

[61] C. Kurz, J. Huwer, M. Schug, P. Müller & J. Eschner «A high-rate source for single photons in a pure quantum state» in *New J. Phys.* **15** (2013), 055005. DOI: 10.1088/1367-2630/15/5/055005 (→ 5, 74).

[62] C. Kurz «Quantum networking with single ions and single photons interfaced in free space» Ph. D. thesis at *Universität des Saarlandes*, 2015 (→ 16, 20, 63, 79, 80, 89, 90).

[63] C. Kurz, P. Eich, M. Schug, P. Müller & J. Eschner «Programmable atom-photon quantum interface» in *Phys. Rev. A* **93** (2016), 62348. DOI: 10.1103/PhysRevA.93.062348 (→ 6, 79, 80, 82, 92, 101).

[64] C. Kurz, M. Schug, P. Eich, J. Huwer, P. Müller & J. Eschner «Experimental protocol for high-fidelity heralded photon-to-atom quantum state transfer» in *Nat. Commun.* **5** (2014), 5527. DOI: 10.1038/ncomms6527 (→ 5, 79, 80, 90, 95, 101).

[65] E. C. Le Ru, E. Blackie, M. Meyer & P. G. Etchegoin «Surface Enhanced Raman Scattering Enhancement Factors: A Comprehensive Study» in *J. Phys. Chem. C* **111**.37 (2007), 13794. DOI: 10.1021/jp0687908 (→ 44).

[66] A. Lenhard, M. Bock, C. Becher, S. Kucera, J. Brito, P. Eich, P. Müller & J. Eschner «Telecom-heralded single-photon absorption by a single atom» in *Phys. Rev. A* **92** (2015), 63827 (→ 6, 92, 99).

[67] A. Lenhard, J. Brito, M. Bock, C. Becher & J. Eschner «Coherence and entanglement preservation of frequency-converted heralded single photons» in *Opt. Express* **25**.10 (2017), 11187. DOI: 10.1364/OE.25.011187 (→ 4).

[68] R. Lepsius «Die alt-aegyptische Elle und ihre Eintheilung» in *Abhandlungen der Königl. Akademie der Wissenschaften zu Berlin* (1866), 1 (→ 8).

[69] G. Lindblad «On the Generators of Quantum Dynamical Semigroups» in *Commun. Math. Phys.* **48**.2 (1976), 119 (→ 64).

[70] D. Loss & D. P. DiVincenzo «Quantum computation with quantum dots» in *Phys. Rev. A* **57** (1998), 120. DOI: 10.1103/PhysRevA.57.120 (→ 3).

[71] H. Lyre «Quantum Theory of Ur-Objects as a Theory of Information» in *Int. J. Theor. Phys.* **34**.8 (1995), 1541. DOI: 10.1007/BF00676265 (→ 8).

[72] M. MacMillan «Paris 1919 – Six Months That Changed the World» Random House Publishing Group, 2007 ISBN: 978-0-307-43296-4 (→ 113).

[73] Y. I. Manin «Vychislimoe i nevychislimoe» Sovietskoie radio, 1980 (→ 2).

[74] T. A. Marian «Higher-order multipole expansion in the Dirac equation» in *Phys. Rev. A* **53**.4 (1996), 1992. DOI: 10.1103/PhysRevA.53.1992 (→ 29).

[75] É. L. Mathieu «Mémoire sur le mouvement vibratoire d'une membrane de forme elliptique» in *Journal de Mathématiques Pures et Appliquées* **13** (1868), 137 (→ 14).

[76] J. Meija, T. B. Coplen, M. Berglund, W. A. Brand, P. D. Bièvre, M. Gröning, N. E. Holden, J. Irrgeher, R. D. Loss, T. Walczyk & T. Prohaska «Isotopic compositions of the elements 2013 (IUPAC Technical Report)» in *Pure Appl. Chem.* **88**.3 (2016), 293. DOI: 10.1515/pac-2015-0503 (→ 11).

[77] N. D. Mermin «Could Feynman Have Said This?» in *Physics Today* **57**.5 (2004), 10. DOI: 10.1063/1.1768652 (→ 63).

[78] K. Mølmer, Y. Castin & J. Dalibard «Monte Carlo wave-function method in quantum optics» in *J. Opt. Soc. Am. B* **10**.3 (1993), 524 (→ 64, 68).

[79] K. Mølmer & A. Sørensen «Multiparticle Entanglement of Hot Trapped Ions» in *Phys. Rev. Lett.* **82**.9 (1999), 1835. DOI: 10.1103/PhysRevLett.82.1835 (→ 109).

[80] P. Müller & J. Eschner «Single calcium-40 ion as quantum memory for photon polarization: a case study» in *Appl. Phys. B* **114** (2014), 303 (→ 5, 79, 82, 85).

[81] P. Müller, M. Kreis, P. Eich & J. Eschner «Measurement of the scattering phase in a spontaneous Raman process» (→ 6, 95).

[82] P. Müller, T. Tentrup, M. Bienert, G. Morigi & J. Eschner «Spectral properties of single photons from quantum emitters» in *Phys. Rev. A* **96** (2017), 23861. DOI: 10.1103/PhysRevA.96.023861 (→ 6, 45, 49, 51, 52, 57, 58, 97, 110).

[83] K. Nakamura et al. «Review of Particle Physics» in *J. Phys. G: Nucl. Part. Phys.* **37**.7A (July 2010), 075021. DOI: 10.1088/0954-3899/37/7a/075021 (→ 34).

[84] D. Nolting, R. Malek & A. Makarov «Ion traps in modern mass spectrometry» in *Mass Spec. Rev.* **38** (2017), 150. DOI: 10.1002/mas.21549 (→ 13).

[85] R. O'Brien & J. Sharman «The Rocky Horror Picture Show» 1975 (→ 1).

[86] W. Paul «Apparatus for separating charged particles of different specific charges» Patent US 2939952 Dec. 1953 (→ 13).

[87] W. Paul «Ein neues Massenspektrometer ohne Magnetfeld» in *Zeitschrift für Naturforschung A* **8**.7 (1953), 448 (→ 13).

[88] W. Paul «Improved arrangements for separating or separately detecting charged particles of different specific charges» Patent GB 773689 Dec. 1953 (→ 13).

[89] W. Paul «Verfahren zur Trennung bzw. zum getrennten Nachweis von Ionen verschiedener spezifischer Ladung» Patent DE 944900 Dec. 1953 (→ 13).

[90] W. Paul «Electromagnetic Traps for Charged and Neutral Particles» Nobel-prize lecture Dec. 1989 (→ 13).

[91] W. Pauli jr. «Zur Quantenmechanik des magnetischen Elektrons» in *Zeitschrift für Physik* **43**.9 (1927), 601 ISSN: 0044-3328. DOI: 10.1007/BF01397326 (→ 8, 26).

[92] K. Pearson «On the Criterion that a given System of Deviations from the Probable in the Case of a Correlated System of Variables is such that it can be reasonably supposed to have arisen from Random Sampling» in *Philosophical Magazine Series 5* **50** (1900), 157. DOI: 10.1080/14786440009463897 (→ 104).

[93] N. Piro «Controlled absorption of heralded single photons by a single atom: Towards entanglement distribution in quantum networks» Ph. D. thesis at *Institut de Ciències Fotòniques & Universitat Politècnica de Catalunya*, 2010 (→ 21).

[94] N. Piro, A. Haase, M.W. Mitchell & J. Eschner «An entangled photon source for resonant single-photon–single-atom interaction» in *J. Phys. B: At. Mol. Opt. Phys.* **42** (2009), 114002. DOI: 10.1088/0953-4075/42/11/114002 (→ 21).

[95] S-D. Poisson «Recherches sur la probabilité des jugements en matière criminelle et en matière civile – précédées des règles générales du calcul des probabilités» 1837 (→ 105).

[96] K. Popper «Logik der Forschung – Zur Erkenntnistheorie der modernen Naturwissenschaft» Philipp Frank and Moritz Schlick, 1934 isbn: 78-3-7091-2021-7 (→ 102).

[97] M. Pototschnig, Y. Chassagneux, J. Hwang, G. Zumofen, A. Renn & V. Sandoghdar «Controlling the Phase of a Light Beam with a Single Molecule» in *Phys. Rev. Lett.* **107** (2011), 63001 (→ 97).

[98] «Quantities and units – Part 2: Mathematical signs and symbols to be used in the natural sciences and technology (ISO80000-2)» International Organization for Standardization (ISO), 2009 (→ 10).

[99] C.V. Raman & K.S. Krishnan «A New Type of Secondary Radiation» in *Nature* **121** (1928), 501. DOI: 10.1038/121501c0 (→ 44).

[100] M. Ramm, T. Pruttivarasin, M. Kokish, I. Talukdar & H. Häffner «Precision Measurement Method for Branching Fractions of Excited $P_{1/2}$ States Applied to $^{40}Ca^{+}$» in *Phys. Rev. Lett.* **111** (2013), 23004 (→ 12).

[101] N. F. Ramsey «A Molecular Beam Resonance Method with Separated Oscillating Fields» in *Phys. Rev.* **78** (1950), 695. DOI: 10.1103/PhysRev.78.695 (→ 18, 99).

[102] L. Ricci, M. Weidemüller, T. Esslinger, A. Hemmerich, C. Zimmermann, V. Vuletic, W. König & T.W. Hänsch «A compact grating-stabilized diode laser system for atomic physics» in *Opt. Commun.* **117**.5 (1995), 541.
DOI: 10.1016/0030-4018(95)00146-Y (→ 19).

[103] F. Rohde, M. Almendros, C. Schuck, J. Huwer, M. Hennrich & J. Eschner «A diode laser stabilization scheme for $^{40}Ca^{+}$ single-ion spectroscopy» in *J. Phys. B: At. Mol. Opt. Phys.* **43**.11 (2010), 115401.
DOI: 10.1088/0953-4075/43/11/115401 (→ 19, 20).

[104] F. Rohde «Remote ion traps for quantum networking: Two-photon interference and correlations» Ph. D. thesis at *Institut de Ciències Fotòniques & Universitat Politècnica de Catalunya*, 2009 (→ 15, 20).

[105] T. Ruster, C.T. Schmiegelow, K. Kaufmann, C. Warschburger, F. Schmidt-Kaler & U. G. Poschinger «A long-lived Zeeman trapped-ion qubit» in *Appl. Phys. B* **122** (2016), 254. DOI: 10.1007/s00340-016-6527-4 (→ 110).

[106] B. E. A. Saleh & M. C. Teich «Grundlagen der Photonik» Wiley-VCH Verlag, 2008 isbn: 978-3-527-40677-7 (→ 44).

[107] N. Sangouard, J-D. Bancal, P. Müller, J. Ghosh & J. Eschner «Heralded mapping of photonic entanglement into single atoms in free space: proposal for a loophole-free Bell test» in *New J. Phys.* **15** (2013), 085004. DOI: 10.1088/1367-2630/15/8/085004 (→ 5).

[108] F. Schmidt-Kaler, H. Häffner, M. Riebe, S. Gulde, G.P.T. Lancaster, T. Deutschle, C. Becher, C. F. Roos, J. Eschner & R. Blatt «Realization of the Cirac–Zoller controlled-NOT quantum gate» in *Nature* **422** (2003), 408. DOI: 10.1038/nature01494 (→ 12).

[109] E. Schrödinger «Are There Quantum Jumps? Part II» in *Brit. J. Phil. Sci.* **3**.11 (1952), 233. DOI: 10.1093/bjps/III.11.233 (→ 13).

[110] C. Schuck «Interfacing single ions and single photons for quantum networks» Ph. D. thesis at *Institut de Ciències Fotòniques & Universitat Politècnica de Catalunya*, 2009 (→ 13, 15, 16).

[111] M. Schug, J. Huwer, C. Kurz, P. Müller & J. Eschner «Heralded Photonic Interaction between Distant Single Ions» in *Phys. Rev. Lett.* **110** (2013), 213603. DOI: 10.1103/PhysRevLett.110.213603 (→ 5, 15, 63).

[112] M. Schug «Single photons from single ions: quantum interference and distant ion interaction» Ph. D. thesis at *Universität des Saarlandes*, 2015 (→ 16, 45, 63).

[113] M. Schug, C. Kurz, P. Eich, J. Huwer, P. Müller & J. Eschner «Quantum interference in the absorption and emission of single photons by a single ion» in *Phys. Rev. A* **90** (2014), 23829 (→ 5, 63, 82).

[114] B. Schumacher «Quantum coding» in *Phys. Rev. A* **51**.4 (1995), 2738. DOI: 10.1103/PhysRevA.51.2738 (→ 8).

[115] P.W. Shor «Algorithms for Quantum Computation: Discrete Logarithms and Factoring» in *Proceedings of the Annual Symposium on Foundations of Computer Science* **35** (1994), 124. DOI: 10.1109/SFCS.1994.365700 (→ 2).

[116] P.W. Shor «Polynomial-Time Algorithms for Prime Factorization and Discrete Logarithms on a Quantum Computer» in *SIAM J. Comput.* **26**.5 (1997), 1484. DOI: 10.1137/S0097539795293172 (→ 2).

[117] A. Smekal «Zur Quantentheorie der Dispersion» in *Naturwissenschaften* **11**.43 (1923), 873 issn: 1432-1904. DOI: 10.1007/BF01576902 (→ 44).

[118] M. Sondermann & G. Leuchs «The phase shift induced by a single atom in free space» in *J. Europ. Opt. Soc. Rap. Public.* **8** (2013), 13052 (→ 97).

[119] A. Sørensen & K. Mølmer «Quantum Computation with Ions in Thermal Motion» in *Phys. Rev. Lett.* **82**.9 (1999), 1971. DOI: 10.1103/PhysRevLett.82.1971 (→ 109).

[120] G. G. Stokes «On the Composition and Resolution of Streams of Polarized Light from different Sources» in *Trans. Camb. Phil. Soc.* **9** (1852), 399 (→ 10).

[121] T. Tentrup «Spektrale Eigenschaften einzelner Photonen von einzelnen Emittern» Master thesis at *Universität des Saarlandes*, 2014 (→ 6, 45).

[122] E. Tiesinga, P. J. Mohr, D. B. Newell & B. N. Taylor «The 2018 CODATA Recommended Values of the Fundamental Physical Constants» Committee on Data for Science and Technology (CODATA), 2019 (→ 106).

[123] G. Tommaseo, T. Pfeil, G. Revalde, G. Werth, P. Indelicato & J. P. Desclaux «The g_J-factor in the ground state of Ca^+» in *Eur. Phys. J. D* **25** (2003), 113. DOI: 10.1140/epjd/e2003-00096-6 (→ 106).

[124] T. Udem, J. Reichert, T. W. Hänsch & M. Kourogi «Absolute optical frequency measurement of the cesium D_2 line» in *Phys. Rev. A* **62** (2000), 31801 (→ 20).

[125] S. Umapathy, ed. *J. Raman Spectrosc.* **47**.1 (2016): «Special Issue: International Year of Light 2015». DOI: 10.1002/jrs.4787 (→ 44).

[126] A. Walther, F. Ziesel, T. Ruster, S. T. Dawkins, K. Ott, M. Hettrich, K. Singer, F. Schmidt-Kaler & U. Poschinger «Controlling Fast Transport of Cold Trapped Ions» in *Phys. Rev. Lett.* **109** (2012), 80501. DOI: 10.1103/PhysRevLett.109.080501 (→ 12).

[127] V. Weisskopf & E. Wigner «Berechnung der natürlichen Linienbreite auf Grund der Diracschen Lichttheorie» in *Z. Physik* **63** (1930), 54 ISSN: 0044-3328. DOI: 10.1007/BF01336768 (→ 45).

[128] C. F. von Weizsäcker «Komplementarität und Logik – Niels Bohr zum 70. Geburtstag am 7. 10. 1955 gewidmet.» in *Naturwissenschaften* **42**.19 (1955), 521. DOI: 10.1007/BF00630139 (→ 8).

[129] C. F. von Weizsäcker «Die Quantentheorie der einfachen Alternative – Komplementarität und Logik II» in *Zeitschrift für Naturforschung* **13**.4 (1958), 245. DOI: 10.1515/zna-1958-0401 (→ 8).

[130] C. F. von Weizsäcker «Die Einheit der Natur» Carl Hanser Verlag, 1971 (→ 8).

[131] M. Welling, H. A. Schuessler, R. I. Thompson & H. Walther «Ion/molecule reactions, mass spectrometry and optical spectroscopy in a linear ion trap» in *Int. J. Mass Spectrom.* **172** (1998), 95. DOI: 10.1016/S0168-1176(97)00251-6 (→ 13).

[132] R. F. Werner «Quantum states with Einstein-Podolsky-Rosen correlations admitting a hidden-variable model» in *Phys. Rev. A* **40**.8 (1989), 4277. DOI: 10.1103/PhysRevA.40.4277 (→ 77).

[133] W. K. Wootters & W. H. Zurek «A single quantum cannot be cloned» in *Nature* **299** (1982), 802. DOI: 10.1038/299802a0 (→ 3).

[134] W. K. Wootters «Entanglement of Formation of an Arbitrary State of Two Qubits» in *Phys. Rev. Lett.* **80** (1998), 2245. DOI: 10.1103/PhysRevLett.80.2245 (→ 93).

[135] S-Y. Zhu, L. M. Narducci & M. O. Scully «Quantum-mechanical interference effects in the spontaneous-emission spectrum of a driven atom» in *Phys. Rev. A* **52**.6 (1995), 4791 (→ 44).

[136] S-Y. Zhu & M. O. Scully «Quantum interference effects in the Autler–Townes spontaneous spectrum» in *Phys. Lett. A* **201** (1995), 85 (→ 44).

Index

Page numbers in **bold** indicate the best explanation of the respective lemma or abbreviation that is found in this thesis.